RADIO AND OPTICAL TECHNIQUES FOR LOCATING
EQUATORIAL PLASMA IRREGULARITIES

BY

ETHAN SCHOFIELD MILLER

B.S., Ohio Northern University, 2003
M.S., University of Minnesota, 2005

DISSERTATION

Submitted in partial fulfillment of the requirements
for the degree of Doctor of Philosophy in Electrical and Computer Engineering
in the Graduate College of the
University of Illinois at Urbana-Champaign, 2009

Urbana, Illinois

Doctoral Committee:

Assistant Professor Jonathan J. Makela, Chair
Professor Erhan Kudeki
Professor Steven J. Franke
Professor Andreas C. Cangellaris

ABSTRACT

Plasma density depletions occur in the post-sunset F region ionosphere almost nightly during certain seasons at equatorial latitudes. These depletions contain density irregularities of scales ranging from a few centimeters to thousands of kilometers. Spread-F, the disruption of ionospheric measurements with ionosondes and incoherent scatter radar, and scintillation (fading) of trans-ionospheric radio communication and navigation signals are well-known symptoms of depletions. This dissertation describes new techniques to combine optical and radio ionospheric remote sensing data in common formats to leverage observational strengths and mitigate weaknesses, leading to new or improved physical interpretations. Principally, a technique for locating scintillation-causing irregularities in the Earth's equatorial regions using radio occultation and airglow imaging is presented. A similar technique is employed to study the relationship between Bragg-scale radar backscatter and depletions observed with the airglow imager. A climatology of airglow and radar data from the central Pacific that uncovers regularly occurring post-midnight depletions is also presented. Combined airglow and radar data from these events suggest that polarization electric fields within mesoscale traveling ionospheric disturbances (MSTIDs) seed post-midnight equatorial plasma depletions during geomagnetic quiet periods at solar minimum.

Nos esse quasi nanos, gigantium humeris insidentes, ut possimus plura eis et remotiora videre, non utique proprii visus acumine, aut eminentia corporis, sed quia in altum subvenimur et extollimur magnitudine gigantea.

—Bernard of Chartres

ACKNOWLEDGMENTS

My wife Sarah often remarks that she had no idea what she was getting into when she married a Ph.D. student. Despite that, she has loved, supported, admonished, and encouraged me in ways that no one else can. For that, I am very grateful. My parents Mic and Leah Miller not only instilled in me the curiosity of a scientist and the practicality of a technician, but they have enthusiastically encouraged my education and research.

Jonathan Makela gave me the opportunity to tinker with equipment and ideas, travel widely, and meet interesting people. His support and patience as an advisor have been invaluable. I have enjoyed both classroom and personal interactions with the other members of my committee, Erhan Kudeki, Steve Franke, and Andreas Cangellaris. They have left their mark on me and my work. I am also grateful to Farzad Kamalabadi and Gary Swenson for insightful conversations on remote sensing and engineering education.

The operational linchpin in the Remote Sensing and Space Science group is Paula O'Connor. She navigated the world of university business, international travel, and a rag-tag collection of vendors, keeping us on the move and doing research. Dan Jordan provided logistical support. Scott McDonald and Marc Stevens were invaluable resources in the machine shop and at the Urbana Atmospheric Observatory facility. Mary Schlembach and Bill Mischo kept me stocked with books and journals.

I shared a spacious office with Chad Carlson, Scott Anderson, and Tony Mangognia. We have spent hours talking about remote sensing, education, physics, engineering, and life in general. Marco Milla and Pablo Reyes provided intimate details of the Jicamarca radar. Joe Comberiate, Romina Nikoukar, and Daniel Yao lent their considerable signal processing experience on occasion. I have also enjoyed working closely with Shaun Armstrong, Dwayne Hagerman, Peter Hedlund, Yiyi Huang, Shawn Adderly, Sameeraj Rao, Dan Fisher, and many others as a part of the Airglow and Irregularities group.

The wider CEDAR community has been extraordinarily supportive: Koki Chau (JRO) and Dave Hysell (Cornell) have provided data, insight, and criticism. Mike Kelley (Cornell) sent me to Maui to work on the imagers and GPS receiver. Rebecca Bishop (Aerospace), Roland Tsunoda (SRI), Keith

Groves (AFRL), Sunanda Basu (BC/NRL), and Warner Ecklund (CXI) have provided access to valuable data. Stig Syndergaard (UCAR) got me started doing radio occulation analysis. Countless others have shared valuable feedback to presentations, posters, and papers.

Jake Burger (Boeing/Maui), Gale Brehmer (CTIO/Chile), Jorge Brillones (CTIO/Chile), Ron Mahabir (UWI/Trinidad), and Alan Gross (Bonaire) have been resilient and diligent maintainers of our instrumentation in the field. We would not be able to collect the volume or quality of data without them.

The work presented in this dissertation was supported by a variety of sources, including a start-up grant from the University of Illinois at Urbana-Champaign to Jonathan Makela, National Science Foundation grant ATM-0517641, Naval Research Laboratory contract N00173-05-1-G904, and a National Science Foundation CAREER award.

TABLE OF CONTENTS

LIST OF TABLES

LIST OF FIGURES

LIST OF ABBREVIATIONS

AACGM	Altitude-adjusted, corrected geomagnetic, coordinate system
AFRL	U. S. Air Force Research Laboratory
ALTAIR	ARPA Long-Range Tracking and Instrumentation Radar
BPSK	Binary phase-shift keying
C/A	GPS coarse acquisition code
CASI	Cornell All-Sky Imager (located on Mt. Haleakala in Hawaii)
CEDAR	Coupled Energetics and Dynamics of Atmospheric Regions (NSF research program)
CHAMP	Challenging Microsat Project, carries an occultation receiver
CNFI	Cornell Narrow-Field Imager (located on Mt. Haleakala in Hawaii)
C/NOFS	Communication/Navigation Outage Forecast System
CORISS	C/NOFS Occultation Receiver for Ionospheric Sensing and Specification
COSMIC	Constellation Observing System for Meteorology, Ionosphere, and Climate, occultation experiment
CTIO	Cerro Tololo Inter-American Observatory, La Serena, Chile
CXI	Christmas Island 50-MHz radar
EAR	Equatorial Atmosphere Radar, Kototabang, Indonesia
ECEF	Earth-centered, Earth-fixed, coordinate system
ECI	Earth-centered, inertial, coordinate system
EEJ	Equatorial electrojet
EPB	Equatorial plasma bubble
ESF	Equatorial spread-F
GPS	Global Positioning System
GPS/MET	GPS/Meteorology occultation experiment
GUVI	Global Ultra-Violet Imager (on TIMED satellite)
HWM	Horizontal Wind Model
IGRF	International Geomagnetic Reference Field model
IOX	Ionospheric Occultation Experiment, occultation experiment

IRI	International Reference Ionosphere model
JHU/APL	Johns Hopkins University Applied Physics Laboratory
JRO	Jicamarca Radio Observatory, Jicamarca, Perú
L_1	Primary GPS L-band frequency (1.57542 GHz)
L_2	Secondary GPS L-band frequency (1.22670 GHz)
MSTID	Medium-scale traveling ionospheric disturbance
NASA	U. S. National Aeronautics and Space Administration
NRL	U. S. Naval Research Laboratory
NRLMSIS	NRL Mass-Spectrometer Incoherent Scatter atmosphere model
NSF	National Science Foundation
PICASSO	Portable Ionospheric Camera and Small-Scale Observatory
RTI	Range-time-intensity (alt. Rayleigh-Taylor instability)
RTV	Range-time-velocity
SBAS	Satellite-Based Augmentation System
SCINDA	AFRL Scintillation Network Decision Aid, network of scintillation receivers
SCINTMON	Cornell University GPS Scintillation Monitor
SNR	Signal-to-noise ratio
SRI	Formerly Stanford Research Institute, now SRI International
TEC	Total electron content
TECU	TEC unit, 10^{16} e^-/m^2
TIMED	Thermosphere Ionosphere Mesosphere Energetics and Dynamics satellite mission
TOA	Time-of-arrival
UCAR	University Corporation for Atmospheric Research
WAAS	Wide-Area Augmentation System

LIST OF SYMBOLS

A	Azimuth, Einstein efficiency
$\mathbf{B}$	Magnetic field vector
c_0	Speed of light in a vacuum
c	Wave speed
E	Electric field scalar
$\mathbf{E}$	Electric field vector
$\mathbf{F}$	Force vector
f	Radio frequency (angular units)
f_p	Plasma frequency (angular units)
h	Altitude
$h_{m\mathrm{F}2}$	Height of the peak electron density in the F_2 layer
I	Received SNR
$\mathbf{J}$	Current (density) vector
k	Wavenumber, reaction rate coefficient
$\mathbf{k}$	Wavevector
K_p	Planetary K index, a measure of geomagnetic activity
m_e	Electron mass
m_i	Ion mass
n_e	Electron density
n_i	Ion density
$n_{m\mathrm{F}2}$	Peak electron density in the F_2 layer
n_n	Neutral density
q_e	Fundamental electronic charge
r_e	Classical electron radius
R_e	Earth radius
S_4	Short-time normalized variance of received SNR

T	Neutral temperature
T_n	Neutral temperature
T_e	Electron temperature
T_i	Ion temperature
u	Scalar electric field, also zonal neutral wind
$\mathbf{U}$	Neutral wind vector
v	Zonal neutral wind
$\mathbf{V}$	Plasma drift
z	Coordinate axis in the direction of wave propagation, altitude
α	Right ascension
β	Wavenumber, Einstein efficiency
δ	Latitude
ϵ	Horizon elevation
ϵ_0	Permittivity of free space
η	Photochemical volume emission rate
λ	Longitude, radio wavelength, Debye length
ν_{ei}	Electron-ion collision frequency
ν_{en}	Electron-neutral collision frequency
ν_{in}	Ion-neutral collision frequency
ξ	Azimuth
$\bar{\bar{\sigma}}$	Conductivity tensor
σ	Conductivity, also a generalized representation of S_4 that does not imply 50-Hz sample rate
σ_0	Specific conductivity
σ_H	Hall conductivity
σ_P	Pedersen conductivity
τ	Group delay
Υ_{FF}	Flat-field matrix
ϕ	Electric potential
ω	Radio frequency (angular units)
ω_p	Plasma frequency (angular units)
Ω_i	Ion gyrofrequencies
Ω_e	Electron gyrofrequencies

CHAPTER 1

THE EQUATORIAL IONOSPHERE

1.1 Introduction

The ionosphere and thermosphere envelop Earth in the altitude range of approximately 70–1000 km. The defining characteristic of the ionosphere is its composition of partially ionized gas plasma. Because both neutral (thermosphere) and ionized (ionosphere) species are present at these heights and they exist in the presence of Earth's geomagnetic field, the ionosphere is host to a number of interesting phenomena such as spectacular auroral displays and otherwise "invisible" waves and turbulence that affect radio waves passing through the region. Figure 1.1 shows empirical models of the ionospheric electron and thermospheric neutral densities at a typical low-latitude site near Hawaii. The neutrals dominate density until well above the ionosphere. Molecular oxygen and nitrogen are dominant in the lower atmosphere, but lighter species such as atomic helium and hydrogen dominate at high altitudes.

The day-to-day behavior of the ionosphere/thermosphere system is driven by the sun. The ionosphere forms as neutral species in the thermosphere absorb EUV and X-ray radiation from the sun. Ions and electrons produced at lower altitudes drift upward due to diffusion and the effects of the geomagnetic field. Thermospheric winds arising from solar convection drive dynamo currents in the presence of the geomagnetic field. These three effects—production (and loss), particle drift, and dynamos—will guide most of our discussions about the ionosphere.

The ionosphere is divided into three regions labeled D, E, and F. The regions are differentiated mostly through their compositions, which in turn affect collision rates between species, which in turn affects the plasma conductivity, which is anisotropic due to the geomagnetic field. The D region occupies the lower portion of the ionosphere, at an altitude of about 70–90 km. It is characterized by high neutral density, and therefore, a high frequency of both electron-neutral and ion-neutral collisions. Although the D region is not of particular interest to this work, the high collision frequencies make it the major contributor to daytime ionospheric absorption of low-frequency (< 30 MHz) radio waves. In the E region, 90–120 km, ion-neutral collisions remain important; however,

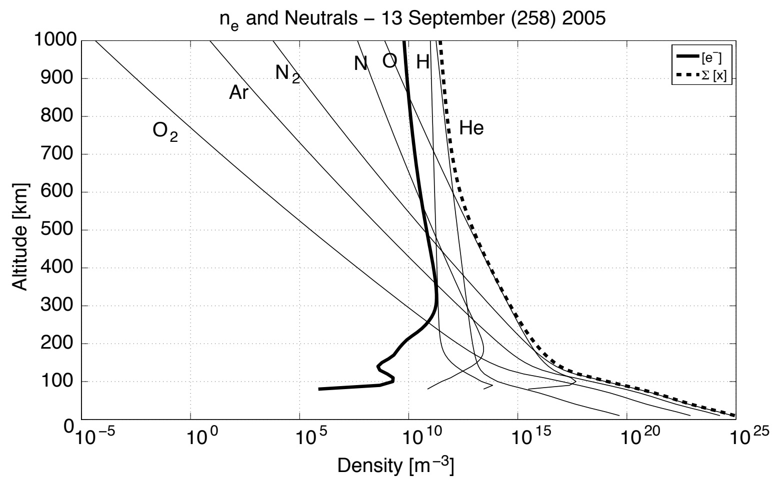

Figure 1.1: Empirical models of the electron and neutral density profiles in the ionosphere-thermosphere system. The electron density is from the International Reference Ionosphere, IRI 2007 [*Bilitza and Reinisch*, 2008], and the neutral densities come from NRLMSISE-00 [*Picone et al.*, 2002].

electron-neutral collisions are less important. The E region contains many ions, both from solar production and metallic ions from meteor ablation. In the low-latitude ionosphere, as discussed in the next section, the E region hosts the equatorial electrojet (EEJ) and the E-region dynamo, which are dominant features of that region. The F region, loosely the remaining ionosphere from 120 to 1000 km, is predominately electrons and light ions. As a consequence of this, collisions are not dominant. The size of the F region and its constituency of mobile electrons make it very important in the propagation of radio waves. A defining metric of the plasma density is the plasma frequency, which is the resonant frequency of a parcel of plasma. As such, it varies with time and position. Below the plasma frequency, radio waves are reflected by the plasma. Above the plasma frequency, increasing electron density corresponds to decreased refractive index at a given radio frequency.

Irregularities in the plasma density, especially dynamic, turbulent irregularities, may have profound effects on radio waves passing through the ionosphere. A class of these equatorial F-region irregularities is the subject of this dissertation. This dissertation is primarily concerned with the behavior of the equatorial ionosphere and irregularities therein that degrade satellite radio communication and navigation systems. The remainder of this chapter is devoted to the equatorial ionosphere, its day-to-day behavior, and the irregularities that are produced there. Some of the outstanding problems will be identified, especially those addressed in this dissertation. An outline of the dissertation concludes the chapter.

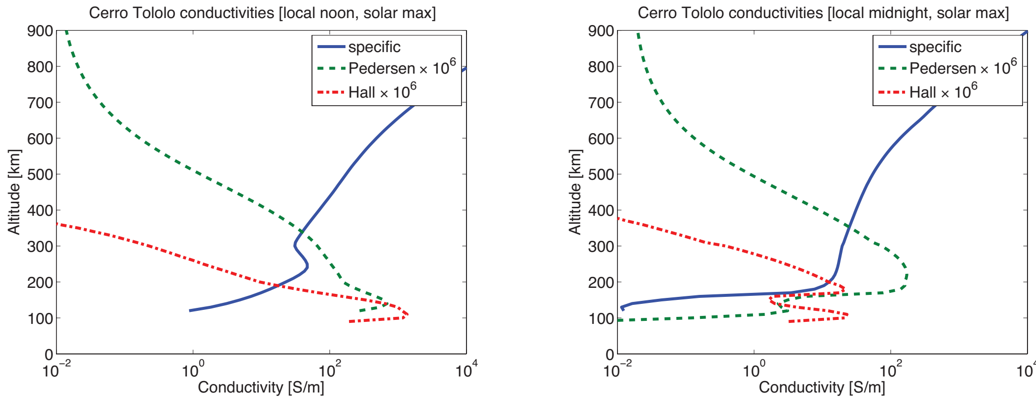

(a) (b)

Figure 1.2: Typical low-latitude conductivity profiles for solar maximum conditions up to 900 km at local (a) noon and (b) midnight. Note that the Pedersen and Hall conductivities are scaled by 10^6.

1.2 Conductivity

In a collisionless plasma, charged particles in the presence of the geomagnetic field gyrate in the plane perpendicular to the magnetic field. Although the particles are free to move parallel to the magnetic field, they do not readily move in the perpendicular direction. Ions and electrons may move perpendicular to the magnetic field under electrodynamic influences, such as the $\mathbf{E} \times \mathbf{B}$ drift, or interactions (collisions) with other particles. This situation yields anisotropic conductivity. In a coordinate system $(\hat{\mathbf{a}}_x,\hat{\mathbf{a}}_y,\hat{\mathbf{a}}_z)$[1] with $\hat{\mathbf{a}}_x$ perpendicular to the geomagnetic field in the (magnetic meridional) plane swept out by the geomagnetic field and $\hat{\mathbf{a}}_z$ parallel to the geomagnetic field, $\hat{\mathbf{a}}_y$ is the remaining Cartesian coordinate perpendicular to both $\hat{\mathbf{a}}_x$ and $\hat{\mathbf{a}}_z$. The conductivity tensor for this geometry is written

$$\bar{\bar{\sigma}} = \begin{pmatrix} \sigma_P & -\sigma_H & 0 \\ \sigma_H & \sigma_P & 0 \\ 0 & 0 & \sigma_0 \end{pmatrix}, \tag{1.1}$$

where σ_P, σ_H, and σ_0, are the *Pedersen*, *Hall*, and *specific* conductivities, respectively. The Pedersen conductivity is in the direction perpendicular to $\mathbf{B}$ and parallel to the $\mathbf{E}$ field; that is, it is due to currents driven by $\mathbf{F} = q_e\mathbf{E}$. The Hall conductivity is in the direction of the $\mathbf{E} \times \mathbf{B}$ drift. The conductivities are finite due to collisions between species. The specific conductivity is about 10^5 larger than either the Pedersen or Hall conductivities. Figure 1.2 shows a typical set of conductivity profiles for an equatorial location up to 900 km.

[1]This is sometimes written $(\hat{\mathbf{a}}_\phi,\hat{\mathbf{a}}_\theta,\hat{\mathbf{a}}_p)$.

1.3 Quiescent Behavior

Principal among the large-scale quiescent processes of the equatorial ionosphere are the E- and F-region dynamos. Fundamentally, the dynamos operate due to the wind-driven currents and the conservation expression requiring *divergence-free* current (Kirchhoff's current law), which can be expressed in the steady state as

$$\nabla \cdot \mathbf{J} = 0. \tag{1.2}$$

Due to the relatively high density of neutrals in the E region, the ion-neutral collision frequency is high there. This facilitates the E-region dynamo as thermospheric neutral winds drag ions across field lines in the part of the E region where σ_H is the dominant conductivity [e.g., *Heelis*, 2004]. Since the net flow of charge constitutes a current, Equation (1.2) must be satisfied by drawing current into the circuit along the geomagnetic field lines. At night, the E (and D) region(s) recombine quickly, reducing the Hall and Pedersen conductivities there. The F-region dynamo, which is dominated by the effects of the Pedersen conductivity, then takes over [*Heelis*, 2004; *Rishbeth*, 1997]. The thermospheric zonal wind drives a current that is predominantly in the magnetic meridional direction, that is, a Pedersen current:

$$\mathbf{J} = \bar{\bar{\sigma}} \cdot (\mathbf{U} \times \mathbf{B}) \, . \tag{1.3}$$

Because the conductivity of the ionosphere is inhomogeneous, polarization electric fields form as charges build up at the terminator separating the day and night sides of the Earth. In order to satisfy the electromagnetic form of Kirchhoff's voltage law,

$$\oint \mathbf{E} \cdot d\ell \approx 0, \tag{1.4}$$

this charge separation creates an eastward electric field on the day side of the Earth and a westward electric field on the night side. This zonal electric field is designated E_ϕ in Figure 1.3, which illustrates the sunset terminator and some associated electrodynamic and neutral properties. The plasma densities and neutral winds shown in Figure 1.3 are from IRI2007 and HWM07, respectively [*Bilitza and Reinisch*, 2008; *Drob et al.*, 2008], for a representative day, 22 August 2005, at a point (geographic 2° N, 203.5° E) in the central Pacific. At the geomagnetic equator where the $\mathbf{B}$ is northward and approximately parallel to Earth's surface, the plasma drifts upward during the

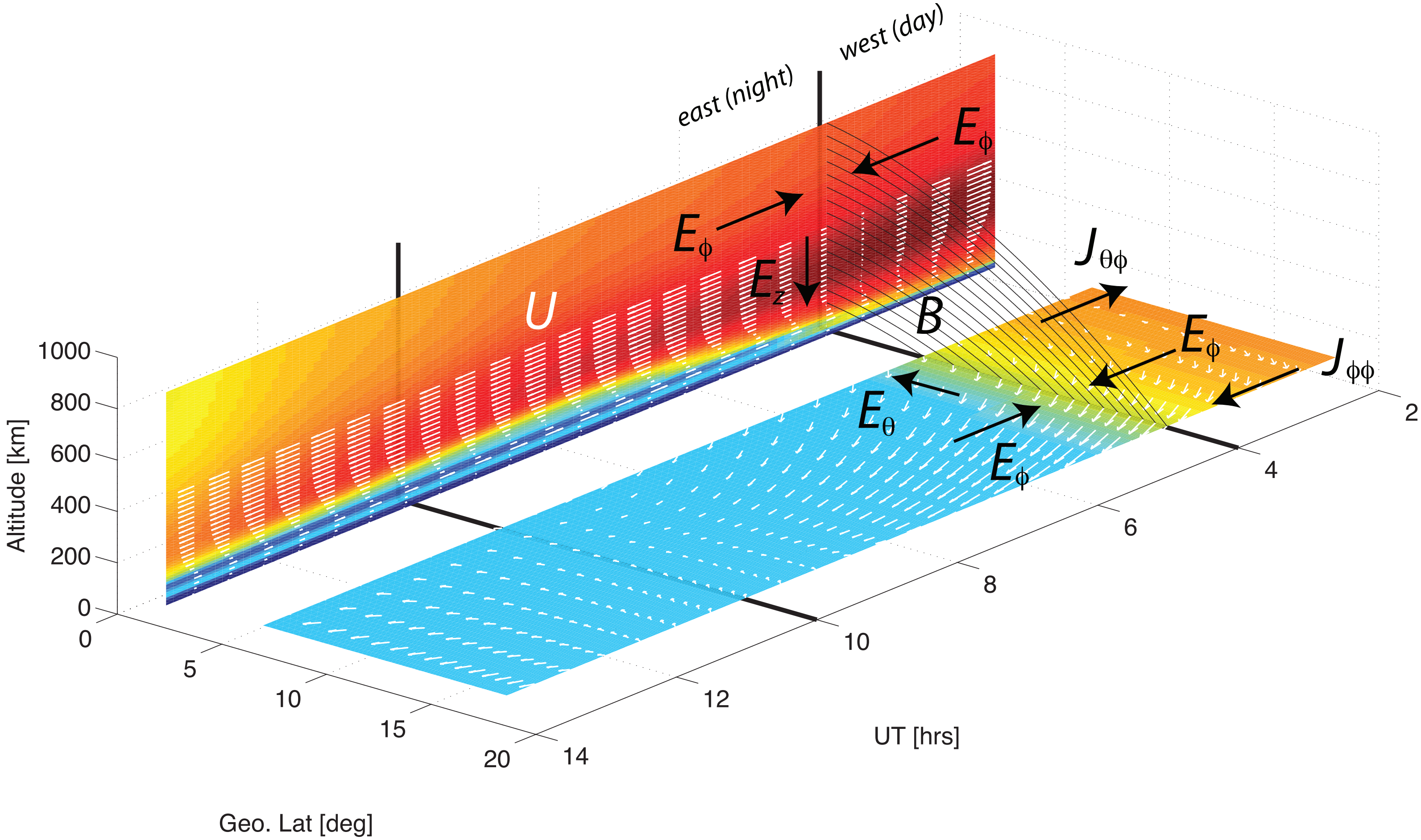

Figure 1.3: Illustration of the equatorial ionosphere at the sunset terminator. This example is taken from the central Pacific region (geo: 2° N, 203.5° E) in late August 2005. The equatorial F-region density plotted in the vertical (time-altitude) plane and the off-equator E region density plotted in the horizontal (time-latitude) plane were modeled using the International Reference Ionosphere (IRI) 2007. The thermospheric neutral wind vectors are from the Horizontal Wind Model (HWM07). The electrodynamic quantities are labeled according to *Farley et al.* [1986]

day and downward at night under the influence of the zonal electric field E_ϕ at a velocity

$$\mathbf{V}_{\mathrm{drift}} = \frac{\mathbf{E} \times \mathbf{B}}{|\mathbf{B}|^2}. \tag{1.5}$$

As the plasma drifts upward into lower density regions, partial pressure gradient forces and gravity push the plasma back down the highly conductive field lines. This plasma forms two crests of increased density, one on either side of the geomagnetic equator. The regions of increased ionization are known by various names; however, for the purpose of this work we refer to them as the *equatorial anomaly crests*.[2] The equatorial anomaly crests are a prominent feature that is observable from the ground and space using optical airglow emissions, as well as electron density measurements. Figure 1.4 illustrates the crests of the equatorial anomaly as observed optically at 135.6 nm by the Global Ultraviolet Imager (GUVI) instrument on the Thermosphere, Ionosphere, Mesosphere, Energetics and Dynamics (TIMED) spacecraft [*Christensen et al.*, 2003].

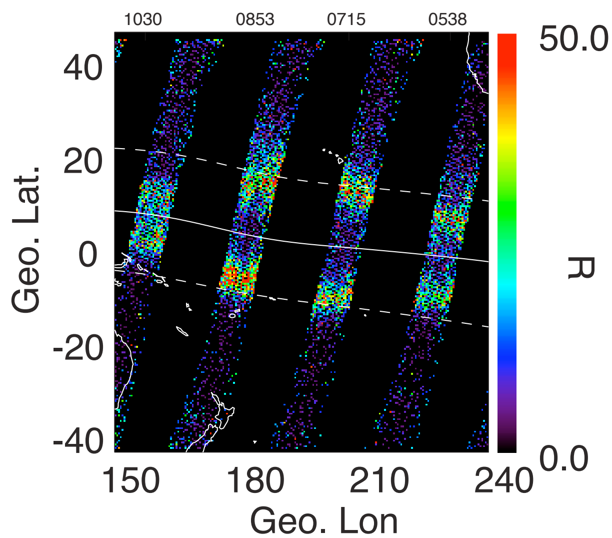

Figure 1.4: Equatorial anomaly crests over the central Pacific observed through the 135.6-nm nightglow emission by the GUVI instrument. Each strip of airglow image represents one orbit of the TIMED spacecraft. The time of the geomagnetic equator crossing is given in UT at the top. Data courtesy of JHU/APL.

Following sunset, the zonal electric field reverses (to the West) in order to satisfy the KVL relationship above. The description given here follows *Farley et al.* [1986], but there are several competing theories [e.g., *Rishbeth*, 1971; *Haerendel and Eccles*, 1992; *Eccles*, 1998]. Before the field reverses, it frequently increases rapidly, increasing the $\mathbf{E} \times \mathbf{B}$ drift and raising the ionosphere [*Wood-*

[2]It has been reasoned that they are no longer anomalous since the theory of their formation is well established, but the name remained.

man, 1970; *Fejer et al.*, 1979; *Farley et al.*, 1986]. This effect is known as the prereversal enhancement (PRE) or post-sunset rise (PSSR). The prereversal enhancement is an important feature of the equatorial ionosphere. Vertical drift velocities are on the order of 40 m/s. The PRE is a seasonal feature, although it also appears to be strongly affected by the solar cycle [*Fejer et al.*, 1979; *Kelley*, 1989]. At Jicamarca, the largest PREs are observed at solar maximum during the equinoxes and summer. One of the most important features of the PRE is its association with the growth of equatorial plasma irregularities.

1.4 Irregularities

A number of ionospheric irregularity types occur at equatorial and low latitudes. For instance, the electrojet is subject to turbulence and irregularities that disrupt radar measurements of ionospheric profiles [e.g., *Berkner and Wells*, 1937; *Bowles et al.*, 1960]. Otherwise, for practical purposes, these irregularities are apparently benign. However, in the F region, large plumes of irregularities grow after sunset on a nearly daily basis in some geographic areas and seasons. These irregularities have a profound effect on trans-ionspheric radio communication and navigation signals, causing everything from minor fading to complete loss of signal lock. Since their initial discovery in the 1930s, post-sunset equatorial irregularities have been a subject of intense scientific and practical interest [*Booker and Wells*, 1938].

Booker and Wells discovered irregularities using an ionosonde. Ionosondes were the earliest ionospheric radio remote sensing instruments [*Breit and Tuve*, 1925]. They are small, swept-frequency (1–20 MHz or so) radars with vertical beams that are used to measure the altitudes of scattering layers. Under normal circumstances, the upward-traveling wave continues until it reaches the altitude where the plasma frequency equals the radio frequency and the wave is reflected. The group delay of reflected pulses is measured to determine the virtual height of reflection, which can be used to determine the altitude of the peak plasma density. A normal ionogram showing a relatively smooth, thin curve for virtual height is shown in Fig. 1.5a. Multiple traces indicate that the pulse has been reflected one or more times by the ground and again off the ionosphere. When the ionosphere is no longer smooth, scattering occurs at many altitudes, spreading the virtual height curve, as shown in Fig. 1.5b. This is the phenomenon known as equatorial spread-F. Study of 50-MHz coherent backscatter from irregularities associated with spread-F began in the 1960s and 1970s at Jicamarca, Perú [*Farley et al.*, 1970; *Woodman and Hoz*, 1976]. Figure 1.5c shows the 50-MHz backscatter SNR

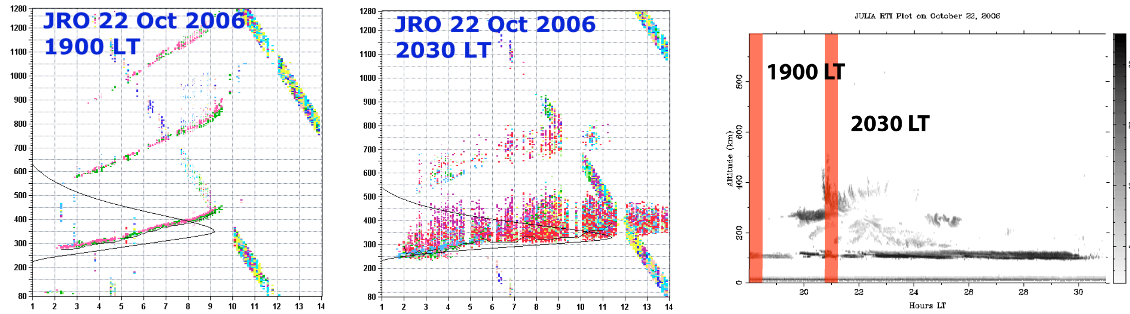

(a) (b) (c)

Figure 1.5: Ionograms from Jicamarca, Perú, on the night of 22 October 2006 under (a) normal (at about 1930 LT) and (b) spread (2030 LT) conditions. Frame (c) is the coherent backscatter map from the Jicamarca radar for the same time period. The highlighted vertical lines refer to the times of the ionograms in subfigures (a) and (b). Data courtesy of Jicamarca Radio Observatory.

observed as the irregularities drifted across the Jicamarca radar beam. Notice the correspondence between spread-F on the ionogram in Figure 1.5b and strong F-region backscatter observed by the radar in Figure 1.5c at the same (2030 LT) time. Earlier at 1900 LT, no spreading was observed in the ionogram (Figure 1.5a) and no F-region backscatter was observed by the radar. The heavy layer of echoes in the 100–120 km altitude range is due to electrojet instabilities mentioned briefly at the beginning of this section.

The coherent echoes observed by the 50-MHz radar correspond to irregularities in plasma density at the 3-meter scale. The same mechanism is responsible for the spreading of the virtual height curve on the ionograms, except that the frequencies involved are much lower and the irregularity scales correspondingly larger. Coherent backscatter occurs at the *Bragg* wavelength, which is one half the radio wavelength.

The term "spread-F" commonly refers to an entire linked set of irregularities spanning scales from centimeters to megameters, although the term itself stems from the specular echoes described above. There are three spread-F irregularity scales that are easily observed from the ground. Structures larger than about 10 km up to a 1000 km or more are observable with airglow imagers. The 100–1000 m range irregularities are observed through forward-scatter radio scintillation measurements. Finally, the smallest irregularities on the order of meters are observed via coherent radar backscatter. In situ rocket density spectra and forward scatter radio observations suggest that it is probable that at least two classes of irregularities exist when fully developed, one at large ($\gtrsim 100$ m) and the other at small scales [e.g., *Kelley et al.*, 1982; *Yeh and Liu*, 1982]. As early as 1956, it was theorized that a collisional interchange instability, specifically the gravitational Rayleigh-Taylor instability, might be responsible for the growth of large-scale plasma irregularities associated with equatorial spread-

F [*Dungey*, 1956]. The small-scale irregularity mechanism remains the subject of some debate and will be addressed in Chapter 5.

The Rayleigh-Taylor instability can occur when a dense fluid is supported above a less-dense fluid, as depicted in Figure 1.6. In the case of the equatorial ionosphere, a steep plasma density gradient forms on the bottom side of the F region when the ion-rich E region recombines after sunset. Since the geomagnetic field, $\mathbf{B}$, is nearly horizontal at the equator, the gravitational effect on electrons and ions drives a current in the zonal direction,

$$\mathbf{J} = \frac{n_i m_i \mathbf{g} \times \mathbf{B}}{|\mathbf{B}|^2}. \tag{1.6}$$

Above the gradient, there is plenty of plasma density and the gravity-driven current ($\mathbf{J}$) is large. Below the gradient, the density (and hence, the current) is low. A small perturbation in the gradient causes polarization charges to build up, keeping the current divergence-free. These polarization charges force a polarization electric field ($\delta\mathbf{E}$) to form within the perturbation, driving the perturbation even larger by the $\delta\mathbf{E} \times \mathbf{B}$ drift. Once this process begins, it evolves rapidly.

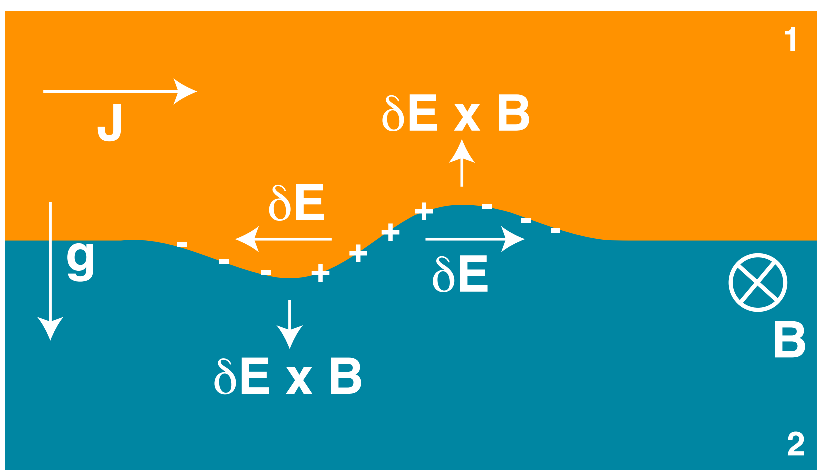

Figure 1.6: Cartoon of the gravitational Rayleigh-Taylor instability operating in the equatorial ionosphere. The geomagnetic field, $\mathbf{B}$, is directed into the page. Region 1 has much higher plasma density than Region 2.

Figure 1.7 illustrates a cartoon of irregularity formation and growth. A seed instability (the result of a transient or another phenomenon) forces the gradient in the bottom side of the F region into a rapidly evolving non-linear Rayleigh-Taylor instability. As the depleted regions grow in altitude, the

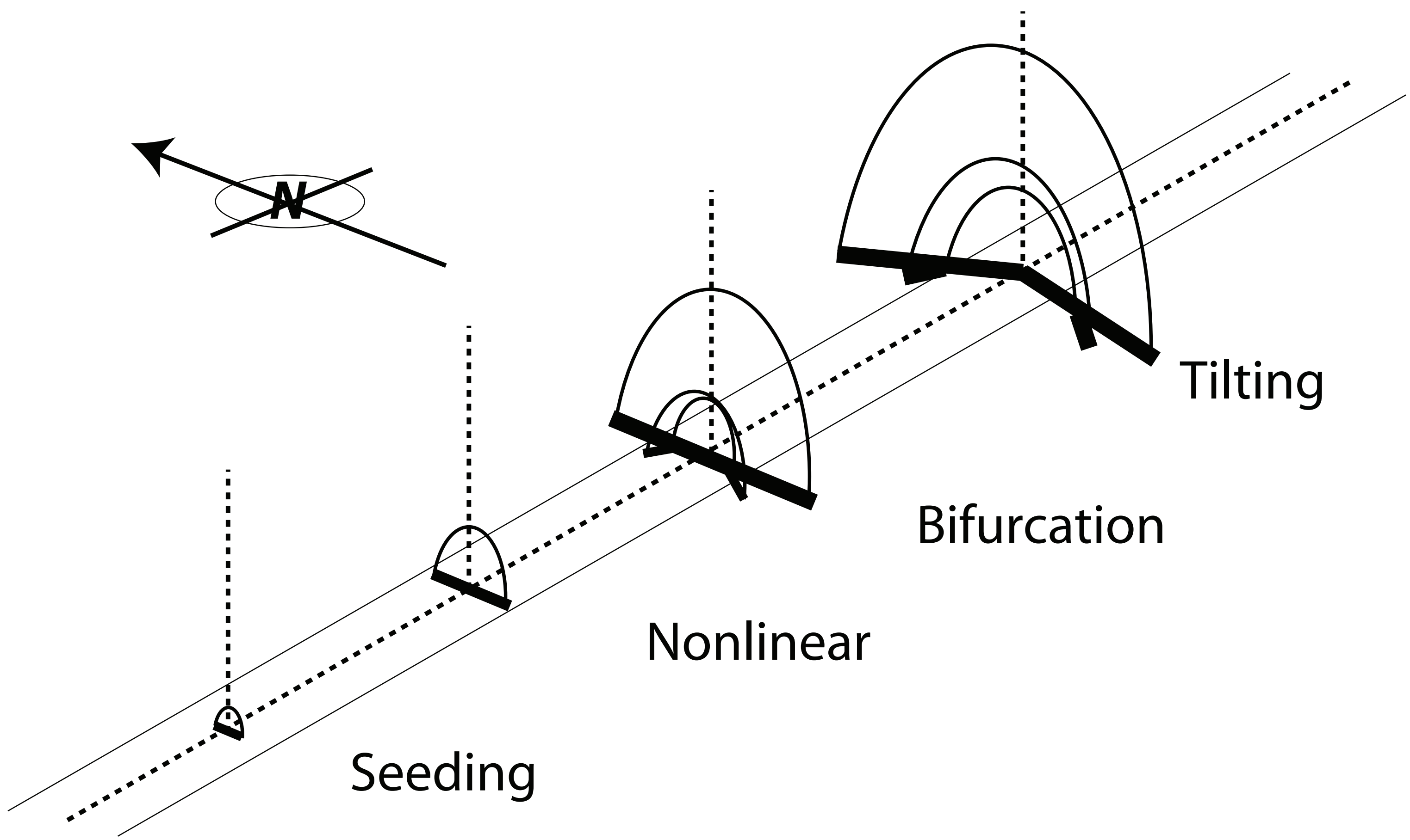

Figure 1.7: Evolution of equatorial plasma depletion during growth. Lines of magnetic latitude extend from lower left to upper right. The center (dotted) line is the geomagnetic equator.

large-scale polarization electric fields associated with them are mapped along the geomagnetic field, displacing the plasma in a wedge-shaped region [e.g., *Farley*, 1960; *Aarons et al.*, 1980; *Tsunoda et al.*, 1982; *Mendillo and Tyler*, 1983]. A differential in the eastward neutral wind and the plasma drift velocity causes gradient-drift instabilities to form on the western walls of the depletions, some of which erupt into bifurcations. This theory is widely accepted and supported by models [*Ossakow*, 1981; *Hysell*, 2000]; however, the lack of a suitable explanation for the seeding of equatorial spread-F has left scholarly debate open on the issue.

Gravity waves propagating up from below the ionosphere/thermosphere have long been suggested as one possible seed [e.g., *Kelley et al.*, 1981]. One difficulty with the gravity wave theory lies in the ability to observe them at thermospheric altitudes. In order to conserve momentum as the atmospheric background density decreases, gravity wave amplitudes grow as the wave propagates upward. This means that waves that are large in the thermosphere are frequently vanishingly small at lower altitudes, making them difficult to observe near their origin. Furthermore, winds in a gravity wave are parallel to the isodensity phase fronts. In order to perturb the plasma in the F region, where the Hall and Pedersen conductivities are very low, the wind must have a significant component parallel to the geomagnetic field. This suggests that gravity waves may not directly impact the motion of the plasma. However, neutral wind field perturbation may affect the growth rate of irregularities through the theories expressed in the next paragraphs.

Another interesting possibility is that the Rayleigh-Taylor instability could be initiated by polarization electric fields generated in the E region north or south of the geomagnetic equator that map along the geomagnetic field to the bottom side F region at the equator [*Tsunoda*, 2006, 2007]. This process is probably responsible for at least a fraction of depletions observed forming more than 2–3 hours after sunset or during seasons in which depletion formation is unlikely. Evidence supporting this theory is presented in Chapter 6.

Recent work based on data from the Jicamarca radar in Perú has shown that electrodynamics of the evening ionosphere can produce seed instabilities capable of triggering the Rayleigh-Taylor instability under favorable conditions ([*Kudeki and Bhattacharyya*, 1999; *Hysell et al.*, 2004; *Kudeki et al.*, 2007]). These irregularities, termed *bottom-type layers* in [*Woodman and Hoz*, 1976; *Hysell and Burcham*, 1998], grow with wavelengths on the scale of 20–30 km. The structure of bottom-type layers was revealed using radar imaging techniques [*Hysell*, 1996; *Woodman*, 1997]. Although bottom-type layers appear to be a necessary precursor to larger post-sunset irregularities, their presence is not alone sufficient to seed depletion formation.

The E region recombines rapidly after sunset as ion production ceases, reducing conductivity there. Lacking the E region as a load, the F-region dynamo currents seek closure in order to remain divergence-free. That is, the F-region dynamo behaves like an energized relay coil in steady state [*Rishbeth*, 1997]. In this analogy, abruptly breaking the circuit (without proper mitigation circuitry) causes the relay to chatter before settling again to steady state. Likewise, the ionosphere responds to this transient through several phenomena, including the pre-reversal enhancement of the zonal electric field and irregularities on the bottom side of the F region [*Kudeki et al.*, 2007].

Perhaps one of the more compelling studies in understanding the initiation of equatorial spread-F is that of conditions which are necessary but perhaps insufficient. The seasonality [*Gentile et al.*, 2006] of equatorial spread-F is thought to be modulated in large part by the alignment between the solar terminator and the geomagnetic meridian [*Tsunoda*, 1985]. According to this theory, when the terminator is aligned with the geomagnetic field, the northern and southern E regions will recombine at approximately the same time (neglecting plasma transport and density asymmetry), producing the sharpest transient. Both models [e.g., *Sultan*, 1996]) and observations [e.g., *Basu et al.*, 1996] suggest that strong $\mathbf{E} \times \mathbf{B}$ drifts are required for irregularity development. The spacing between the crests of the equatorial anomaly can serve as a proxy for the $\mathbf{E} \times \mathbf{B}$ drift. *Basu et al.* [2009] have presented observational and modeled examples of "collapsed" equatorial anomaly crests which appear to inhibit the formation of F-region irregularities. In the SAMI3 [*Huba et al.*, 2005] model, collapses are generated in conjunction with local reversal of the equatorial electrojet from east to west in the afternoon. This suggests that these counter-electrojet events can be inhibitors of spread-F.

Figure 1.8 is an oft-shown illustration of a *wave-4* structure in the equatorial arcs as observed from the IMAGE instrument [*Immel et al.*, 2006]. The locations of wider arc spacings are coincident with tropical convection centers. *England et al.* [2006] explain this through the daytime modulation of the equatorial plasma fountain through the E-region neutral wind. This is indeed interesting because a study of AE-1 satellite data suggests that there is some correlation between tropical convection and irregularity development [*McClure et al.*, 1998]. This suggests an alternative, although as of yet unverified, link between convection and irregularity development which may or may not depend on gravity waves.

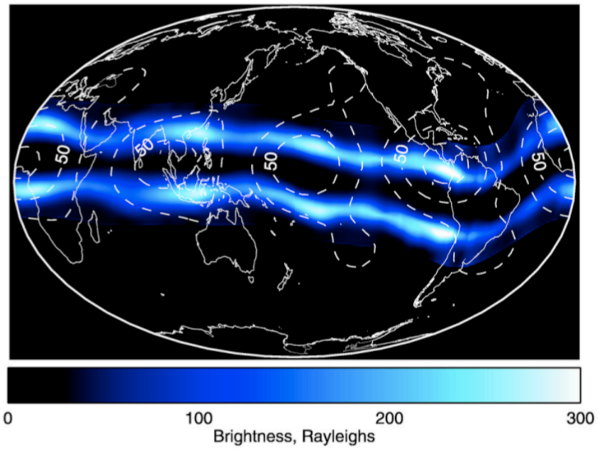

Figure 1.8: Modulation of density and location of the northern equatorial arc observed from space by the IMAGE spacecraft. The southern arc was reflected across the geomagnetic equator. After [*Immel et al.*, 2006]. (Reproduced with permission of the American Geophysical Union.)

1.5 Irregularity Effects

The primary known impact of ionospheric irregularities is scintillation. Scintillation is an optical diffraction effect that causes rapid fluctuations in the amplitude or phase of the received signal when a radio wave propagates through a turbulent medium [e.g., *Yeh and Liu*, 1982]. Figure 1.9 illustrates the geometry of the space-to-ground radio wave scintillation problem. A slab of irregularities with thickness L exists at a distance z from the receiver. A transmitter illuminates the slab of irregularities from $-\infty$.

Irregularities have both a scale and a perturbation "depth" which affect the observed scintillation on the ground. Commonly, amplitude fading occurs while the phase remains relatively constant. This is the situation of "weak" scintillation. "Strong" scintillation entails phase scintillation in addition to amplitude scintillation. Strong scintillation of this type is most common on VHF and UHF trans-ionospheric radio links during solar maximum. Scintillation events are often classified by their S_4 index, which is a short-time normalized variance of the signal-to-noise ratio (SNR) of the received signal,

$$S_4^2 = \frac{\langle I^2 \rangle - \langle I \rangle^2}{\langle I \rangle^2}, \tag{1.7}$$

where I is the SNR and $\langle \cdot \rangle$ represents the short-time average over a number of samples. The S_4 index indicates the depth of the fade with respect to signal strength. That is, $S_4 = 1$ indicates that the fade is as large as the signal strength itself.

Irregularities that cause amplitude scintillation observed at a receiver are of the order of the

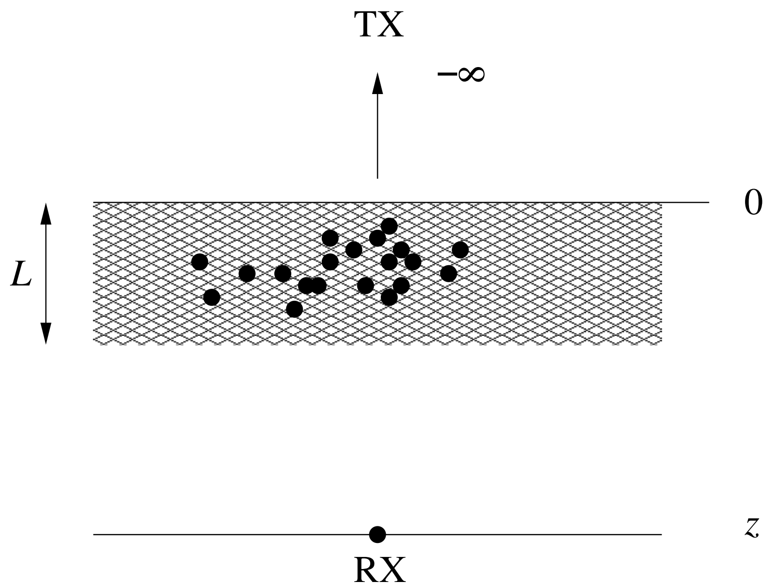

Figure 1.9: Geometry of the space-to-ground radio wave scintillation problem. A slab of irregularities with thickness L exists at a distance z from the receiver. The transmitter is much farther from the irregularities than the receiver (Fresnel approximation).

Fresnel scale, yielding a diffraction pattern that moves with respect to the receiver due to the motion of the signal source, irregularities, and the receiver (in the case of the non-stationary receiver). An estimate of the Fresnel scale based on the first Fresnel zone for a slab of random density is given by

$$d_F = \sqrt{\lambda(z - L/2)}, \tag{1.8}$$

where z is the range to the far (with respect to the receiver) side of the slab and L is the slab thickness [*Yeh and Liu*, 1982]. First-order estimates of the Fresnel scale for the irregularities associated with equatorial spread-F can be obtained by assuming that the slab is located at the F peak. Scattering regions have been reported at altitudes higher than the F peak [*Sokolovskiy et al.*, 2002; *Cerruti et al.*, 2006], although there is very little data on scattering altitude with which to corroborate these results. Furthermore, the altitude of the F peak varies, yielding errors in the Fresnel scale estimate without some independent measurement of this parameter [*Batista and Abdu*, 2004]. Estimation of the altitude distribution of scintillation-causing irregularities is the subject of Chapter 4.

Irregularities can have a profound effect on satellite-based radio communication and navigation systems. For navigation systems which rely on the propagation delay of signals from satellite-based transmitters, depletions and gradients in electron density distort the accuracy of navigation solu-

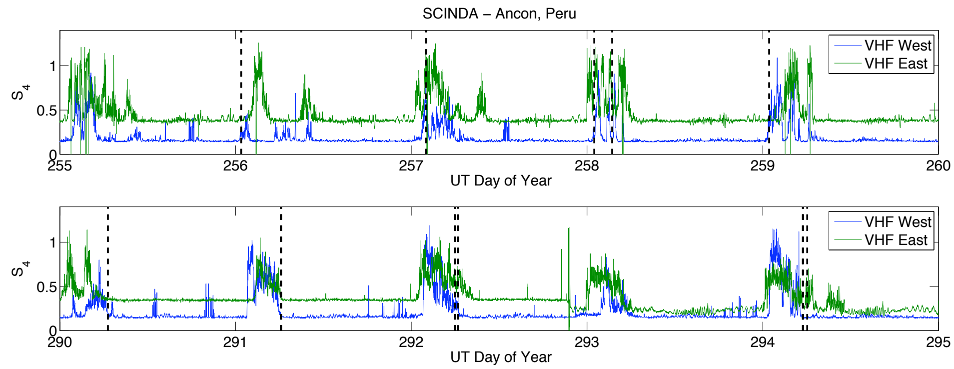

Figure 1.10: SCINDA S_4 plots from Ancón, Perú, in September and October 2006. Notice that scintillation occurs almost on a nightly basis. After [*Miller and Makela*, 2008]. (Reproduced with permission of the American Geophysical Union.)

tions. If scintillation associated with these irregularities causes severe amplitude or phase fading, the receivers may lose lock on the signal, rendering communication or navigation impossible for periods of a few minutes or hours. Therefore, users of these systems are keenly interested in scintillation detection, prediction, and mitigation systems. The U. S. Air Force operates a worldwide system of VHF and L-band (1.6 GHz) receivers known as the Scintillation Network Decision Aid (SCINDA) [*Groves et al.*, 1997]. These receivers calculate 87-second S_4 continuously as well as drift velocities when irregularities are present to perform a cross-correlation. Figure 1.10 shows VHF (240 MHz) SCINDA S_4 data from Ancón, Perú, in September and October 2006. At this location, scintillation is observed on a nearly nightly basis during these time periods.

The spectrum of irregularities observed by a scintillation receiver can be obtained through the Fourier transform of the received signal. This technique has been utilized to study the scale distribution of irregularities [e.g., *Yeh and Liu*, 1982]. More recently, it has also been employed to determine the altitude of irregularities [*Bhattacharyya et al.*, 2001].

1.6 Questions and Contribution

1.6.1 Four problems

Generally speaking, there are four outstanding areas of research for equatorial F region irregularities:

Seeding of Equatorial Depletions / Spread-F

The first question pertains to the seeding and suppression of equatorial plasma depletions. Although much work has been performed in this area, the complexity of proposed drivers and the variability of the ionosphere-thermosphere system make it a challenging problem. Compelling evidence has been provided to justify the claim that the initiation is a cascade or sequence of plasma instabilities. It is theorized that the zonal [*Kudeki et al.*, 2007] and meridional [*Mendillo et al.*, 1992] neutral winds play an important role in the initiation of irregularities. Therefore, it is conceivable that gravity waves, which are a neutral perturbation phenomenon, may modify the background wind in a manner conducive to irregularity development. *Tsunoda* [2007] has also shown that electric fields associated with off-equator irregularities in the E or lower F region may be responsible for seeding of certain kinds of irregularities.

Conjugacy of Depletions

The second outstanding area is in the conjugacy of depletion growth. Models and initial observations suggest that below a certain scale, probably on the order of 10s of km, irregularities observed in the northern geomagnetic hemisphere may not be well-correlated with those observed in the southern geomagnetic hemisphere. Only a handful of temporally coincident conjugate airglow images have ever been presented [*Otsuka et al.*, 2002]. This has particular significance during geomagnetic storms, when irregularities may be generated in the local ionosphere [*Makela et al.*, 2006].

Distribution of Irregularity Scales

The third question is related to the second. That is the question of scales and irregularity location. It is well-known that at large scales (many 10s of km), secondary irregularities tend to grow on the western wall of the depletion under the influence of an eastward neutral wind [*Tsunoda*, 1983]. In the rare event of a westward neutral wind, secondary irregularities may grow on the eastern wall [*Makela et al.*, 2006]. There is also substantial evidence that coherent radar backscatter at the meter-scale range occurs from the center of depletions [*Tsunoda*, 1980; *Otsuka et al.*, 2004b]. Furthermore, the km-scale irregularities that cause radio wave scintillation are difficult to locate because scintillation is an effect that results from the combined action of electron density gradient and irregularity scale [*Yeh and Liu*, 1982].

Coupling to/from Mid-Latitude Instabilities

The fourth, and final, question regards the coupling between low-latitude processes and mid-latitude processes. Mid-latitude medium scale traveling ionospheric disturbances (MSTIDs) are often observed in airglow images in association with what appear to be ordinary equatorial plasma depletions that have surged poleward from the equatorial arcs. Does the depletion trigger a mid-latitude process? Is the the observed "MSTID" truly a MSTID or just a collapsing depletion? Can a mid-latitude process trigger a depletion?

1.6.2 Contribution

This dissertation is devoted to techniques that can assist in answering the questions outlined in the previous section, particularly using multiple remote sensing techniques together and bringing the data into a common format for study. There are primarily three new and significant contributions in this work: The first is to locate scintillation-causing irregularities in three dimensions using radio occultation and airglow imaging. This study suggests that the radio occultation technique for identifying and locating scintillations benefits greatly from additional information. The second contribution is a long-term study of equatorial plasma irregularities from the central Pacific sector. This study confirmed some of the climatological observations from in situ probes and the Jicamarca radar in the American sector while uncovering new and interesting details, as well. One of these interesting details is the third contribution: A secondary peak in depletion activity was identified post-midnight during the November—January period at solar minimum. This was correlated with a high incidence of MSTID structures in the airglow. A physical explanation is provided suggesting that most (if not all) post-midnight depletions are associated with MSTID structures that propagate past the equatorial anomaly crests.

1.7 Outline

Chapter 1 has concerned the general state of ionospheric research and the relationship of this dissertation to it. Chapter 2 surveys the main ionospheric remote sensing techniques utilized in this work, with special attention to radio occultation, coherent backscatter radar, and optical airglow imaging. Chapter 3 develops the basis for the field-aligned airglow observation technique. Chapter 4 proposes a fusion technique to localize irregularities in three dimensions using radio occultation and optical airglow imaging. Chapter 5 discusses a long-term study of airglow and radar data from Haleakala, Maui, Hawaii, and Christmas Island, Kiribati. Chapter 6 presents evidence uncovered during the work presented in Chapter 5 of an alternate depletion seeding process that may explain deviations in the depletion climatology. Chapter 7 concludes with a synthesis of equatorial irregularity formation and detection, placing this work in the larger context and providing some ideas for future directions. A collection of appendices follow at the end, containing information on the data processing approach, the fielding of imaging instruments, and the relative accuracy of geomagnetic field models.

CHAPTER 2

IONOSPHERIC OBSERVATIONS AND REMOTE SENSING

2.1 Introduction

The ionosphere and thermosphere are relatively inaccessible to *in situ* measurements, and the phenomena they host are often best observed remotely. Indeed, the ionosphere was discovered due to its effects on radio waves: refraction, absorption, and scattering. The ionosphere is also the source of naturally occuring airglow emissions that may be used as tracers of plasma and neutral dynamics. This chapter is devoted to these two major ionospheric remote sensing modalities, radio and optical. The radio occultation, coherent radar backscatter, and airglow imaging techniques, which are principal subjects of this dissertation, are covered in detail. Finally, the chapter concludes with some open questions.

2.2 Radio Techniques

2.2.1 Ionosondes

The ionosonde is a simple radar that was originally designed to test the theories of the ionosphere's existence [*Breit and Tuve*, 1925]. An ionosonde transmits RF pulses vertically and detects the delay (2τ) between transmitted and received pulses in order to compute the virtual (constant velocity) heights (h_0) of plasma density layers given a known wave velocity (c_0),

$$h_0 = 2c_0\tau. \tag{2.1}$$

Modern ionosondes transmit coded pulses over a range of frequencies (usually 1–20 MHz) and are capable of identifying different layers and propagation modes automatically. The ionosonde is an important instrument for making HF radio link decisions and for making temporally coarse ionospheric measurements of parameters such as h_{mF2} and n_{mF2} (the height and maximum density of the F region peak, respectively), especially over extended periods of time. However, other radars are superior for studying specific phenomena, such as irregularities associated with equatorial spread-F. An example comparing equatorial spread-F observed by ionosonde and coherent radar backscatter is given in Section 1.4.

2.2.2 Backscatter radar

Phenomenon and Theory

In contrast to ionosondes which leverage the rapidly changing refractive index of the ionospheric plasma in the HF (3–30 MHz) range, backscatter radars are used to study the ensemble behavior of free electrons in the plasma by scattering pulses off of them. These radars operate at higher power levels and higher frequencies, usually in the VHF (30–300 MHz) and UHF (300–3000 MHz) ranges. Frequency choice is motivated by the availability of suitable high-power and low-noise components, location far above the plasma frequency, the ease of creating large aperture antennas, radar wavelength exceeding the plasma Debye length, and the required instrument resolution.

The incoherent backscatter radar was conceived in the late 1950s as a way to understand the ionospheric plasma physics at a more fundamental level [*Gordon*, 1958; *Bowles*, 1958]. The incoherent scatter theory is that the scattered spectra from an ensemble of charged particles in the plasma contain information about the plasma density and temperature. By observing the spectra at different ranges, the electron temperature (T_e) and density (n_e) profiles may be inferred. A complete discussion of incoherent scatter theory, particularly the modeling and inverse problems that must be solved to recover the plasma parameters, is beyond the scope of this work. However, a functional description of the backscatter measurement and the understanding that temperatures and densities may be estimated from incoherent scatter measurements are essential.

For the sake of a non-rigorous illustration, consider a scalar wave with E_b the backscattered electric field at the scattering electrons. The scattered field, E_s, observed at the radar is the superposition of the backscattered fields, E_b, over the scattering volume propagated back to the antenna,

$$E_s = -r_e \sum_p E_b \frac{e^{-jk_0 r_p}}{r_p}. \tag{2.2}$$

The term r_e is the classical electron radius and r_p is the range from the antenna to electron p. Since the scattering region is small, assume that the amplitude variation is small and that only phase differences are consequential (paraxial approximation). Therefore, the backscattered field may be approximated by the product of the incident field, E_i, at the electrons and a phase term representing

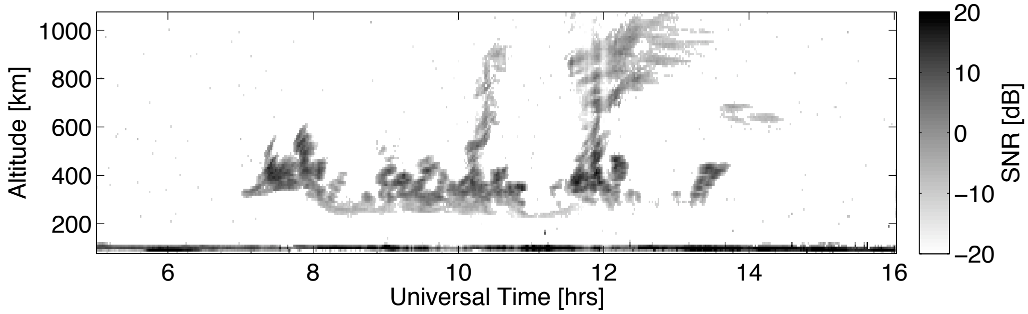

Figure 2.1: Range-time-intensity (RTI) plot of backscatter SNR for the Christmas Island 50-MHz radar on the night of 4 August 2003.

the propagation delay from the transmitter,

$$E_b = E_i e^{-jk_0 r_p}. \tag{2.3}$$

Combining Equations (2.2) and (2.3) yields

$$E_s = -r_e E_i \sum_p \frac{e^{-j2k_0 r_p}}{r_p} \approx \frac{-r_e}{r} E_i \sum_p e^{-j2k_0 r_p}, \tag{2.4}$$

relating the scattered field to the incident field. Notable in Equation (2.4) is the Bragg wavenumber,

$$k_{\text{Bragg}} = -2k_0 = \frac{-4\pi}{\lambda_0}. \tag{2.5}$$

For the purpose of this dissertation, the Bragg wavelength is important because it represents the scale of plasma irregularities that are detectable as coherent radar backscatter. Coherent backscatter can and does occur during incoherent scatter measurements, although study of irregularities that cause it is a research field in itself. Coherent backscatter data are typically aggregated in a range-time-intensity (RTI) or range-time-velocity (RTV) plot, such as that in Figure 2.1, with time on the abscissa, range on the ordinate, and intensities (Doppler velocities) plotted at each point. For equatorial plasma depletions, such a plot represents a "slit camera" observation of irregularities that drift through the radar beam. Figure 2.1 illustrates backscatter from irregularities in both equatorial plasma depletions (above 250 km) and the electrojet (near 100 km).

The "slit camera" observation is a liability in understanding the dynamics which lead to the

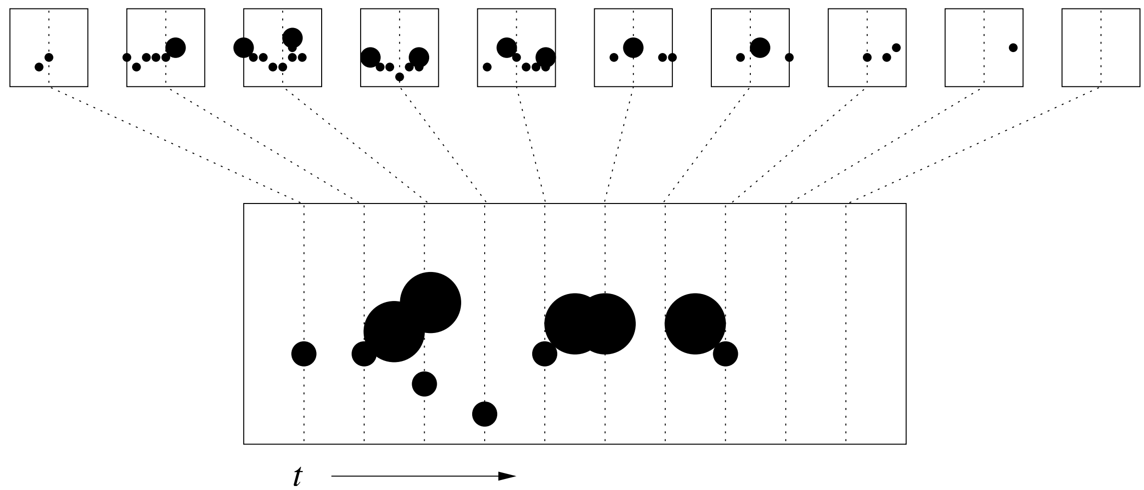

Figure 2.2: A cartoon illustration of the slit camera problem in backscatter radar. The ten panels across the top represent snapshots of an irregularity process that moves left-to-right and evolves with time. The bottom panel is the aggregate of strips from the center of each of the ten panels. It is clear that changes in velocity smear the slit panel image. Irregularities also enter the left side of of the beam fully formed or continue developing once they exit the right side.

formation of depleted plumes and the associated strong coherent backscatter. Figure 2.2 illustrates two of the problems with the slit camera. The first problem is that changes in irregularity velocity cause the RTI plot to smear. This is particularly prominent during periods of increased geomagnetic activity, when the zonal drift may reverse one or more times; but it also skews the interpretation of regular RTI plots, particularly during the growth stages of backscatter plumes when the velocity vector varies rapidly. The second difficulty is observing irregularity developments and precursors. Even if the beam were wide enough to view a large portion of the ionosphere, the resolution would be poor.

Although the considerations in the previous paragraph can be factored into the analysis of RTI plots, the radio imaging technique can alleviate some of the difficulties and provide additional insight into the formation of plasma depletions. Originally, radio imaging was developed by radio astronomers wishing to observe distant radio sources with useful resolution. The first application to ionospheric backscatter radars was in the study of electrojet instabilities [*Kudeki and Sürücü*, 1991]. Radar images are constructed by illuminating the ionosphere with a relatively wide beam and synchronously sampling the backscattered field at multiple locations. Sampling the field over a small region creates (by diffraction) a lens. By way of analog to the pinhole lens in optics, the inversion is related to the Fourier transform [*Woodman*, 1997]. Although this technique creates high-resolution images in space and time, it does not have comparable spatial extent to airglow imaging, for instance.

Figure 2.3 illustrates a sample of frames from a coherent backscatter imaging experiment at Jicamarca, Perú, in 2006 using a maximum-entropy (ME) inversion technique [*Hysell*, 1996; *Hysell et al.*, 2008a]. The intricacy of the irregularities and the level of detail afforded by the imaging radar are quite stunning in comparison to what can be resolved with an RTI plot. Although the radar images have not, as of yet, been rigorously verified by any secondary technique, they are thought to be a good representation of the physics.

Coherent backscatter from irregularities in equatorial plasma depletions is also highly aspect sensitive. That is, the radar beam must be pointed very nearly perpendicular to the geomagnetic field in order to detect coherent backscatter. The 50-MHz radar at Jicamarca, Perú, cannot steer the beam far enough off perpendicular to avoid detecting coherent backscatter. However, one equatorial radar, the ALTAIR (ARPA Long-Range Tracking and Instrumentation Radar) on Roi-Namur island in the Kwajalein Atoll, is capable of steering its beam on and and off-perpendicular to the geomagnetic field. This was used to test the theory that coherent backscatter comes from the depleted portions of equatorial plasma depletions [*Tsunoda*, 1980].

Coherent backscatter, particularly imaging coherent backscatter, is an important tool for understanding irregularity processes. However, it is limited to detecting irregularities at the Bragg scale within the typically narrow radar beam. Other instruments are therefore important in understanding irregularity development, location, and motion.

Christmas Island Radar

The Christmas Island Radar (CXI; geographic: 2.0 N, 202.6 E; geomagnetic: 3.1 N, 273.6 E) is a 50-MHz system presently operated by the U. S. Air Force Research Laboratory (formerly operated by SRI International between 2002–2007) in Kiribati. The antenna is a 100-m $\times$ 100-m co-co type array. Two stationary beams (each with symmetric half-power beam-width of 2.3°) have been operational since 2002 (east) and 2003 (north). The east beam (elevation: 60.5°; azimuth: 90.0°) provides backscatter data slightly to the east of the CNFI field of view. The north beam (elevation: 84.5°; azimuth: 0.0°) provides observations within the same geomagnetic volume as a pair of airglow imagers operating from Hawaii (discussed in Section 2.3.3). That is, the range gate centroid locations of the north beam reside on geomagnetic field lines that intersect the airglow observed by the imagers north of the geomagnetic equator. In its present configuration, the radar provides backscatter SNR and Doppler velocities at 100$\times$ 10-km (in altitude) range gates on each of the two beams every 75 seconds.

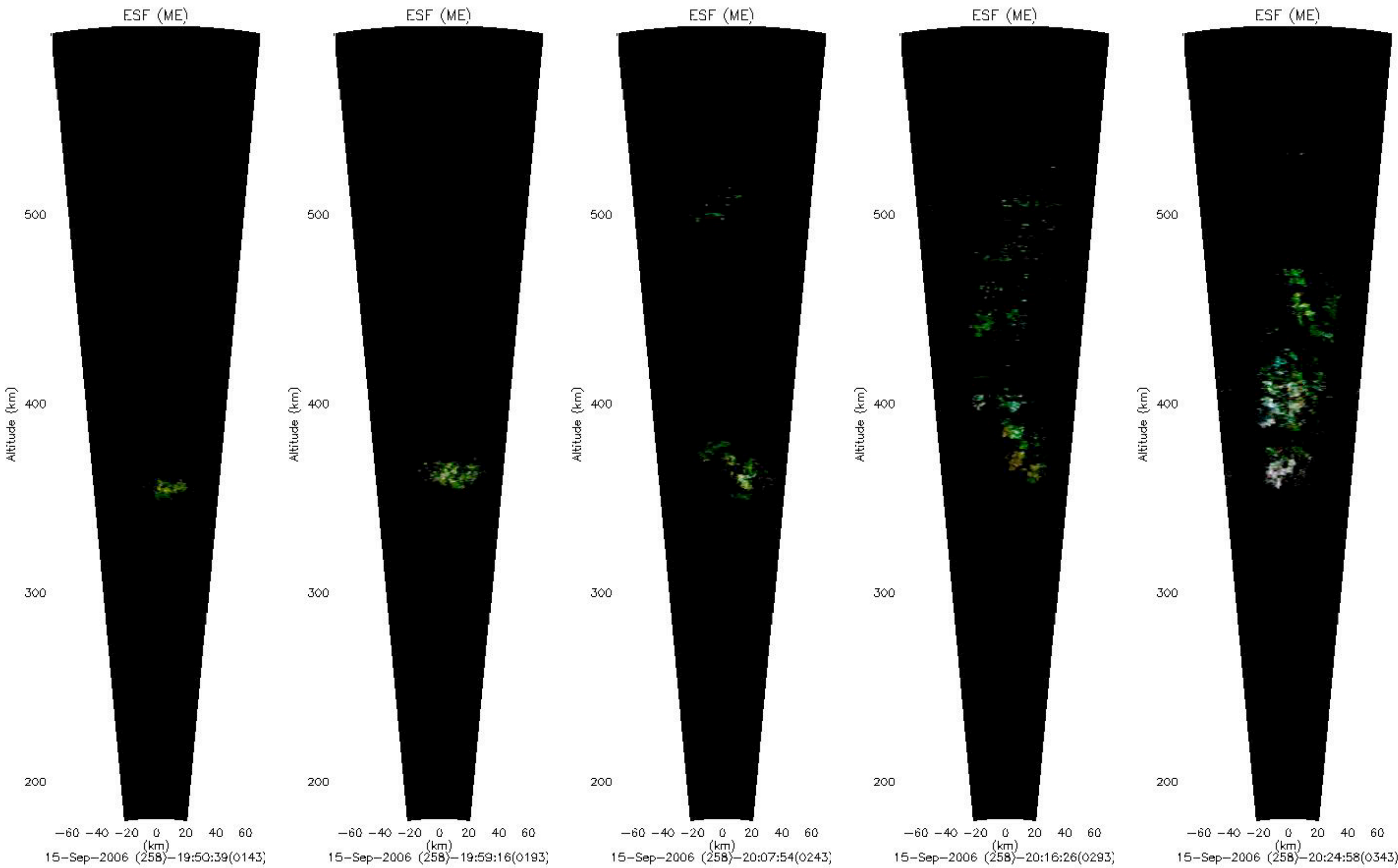

Figure 2.3: Radar images of plasma bubble formation from Jicamarca, Perú. The images are approximately 9 minutes apart. The first three frames show "bottom side" irregularities at 350 km and the last two show irregularities forming up to about 500 km. (Figures courtesy of Jicamarca Radio Observatory.)

2.2.3 Satellite beacons

Forward scatter, or bistatic, measurements utilize a transmitter and receiver at different locations. For this work, we are interested primarily in forward scatter measurements made with either the transmitter or receiver (or both) on spacecraft. The first artificial Earth satellites employed radio beacons to facilitate tracking. It was soon discovered that rapid variations (much more rapid and irregular than the Doppler shift) were present on the received satellite signal. Although the first recorded observation of scintillation came from radio star (pulsar) observations a decade earlier, artificial satellite beacons provided a calibrated means to observe irregularities in the ionosphere.

Satellite beacons on multiple frequencies far above the plasma frequency can also be used to determine the total electron content (TEC) along the path between the transmitter and receiver via the dispersive properties of the plasma. From the Appleton-Hartree formula in the high-frequency limit,

$$n(z) = \sqrt{1 - \frac{\omega_p^2(z)}{\omega^2}}. \tag{2.6}$$

The plasma frequency, ω_p, can be derived by slightly displacing a parcel of plasma of known density n_e and allowing it oscillate at its natural frequency,

$$\omega_p = \sqrt{\frac{n_e q_e^2}{\epsilon_0 m_e}} \approx 2\pi\sqrt{80.6 n_e}, \tag{2.7}$$

where $q_e = 1.609 \times 10^{-19}$ C/e^- is the fundamental unit of electronic charge, $m_e = 9.109 \times 10^{-31}$ kg/e^- is the mass of an electron, and $\epsilon_0 = 8.854 \times 10^{-12} \mathrm{m}^{-3} \cdot \mathrm{kg}^{-1} \cdot \mathrm{s}^4 \cdot \mathrm{A}^2$ is the permittivity of free space. Let the group path (S_g) be the effective distance traveled by a wave packet through the dispersive plasma in the course of the group delay (τ),

$$S_g = c_0 \tau = \int_{z_0}^{z_0+z} \frac{dz'}{n(z')}. \tag{2.8}$$

Dividing through by c_0 and taking a Taylor series approximation for the group refractive index ($n_g = 1/n$) yields

$$\tau \approx \frac{1}{c_0} \int_{z_0}^{z_0+z} \left(1 + \frac{1}{2}\frac{\omega_p^2(z')}{\omega^2}\right) dz', \tag{2.9}$$

which can be simplified to

$$\tau \approx \frac{z}{c_0} + \frac{1}{2c_0\omega^2} \int_{z_0}^{z_0+z} \omega_p^2(z') dz'. \tag{2.10}$$

We solve Equation (2.7) for n_e and integrate to obtain TEC,

$$\text{TEC} = \int_{z_0}^{z_0+z} n_e(z')dz' = \frac{\epsilon_0 m_e}{q_e^2} \int_{z_0}^{z_0+z} \omega_p^2(z')dz'. \tag{2.11}$$

That is,

$$\int_{z_0}^{z_0+z} \omega_p^2(z')dz' = \frac{q_e^2}{\epsilon_0 m_e}\text{TEC}. \tag{2.12}$$

We can insert this result into Equation (2.10) to obtain

$$\tau \approx \frac{z}{c_0} + \frac{q_e^2}{2c_0\epsilon_0 m_e \omega^2}\text{TEC}. \tag{2.13}$$

Given two temporally coincident (phase-coherent at the transmitter) group delays (τ_1, τ_2), we can compute the TEC as

$$\text{TEC} \approx \frac{2c_0\epsilon_0 m_e (\tau_1 - \tau_2)}{q_e^2} \frac{\omega_1^2\omega_2^2}{\omega_1^2 - \omega_2^2}. \tag{2.14}$$

Converting the frequencies from angular (rad/s) to time (Hz) and applying the approximation from Equation (2.7) yields

$$\text{TEC} \approx \frac{c_0 (\tau_1 - \tau_2)}{40.3} \frac{f_1^2 f_2^2}{f_1^2 - f_2^2}. \tag{2.15}$$

TEC is typically specified in e^-/m^2 or in "TEC units" (TECU, 10^{16} e^-/m^2). When observed over a path that traverses the entire ionosphere such as Earth's surface to the Global Positioning System (GPS), TEC serves as a relative measure of plasma density over the surface of the Earth. For comparison, TEC measurements are often projected onto the surface normal vector of the Earth. This product is called vertical TEC (VTEC). The plasmasphere also contributes some electron density to TEC observations made using GPS. This contribution is generally small during the day, but may become significant at night during solar minimum conditions when the ionospheric contribution to TEC is low. TEC is also useful in "ray" tomography problems [e.g., *Austen et al.*, 1988; *Kunitsyn and Tereshchenko*, 2003; *Lee et al.*, 2008]. A special case of the ray tomography problem is radio occultation, discussed in Section 2.2.3.

One of the problems with the TEC technique is removing the biases introduced by the transmitter and receiver circuitry when determining the actual delays, τ_1 and τ_2. In the case of GPS, the correction terms are broadcast regularly, but the receiver biases must also be removed. For ground-based receivers, a simple technique normalizes all of the observations made by a given receiver to the lowest TEC observed just before dawn. There are also estimation and filtering techniques that may be applied to this problem given sufficient data. For the case of space-based receivers and transmitters, the TEC can be plotted as a function of distance between the two satellites. Extrapolating the distance to zero yields both the transmitter and receiver biases directly (P. Bernhardt, personal communication, 2007). This extrapolation technique does not work well when distances are large or slowly varying, as is the case for GPS. However, it is useful with many of the low-Earth orbiting beacon transmitters and receivers.

The Global Positioning System

GPS provides precision location and altitude information world wide through a constellation of 32 satellites. Each satellite broadcasts coded time signals on several frequencies, which are combined at the receiver to determine location. As a remote sensing tool, the GPS is fundamentally similar to other satellite beacons. However, it has the advantage of a synchronized, stable clock system, and global coverage. GPS is particularly interesting for ionosphere studies because it is both a remote sensing tool and an application space for the results of ionospheric research.

GPS operates on the principle of time-of-arrival (TOA), illustrated in Figure 2.4. Synchronized pulses from three transmitters $\{A, B, C\}$ at known locations are received at Z. The estimated range to a given satellite under assumption of a known constant propagation velocity (c_0, the speed of light in a vacuum) is called the *pseudorange*. Equation (2.16) is a simplified version of the pseudorange equation. In the pseudorange equation, ρ is the true range to the satellite, ε is the error (including ionospheric TEC and hardware biases, discussed earlier, among others) in the pseudorange, and τ is the measured time delay between the satellite and the receiver.

$$P = \rho + \varepsilon = c_0\tau. \tag{2.16}$$

Orbital information for each satellite is provided in the form of ephemerides broadcast by the satellites. This allows the satellite position to be accurately fixed during solution for the user location. Most of the components of the error term ε are corrected using information included with the ephemerides. However, environmental errors not associated with satellite hardware are often difficult to parameterize. Particularly of interest are the delays introduced by variations in the refractive indices of the Earth's atmosphere and ionosphere. Herein lies the problem of interest. Through the delay mechanism discussed above in association with TEC measurements, the presence of electron density gradients causes GPS navigation solutions to become inaccurate on the order of a few meters. Large gradients, such as those observed during major storms, may degrade the navigation solution further to the order of tens of meters. Although scintillation is usually associated with gradients in electron density, the rapid fading may also cause the tracking algorithm in the receiver to lose lock on the GPS signal.

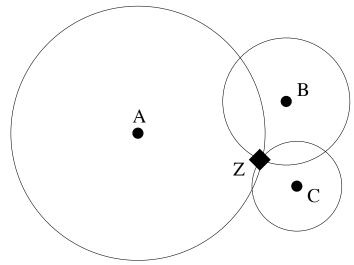

Figure 2.4: Illustration of the time-of-arrival principle applied to GPS. Three transmitters labeled $\{A, B, C\}$ produce synchronized pulses that are received at Z. By computing the transit times of the pulses, the location of Z can be fixed.

The GPS signal is spread-spectrum BPSK with a 50-Hz data rate. Two different frequencies are presently used for GPS. Consumer-grade GPS units lock onto the *Coarse / Acquisition* (C/A) code broadcast on the GPS L_1 frequency of 1.57542 GHz. Another code, the so-called *Precise-Encrypted* (PY) code, inaccessible to civilian users, is broadcast both at L_1 and at frequency L_2, 1.22760 GHz. Although the coded data from L_2 are not accessible to civilians, receivers with high-stability local oscillators can track the phase difference between the L_1 and L_2 signals without decoding L_2. This technology allows TEC measurements through the technique discussed in the previous section (e.g., Equation (2.15)). The two frequencies may also be used to correct for dispersive transmission delays in the ionosphere through a related procedure. However, the *codeless* tracking on L_2 requires higher SNR than the C/A signal on L_1 and is more susceptible to scintillation.

Another technique for improving the accuracy of single-frequency GPS receivers is differential GPS. Differential GPS employs one or more well-surveyed receivers whose observations are combined with the observations of the unknown receiver to yield a navigation solution with improved accuracy. A widely deployed differential GPS service is the Wide-Area Augmentation System (WAAS). WAAS employs a network of reference receivers throughout the United States. While WAAS can correct for large scale temporal and spatial variations in the ionosphere, its accuracy does break down under certain cases, particularly during intense geomagnetic storms, when smaller scale electron density structures often form in the midlatitude ionosphere.

GPS receivers have also been employed as scintillation monitors [*Beach and Kintner*, 2001]. Since the irregularities and the satellites are in motion with respect to the receiver, the interpretation of the data requires careful effort [e.g., *Ledvina et al.*, 2004; *Kintner et al.*, 2004]. One way to mitigate the effect of satellite motion is to use the WAAS signal, which is broadcast from geostationary orbit [*Cerruti et al.*, 2006; *Ledvina and Makela*, 2005].

Radio Occultation

The premise behind occultation is that a space-based transmitter and space-based receiver have established a radio communication link. As one of the two stations passes behind a planet, the communication signal is lost, or occulted. However, at the *immersion* and *emersion* points, where the transmitting station is just setting and rising, respectively, the signal is bent slightly as it passes through the planet's atmosphere. Figure 2.5 illustrates immersion in cartoon form, although the bending angle is slightly exaggerated.

Occultation has a long history in planetary astronomy. The first suggestion for optical observations was by *Pannekoek* [1903]. The idea is that a varying intensity (due to extinction) of a star occulted by a planet should yield the atmospheric scale height. However, this measurement was impractical until photometry advanced sufficiently. Even then, the measurement is noisy due to seeing conditions[1] for terrestrial telescopes. The first radio occultation experiment was completed using supernova remnant IC 443 and the moon in 1955 [*Elsmore and Whitfield*, 1955]. This measurement was repeated in 1956 using the Crab Nebula [*Elsmore*, 1957]. The modern era of radio occultation began with the Mariner IV spacecraft as it flew by Mars on 15 July 1965 [*Kliore et al.*, 1965].

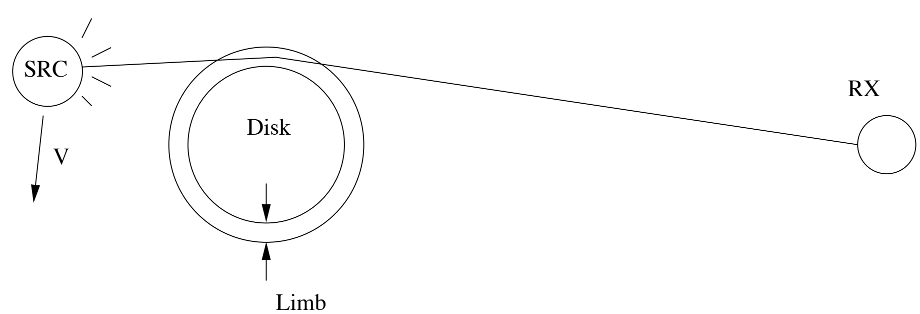

Figure 2.5: Cartoon of immersion occultation geometry. The bending angle is exaggerated for effect.

In the Mariner experiments, the spacecraft and Earth stations were used as transmitters and receivers, respectively, to probe the atmospheres of Venus and Mars. The Voyager spacecraft sent to the outer planets of the Solar System also employed this particular occultation geometry to study not only planetary atmospheres, but also ring systems [*Marouf et al.*, 1986]. Early in the U.S. space program, plans were laid for occultation experiments involving two orbiters [*Harrington*

[1]Atmospheric turbulence also affects light from extraterrestrial sources. In astronomy circles, "good seeing" is the qualitative term for little variation in intensity.

et al., 1970]. While this was a substantial undertaking for other planets, it suddenly became feasible for the Earth when space-based navigation systems were installed. The introduction of the Global Positioning System (GPS) spurred a renaissance for the occultation idea. The GPS/MET satellite launched in the mid-1990's was intended as a testbed for GPS occultation technology. Other programs such as CHAMP and IOX became operational in 2000 and 2001, respectively. More recently, six COSMIC/FORMOSAT-3 satellites were launched in April 2006 as a partnership between the University Corporation for Atmospheric Research (UCAR) in the United States and the Taiwanese Space Agency [*Cheng et al.*, 2006].

Radio occultation leverages phase measurements of phase-coherent signals at two or more different frequencies to obtain either the ray bending angle (for neutral atmosphere) or the TEC (for ionosphere). Initially, the Mariner phase measurement data were inverted by comparing the observations to a forward model for the Martian atmosphere [*Kliore et al.*, 1965]. However, subsequent inversions employed the Abel transform relationship and the assumption of spherical symmetry to solve for the refractive index profile. The refractive index profile is then inverted via forward model for the neutral or electron density profile [*Fjeldbo et al.*, 1971].

Occultation is a projection problem in the sense that the properties of the medium along the ray path at each sample step affect the resulting measurement. In contrast to most other projection problems such as those in medical imaging, occultation is constrained by instrument density to be a very limited angle problem. A tomographic reconstruction is not possible in the traditional sense. However, by modeling the atmosphere as a set of spherically symmetric layers ("voxels" to borrow the tomography term), the density (refractivity) of each layer can be inverted to produce a profile. Since the region over which the occultation occurs is a surface ("plane"), it is common to flatten the problem into two dimensions. In two dimensions the analytical formulation is the so-called Abel transform. Referring to Figure 2.6, the two-dimensional Abel transform amounts to the projection (Equation (2.17)) of a circularly symmetric function ($f(r)$) along a line-of-sight (p) parallel to the x-axis:

$$f_A(a) = \int_{-\infty}^{\infty} f(r) dx. \tag{2.17}$$

For any point (x, a), $r = \sqrt{x^2 + a^2}$. Therefore, we invoke the chain rule to change dx to dr in the Abel projection integral. Substituting the new differential and noting the symmetry involved, we write

$$f_A(a) = \int_{-\infty}^{\infty} \frac{f(r)\, r\, dr}{\sqrt{r^2 - a^2}} = 2 \int_{a}^{\infty} \frac{f(r)\, r\, dr}{\sqrt{r^2 - a^2}}. \tag{2.18}$$

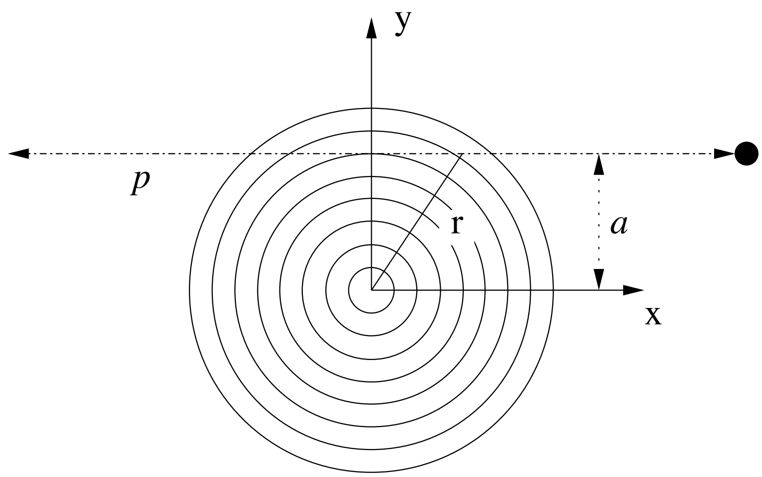

Figure 2.6: Abel transform geometry.

There are generally two approaches to solving this inverse problem for $f(r)$. The first, and original, technique is to evaluate the analytical inverse of the Abel transform numerically,

$$f(r) = -\frac{1}{\pi}\int_r^\infty \frac{df_A(a)}{da}\frac{da}{\sqrt{a^2 - r^2}}. \tag{2.19}$$

One such numerical technique is termed “onion peeling.” The assumption is that the area over which spherical (circular) symmetry is required is smallest at the highest altitude shell for which data are available. As the name suggests, onion peeling starts at the highest shell and works down, evaluating Equation (2.19) by quadrature, layer by layer. Although the error response of such a technique is relatively good on the topside, errors compound rapidly as the ray descends and the size of the required region of symmetry grows. The second technique recognizes that the discrete form of the integral transform in Equation (2.18) can be cast as

$$\mathbf{f_A} = \mathbf{G}\,\mathbf{f}. \tag{2.20}$$

In this case, there may exist a whole host of generalized inverses $\mathbf{G}^\dagger$ for the transform $\mathbf{G}$, each with different smoothing and noise response properties. At the time of this writing, the COSMIC and CHAMP occultation data were processed using a form of the onion peeling algorithm [*Lei et al.*, 2007]. The only known study of matrix inverse methods for this problem was performed on modeled data [*Hysell*, 2007].

The input, $f_A(a)$, of Equation (2.19) for ionospheric problems is the calibrated suborbital total electron content: the TEC within the satellite orbit ellipse. This is obtained by measuring the

TEC from the receiver to the GPS satellite as a function of ray tangent altitude on either side of the ray tangent point. On each side of the tangent point, there is a TEC measurement with the same tangent altitude. The difference between these measurements approximates the TEC below the receiver orbit. Naturally, this estimate is considerably better if the occultation is (nearly) in the orbit plane of the receiver. The value of the suborbital TEC is constrained to approach zero as the ray tangent altitude approaches the satellite altitude. This motivates the onion-peeling inversion by starting with the shortest ray paths (those supposed to have the most local spherical symmetry) and working downward.

In the absence of other data sources, classical radio occultation utilizing spherically symmetric shells is a credible technique. However, as we will soon see, the spherical symmetry assumption is easily violated. Figures 2.7 and 2.8 illustrate the effects of the spherical symmetry assumption under daytime conditions with few irregularities and nighttime conditions with irregularities, respectively. Each of these figures has three panels containing occultation data from the COSMIC experiment. On the left is the suborbital TEC as a function of ray tangent altitude. The center is the Abel electron density inversion provided as a data product by the UCAR COSMIC program. The right is the SNR reported by the receiver as a function of ray tangent altitude. The inversion in Figure 2.7 is both relatively smooth and mostly positive. However, the inversion in Figure 2.8 is both ragged and negative up to 225 km. The presence of negative values (or unrealistic positive ones) suggests that the inverse Abel transform has redistributed the electron density in the spherical shells to explain meridional or longitudinal gradients in electron density. Notice also in Figure 2.8 that the GPS L_1 SNR undergoes scintillation from about 175 to 350 km. This suggests that small-scale electron-density irregularities are present, likely in conjunction with large-scale equatorial plasma depletions. This was confirmed by an airglow imaging system operating on the ground.

The spherical symmetry problem is an invitation to creativity in assimilating data from other sources. A few researchers have combined ground-based GPS VTEC data with GPS occultation data [*Hernández-Pajares et al.*, 2000]. This can also be accomplished as a tomography problem, which relies on a high density of ground receivers in addition to one or more well-placed occultations (J. Lee, personal communication, 2007).

The SNR and excess phase measured at the occultation receiver can also be used to study irregularities. This is a relatively recent development that requires special attention to detail because the transmitter, receiver, and irregularities, are all in motion. Furthermore, the data rates (typically 1-Hz) provided by the early radio occultation satellites tended to under-sample irregularities. Scin-

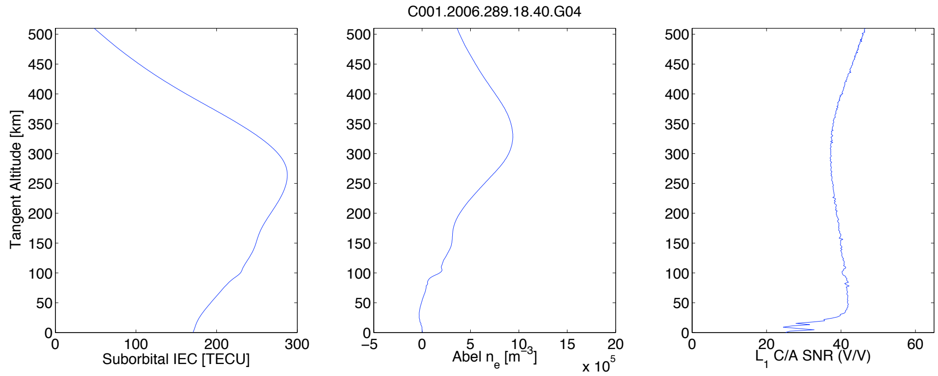

Figure 2.7: Occultation inversion during the mid-day time period. The left plot shows the calibrated TEC as a function of the ray tangent altitude. The center plot is the inverted electron density profile. The right plot is the SNR on the GPS L_1 frequency. Data provided courtesy of the UCAR COSMIC Project Office.

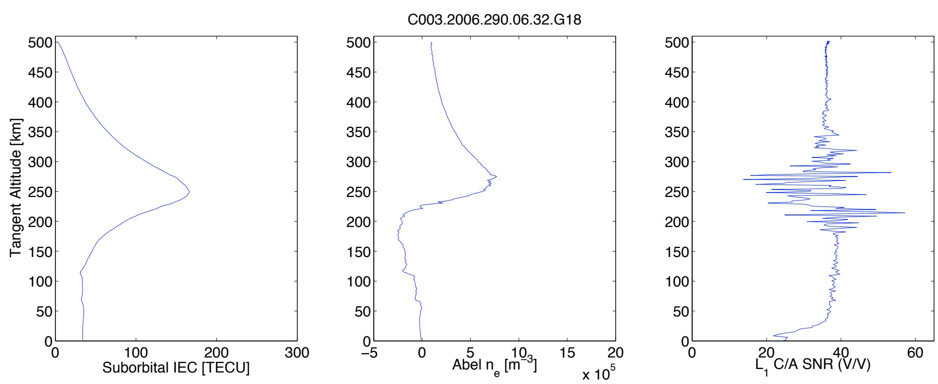

Figure 2.8: Nighttime occultation inversion in the presence of irregularities at many scales. The left plot shows the calibrated TEC as a function of the ray tangent altitude. The center plot is the inverted electron density profile. Notice that the inverted profile is negative up to 225 km. This is an artifact of the spherical symmetry assumption in an atmosphere that is not spherically symmetric. The right plot is the 1-Hz SNR on the GPS L_1 frequency. Large, rapid fluctuations occur over most of the occultation. This suggests that small-scale irregularities (which may be associated with equatorial plasma depletions) are present. Data provided courtesy of the UCAR COSMIC Project Office.

tillation indices such as the S_4 cannot be interpreted in the same way for these measurements as for the 50-Hz sampled ground-based measurements. This is because both the satellite and the receiver are in motion, whereas terrestrial scintillation observations only have the satellite moving (in the Earth frame). However, as we will see in Chapter 4, a short-time increase in the SNR variance does indicate the presence of irregularities along the ray path [*Miller and Makela*, 2008]. The geographic distribution and magnetic aspect angles of scintillation irregularities have been studied in a coarse manner utilizing the SNR variance (called "S_4" by the authors) [*Straus et al.*, 2003; *Anderson and Straus*, 2005]. However, the assumption is made that the irregularities are occurring at the ray tangent point.

2.2.4 Irregularity imaging with occultation

The irregularity localization problem can also be approached from the standpoint of diffraction tomography or inverse scattering [*Sokolovskiy et al.*, 2002; *Gorbunov et al.*, 2002; *Gorbunov and Gurvich*, 1998; *Bojarski*, 1982]. Fundamentally, this amounts to invoking Huygens' principle, which arises from solving the Helmholtz equation

$$(\nabla^2 + k^2)u = 0. \tag{2.21}$$

Given samples of the complex field along the perimeter of a region, we can reconstruct the irregularities within the region. If the field is stationary in time and is uniformly sampled along a straight line in a two-dimensional plane, the problem reduces to a phase-shift in Fourier space,

$$\mathcal{F}\{u\} = \mathcal{F}\{u_0\} \exp\left(-jz\frac{k_x^2}{2k}\right), \tag{2.22}$$

where $\mathcal{F}\{\cdot\}$ is a Fourier transform operator, z is the distance from the sample line, k_x is the angular displacement $[-\pi, \pi]$ along the samples $u_0(k_x)$, k is the radio-frequency wavenumber, and $u(k_x, z)$ is the unknown field [e.g., *Ratcliffe*, 1956]. Figure 2.9 illustrates an example of this kind of reconstruction. The forward diffraction field (top) is generated for a thin phase screen of irregularities at $x = 100$ and the radio source at $x \to -\infty$. The forward field is sampled at $x = 200$ and reconstructed (bottom). The point ($x = 100$) in the reconstructed field at which the rays appear "focused" with minimum amplitude variation is the location of the irregularities.

Since satellite orbits are elliptical, it is sensible to attempt a solution of Equation (2.21) in two

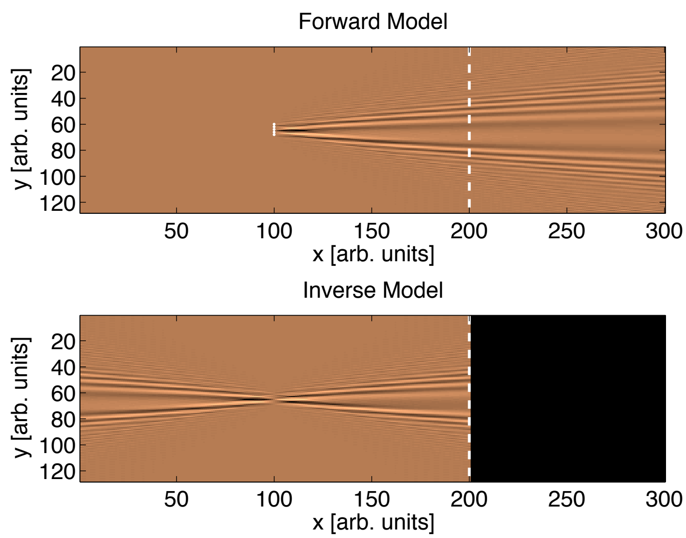

Figure 2.9: Forward (top) and inverse (bottom) models of diffraction due to irregularities at $x = 100$. The forward field was sampled at $x = 200$. In the inverse model, the reconstructed field exhibits a focusing effect at $x = 100$. This indicates the position of the irregularities.

dimensions. After *Gorbunov and Gurvich* [1998], the solution is

$$u(x) = \sqrt{\frac{k}{2\pi}} \int_S \frac{u_0(y) \cos \psi_{xy} \exp(-jk|x-y| + j\pi/4)}{\sqrt{|x-y|}} dS_y, \tag{2.23}$$

where $u_0(y)$ are the samples of the field along the satellite orbit, x is the location of the reconstructed field, y is the location of the satellite, and ψ_{xy} is the angle between the vector $x - y$ and the normal to the curve, $\hat{\mathbf{a}}_n$. The complex field samples $u_0(y)$ are obtained from the GPS receiver SNR and excess phase measurements.

In order to take advantage of the spatial reduction to two dimensions, it is necessary to assume that the irregularities are field-aligned [*Sokolovskiy et al.*, 2002]. The two-dimensional flattening also destroys the physical interpretation of the reconstructed field. However, if the irregularities form a thin phase screen, they can be detected by the focusing technique described above. Figure 2.10 illustrates the geometry of this problem when flattened to two dimensions. The diffraction tomography approach has never been directly verified against other techniques. Some of its proponents claim to have detected irregularities at an altitude of 1300 km [*Sokolovskiy et al.*, 2002]. While scintillation-scale irregularities have been detected near 800 km using forward-scatter [*MacDougall*, 1981] (mid-latitude case) and rocketry [*Jahn and LaBelle*, 1998] (equatorial case), this claim seems to be somewhat dubious. Refinement of this technique or a complimentary technique might allow

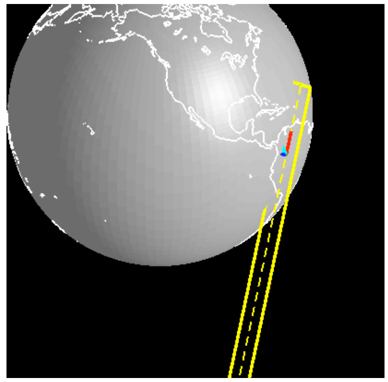

Figure 2.10: Geometry of the two-dimensional diffraction tomography ("back propagation") problem. The receiver is in low-Earth orbit over the eastern Caribbean. The GPS satellite is far below the figure. The 2-D solution is computed in the plane drawn tangent to Earth's surface.

it to become more robust, and therefore more valuable, in the future. One such complimentary technique is presented in Chapter 4.

2.3 Optical Imaging Techniques

Optical remote sensing of the ionosphere predominantly occurs through airglow detection. Airglow is light given off as ions in the ionosphere change energy levels due to ion-electron recombination or high-energy particle impacts. The aurorae, which are the most commonly recognized airglow emissions, are primarily due to high-energy particle impact. However, at lower latitudes, the primary airglow emissions of interest are due to recombination. During the day, solar radiation drives production. After sunset, the ions and electrons recombine to form neutral species again. These recombination processes yield airglow emissions used as dynamic tracers in the low- and mid-latitude ionosphere. Because airglow emissions at low and mid-latitudes tend to be rather weak (below the threshold of human perception), narrow bandwidth color filters are used in conjunction with long (on the order of minutes) exposure times and sensitive photon counters.

As equatorial depletions grow in altitude, internal polarization electric fields map efficiently along the geomagnetic field (an effect that will be discussed in Chapter 3), pushing them into the low- and mid-latitude regions north and south of the geomagnetic equator. There, the depleted plasma appears as a dark region in the airglow, allowing wide-area spatial maps to be made of the depletions.

Airglow observations represent a complex product of sensor and optics, observation geometry, chemistry, neutral dynamics, and electrodynamics. In the following subsections, we will investigate many of these relationships, especially plasma chemistry, instrumentation, calibration, and signal processing. The details of geomagnetic field-aligned imaging will be reserved for discussion in Chapter 3. A short discussion of the practical aspects of installing and operating an airglow imager is found in Appendix B.

2.3.1 Airglow chemistry

There are predominantly two airglow emission lines that are useful for ground-based F-region studies in the equatorial region. One is the 630.0-nm "red" line. The other is the 777.4-nm line in the infrared. These emissions arise from atomic oxygen energy transitions, as illustrated in Figure 2.11.

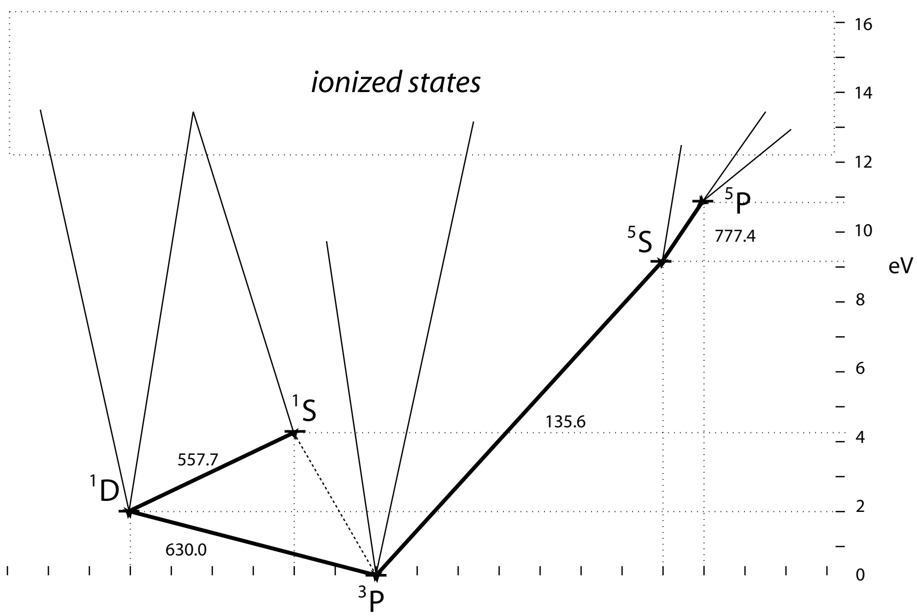

Figure 2.11: Simplified OI transition diagram showing commonly observed equatorial airglow emissions. This figure is a considerably simplified version of Figure 1 in *Tinsley et al.* [1973]. There are a number of high-energy states with transitions that populate the ^1D and ^5P states that are not shown here.

The 630.0-nm "red" line that results from the dissociative recombination of O_2^+ is easiest to observe, although the chemistry and dynamics are a little more complex. This discussion is based on work by *Makela and Kelley* [2003b]; *García* [1999]; *Link and Cogger* [1988]. O_2^+ is formed from the collision between O^+ and molecular oxygen (O_2),

$$O^+ + O_2 \rightarrow O_2^+ + O. \tag{2.24}$$

One dissociative recombination reaction of O_2^+ yields

$$O_2^+ + e^- \rightarrow O(^1D) + O(^3P) + 4.99\,\text{eV}. \tag{2.25}$$

Although $O(^1D)$ may be lost through several mechanisms, the 630.0-nm emission arises from the relaxation

$$O(^1D) \rightarrow O(^3P) + h\nu. \tag{2.26}$$

The $O(^1D)$ state has a lifetime of 110 s. This is important because the $O(^1D)$ population may be advected by dynamics, causing the image to blur.[2] The transition produces a photon ($h\nu$) at 630.0 nm.

The volume emission rate of the 630.0-nm emission has contributions from a number of sources, which are summarized in this rate equation [*Link and Cogger*, 1988]:

$$\eta_{630.0} = \frac{0.76\beta_{^1D}k_1[O^+][O_2]}{1 + (k_3[N_2] + k_4[O_2] + k_5 n_e)/A_{^1D}}. \tag{2.27}$$

The values of the coefficients [from *Link and Cogger*, 1988] are given in Table 2.1. Coefficient k_1 relates the production of O_2^+ ions to the densities O^+ and O_2, which are dominant ion and neutral components at F-region altitudes. Coefficient $\beta_{^1D}$ reflects the rate of production of $O(^1D)$ from the dissociative recombination reaction in Equation (2.25). Dissociative recombination of O_2^+ also yields significant populations of $O(^3P)$ and $O(^1S)$, which can be seen in the context of airglow emissions in Figure 2.11.

Table 2.1: Reaction Rate Coefficients for the 630.0-nm Emission

Reaction	Coefficient	Value
$O_2^+ + e^- \rightarrow O(^1D) + O(^3P) + h\nu$	$\beta_{^1D}$	1.1
$O^+ + O_2 \rightarrow O_2^+ + O$	k_1	$3.23 \times 10^{-12} \exp\left(\frac{3.72 \cdot 300}{T_i} - \frac{1.87 \cdot 300^2}{T_i^2}\right)$ cm^3·s^{-1}
$O(^1D) + N_2 \rightarrow O(^3P) + N_2$	k_3	$2.0 \times 10^{-11} \exp\left(\frac{111.8}{T_e}\right)$ cm^3·s^{-1}
$O(^1D) + O_2 \rightarrow O(^3P) + O_2$	k_4	$2.9 \times 10^{-11} \exp\left(\frac{67.5}{T_e}\right)$ cm^3·s^{-1}
$O(^1D) + e^- \rightarrow O(^3P) + e^-$	k_5	$1.6 \times 10^{-12} T_e^{0.91}$ cm^3·s^{-1}
$O(^1D) \rightarrow O(^3P) + h\nu$	$A_{^1D}$	6.81×10^{-3} s^{-1}

A typical emission profile of the 630.0-nm red line emission generated from Equation (2.27) is shown in Figure 2.12 along with the electron and molecular (diatomic) oxygen densities. The peak emission altitude and the altitude of peak electron density are marked, as well as one neutral

[2]This might be something, however impractical, to explore as a remote sensing technique.

scale-height below the electron density peak.

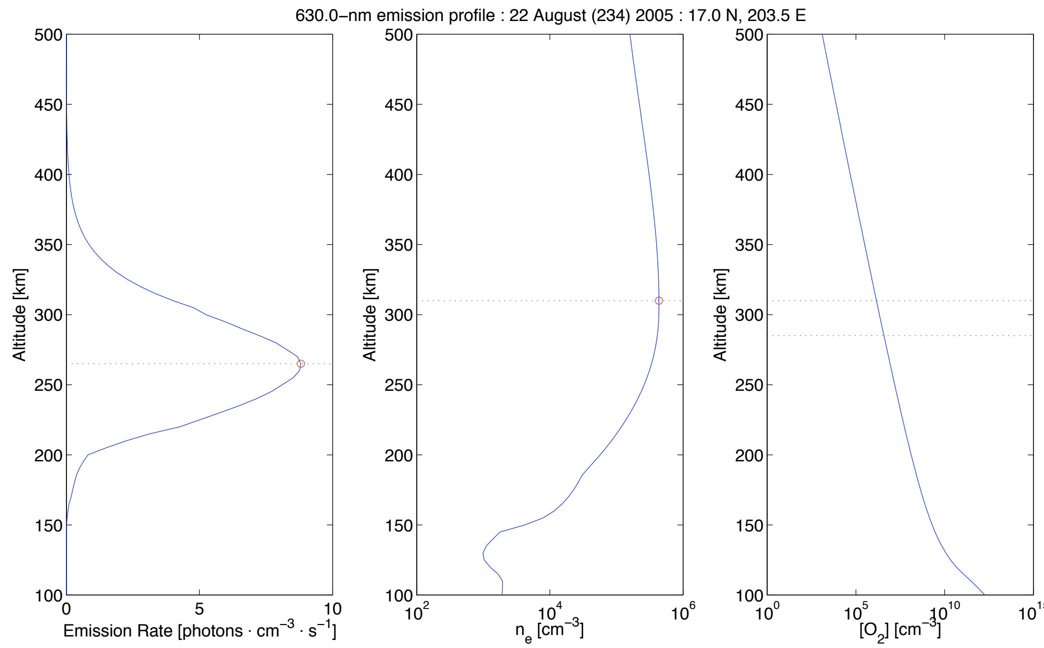

Figure 2.12: 630.0-nm emission profile compared to n_e and $[O_2]$ profiles. Peak emission/density altitudes are indicated by the horizontal line and marker ($\circ$). In the oxygen profile, the electron density peak altitude and scale-height are indicated.

The 777.4-nm emission arrises from the radiative recombination of O^+,

$$O^+ + e^- \rightarrow O(^5P). \tag{2.28}$$

And a photon is given off at 777.4 nm,

$$O(^5P) \rightarrow O(^5S) + h\nu. \tag{2.29}$$

The 777.4-nm emission occurs promptly. From Equation (2.28) and Figure 2.11, it is apparent that the rate of $O(^5P)$ production, and hence 777.4-nm photon production, is related to the product of the O^+ and electron densities. Given that the dominant ion at the F region peak is O^+ and assuming that the ionosphere is electrically neutral, such that $n_e = n_i \approx [O^+]$, the volume emission rate of 777.4-nm photons is proportional to the square of the electron density, as described by Equation (2.30). This is also true of the 135.6-nm emission observed by the GUVI and IMAGE instruments, which comes from a related reaction [e.g., *DeMajistre et al.*, 2004]. The 135.6-nm emission also has a different constant (α) relating its volume emission rate to the electron density.

$$\eta_{777.4} \approx \alpha_{^5S} n_e^2. \tag{2.30}$$

There is also an ion-ion recombination contribution to the 777.4-nm emission that is frequently negligible and beyond the scope of this work.

2.3.2 Intensity interpretation

Whereas the volume emission rate, and therefore the intensity, of the 777.4-nm emission is directly related to the electron density, the emission rate for the 630.0-nm emission is jointly dependent on the density of O_2 and electrons. Because O_2 is a neutral species, its distribution is not strongly influenced by electrodynamic processes. As the electrons (in the F-region peak) move upward, there is less O_2, and the 630.0-nm emission becomes weaker. Likewise, as the F region descends, the 630.0-nm emission intensifies.

This ambiguity becomes particularly important when differentiating classes of structures, notably MSTIDs (medium-scale traveling ionospheric disturbances) and equatorial plasma depletions. MSTIDs are predominantly observed as undulations in the ionosphere height and to a lesser extent changes in density, whereas depletions exhibit considerably larger electron density variations. However, to the untrained eye, they may appear to have similar characteristics in an airglow image.

In an all-sky imaging system, the optical extinction of the atmosphere and the thickness of the airglow layer become important. At low elevation angles, the ray path lengths in the atmosphere and the airglow layer are longer than they are at zenith. For a narrow-field imaging system such as those predominantly utilized in this work, this consideration is less important. For a discussion of these effects, consult *García* [1999].

2.3.3 Instrumentation

An airglow imaging system consists of several major components (see *Mendillo and Baumgardner* [1982] for an early example of this architecture). Light enters the system through an objective lens. It is then re-imaged to be approximately telecentric as it passes through a narrow filter to select the emission wavelength of interest. Filters are switchable using a rotating wheel. The final block of optics focuses light exiting the filter onto the detector. The earliest airglow images were obtained with film or intensified television cameras. However, developments in charge-coupled device (CCD)

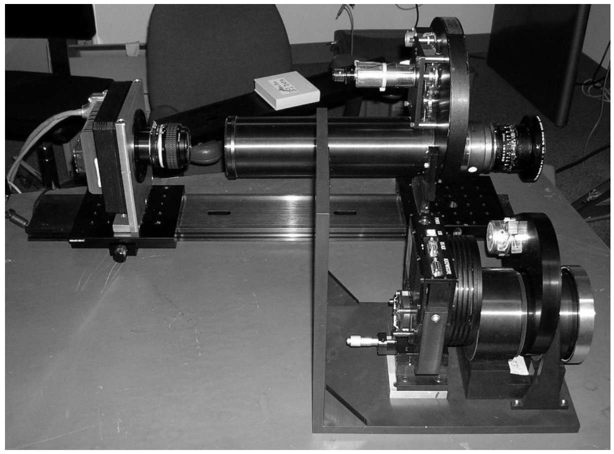

Figure 2.13: KEO architecture all-sky airglow imager fitted with a CCD camera (back). PICASSO architecture all-sky airglow imager (front).

technology over the past two decades have made it the sensor of choice for modern airglow imagers.

At least two architectures of airglow imagers are in use worldwide. Examples of each are shown together in Figure 2.13. The original is the KEO[3] architecture, which was developed using mostly off-the-shelf photographic components. While many contributions were made using the KEO architecture, these imagers are large and require considerable infrastructure to operate. A more recent imager architecture is the PICASSO (Portable Ionospheric Camera and Small-Scale Observatory). PICASSO utilizes custom optics that reduce the length of the optical train from about 1.3 m for a KEO system to 0.3 m. The PICASSO imager can be operated from a laptop in a small weatherproof enclosure of $0.5 \times 0.5 \times 0.5$ m.

Two narrow-field imagers and one all-sky imager are predominantly used in this work. The narrow-field imagers are located in Hawaii and Chile, respectively. The all-sky imager is co-located with the narrow-field imager in Hawaii.

The airglow imager ("CTIO" or "PICASSO2") used in the Chapter 4 has a narrow field of view, $80° \times 60°$, which covers about 18 degrees of magnetic longitude or 2000 km. This increases the spatial resolution of the imager compared with the all-sky systems at the expense of a more limited field of view. The imager is installed at the Cerro Tololo Inter-American Observatory (CTIO; geographic: 30.17 S, 289.19 E; geomagnetic 16.72 S, 0.42 E) near La Serena, Chile, and has been operating since August 2006. It consists of custom optics, a five-position filterwheel to select the emission line of interest, and a 2184×1472 CCD array cooled to -30 °C and binned 3×3 on-chip. The imager is oriented such that the lines of sight are parallel to the geomagnetic field at the altitude of the peak

[3]Named for KEO Consultants of Brookline, MA, now KEO Scientific, Ltd., Calgary, AB.

airglow emission, as illustrated in Figure 2.14. The physical motivation for this technique will be discussed in Chapter 3. In such an orientation, the imager can observe the effects of the polarization electric fields along an entire magnetic field line projected onto the local (off-equatorial) airglow layer.

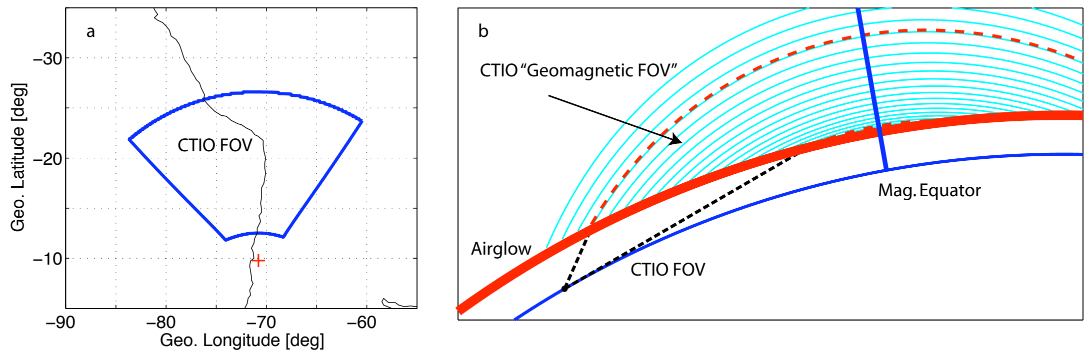

Figure 2.14: (a) Geographic view of the PICASSO narrow-field imager at Cerro Tololo, Chile (CTIO). The field of view assumes a 250-km emission altitude for the airglow. (b) This figure shows the meridional cross-section, highlighting that the lines of sight are nearly parallel to the geomagnetic field.

The narrow-field and all-sky imagers used in the Chapter 5 and 6 studies are located at the U. S. Air Force's Maui Space Surveilance Complex on Mount Haleakala on the Hawaiian island of Maui. The Cornell Narrow-Field Imager (CNFI; geographic: 20.71 N, 203.83 E; geomagnetic 21.03 N, 271.84 E) has been operational since December 2001 [*Kelley et al.*, 2002]. This system is oriented in the field-aligned viewing geometry discussed in Chapter 3. The imaging system has a narrow (47°) field of view that yields high native resolution compared to ordinary wide-field or all-sky imaging systems. CNFI has a liquid-cooled, low-noise CCD detector and a filterwheel containing several narrowband filters that allow observation of the 630.0-nm and 777.4-nm emissions, as well as a slice of the background continuum. The Cornell All-Sky Imager (CASI) is colocated with CNFI and oriented at zenith. In addition to the airglow lines observed by CNFI, it also has filters for 557.7 nm ("green" line) and 589.0 nm (sodium). The fields of view of these instruments at 250 km altitude are shown in conjunction with the beams of the Christmas Island 50-MHz radar in Figure 2.15.

2.3.4 Flat field calibration

As with any wide aperture, wide angle lens, vignetting, or intensity roll-off, occurs near the edges of the image. For certain experiments, the absolute or relative airglow intensity across an image is an important observable. Therefore, it is necessary to correct for the vignetting using a flat-field image.

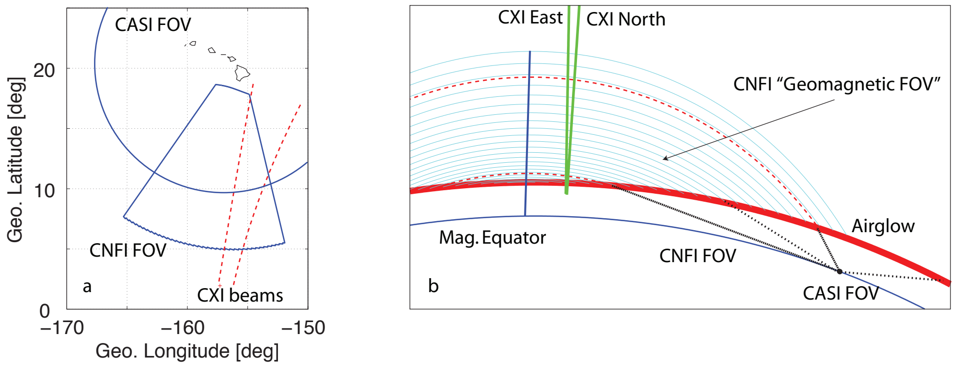

Figure 2.15: (a) Geographic view of several instruments in the central Pacific. The CASI curve is the field of view for CASI at 250 km altitude and 15° elevation. The CNFI curve is the CNFI field of view at 250 km. The dashed curves in between −150° and −155° are beams of the CXI radar mapped along the geomagnetic field into the off-equator ionosphere at 250 km. (b) Meridional-cut view of the CNFI-CASI-CXI geometry. The approximately parallel family of curves are the geomagnetic field. The CXI beams are oriented $\perp$ **B** just north of the geomagnetic equator. CNFI (oblique) and CASI (zenith) fields of view are indicated. Notice that the CNFI lines of sight are nearly parallel to the geomagnetic field.

In principle, this correction is accomplished by obtaining an image of a known constant source over the entire field of view of the imager. An integrating sphere is a convenient and accurate constant intensity source that yields a flat-field image directly. Data images are divided by the flat-field image to obtain the corrected image. Even when photometry is a secondary consideration, flat-field correction yields more visually appealing images.

In the absence of an integrating sphere, a calibrated Lambertian light source may be employed at every azimuth and elevation angle. A curve is then fit to the observed intensity as a function of angle (pixel location) in each direction. Assuming that the azimuthal variation is constant for a high-quality lens system, the flat-field image is equal to the fitted curve rotated about the optical axis:

$$\Upsilon_{FF} = a_x a_y \cos\theta_x \cos\theta_y. \tag{2.31}$$

2.3.5 Spatial calibration

Perhaps the most important calibration for all airglow imaging applications is the mapping from pixel coordinates to geographic coordinates in the airglow layer. This is a two-step procedure that begins with identifying known stars in the airglow images. Given the location for the imager, the date and time, and the locations of a few stars, an azimuth and elevation map is generated to relate the pixel locations to the azimuth and elevation [e.g., *García*, 1999]. The second step is to convert the azimuth and elevation to latitude and longitude in the airglow layer. By assuming an altitude for the centroid of the emission layer, the intersection point for each ray can be computed using spherical geometry.

The procedure outlined here is iterative. The first step is to propose a model of the imaging system and its orientation. Second, a guess is made (based on an observed star field or known surveying of the site) as to how the imager is oriented at the site. Third, the position from the on-site GPS receiver is used in conjunction with the previous two steps to create an azimuth/elevation map for each pixel in a candidate airglow image. Now, the timestamp of the airglow image is utilized with the aid of a star catalog to find the actual positions of stars within the imager's field of view. The final step is to compare the locations of the stars within the field of view from the star catalog to those stars in the candidate image. This procedure is iterated[4] until the ensemble distance between the stars in the candidate image and the catalog image is negligible.

Figure 2.16 illustrates the five parameters of the installed imager system required to establish a spatial calibration: optical axis azimuth (ξ, North-definite) and elevation (ε), CCD rotation with respect to optical axis (γ), and CCD translation ($\delta x, \delta y$) from the optical axis. Additionally, because the PICASSO-type imagers use custom non-telecentric optics, each unit has a specific function relating the angle between the optical axis and the radial distance on the CCD. This function is specified by the designer in the form of radial distances (ℓ, in pixels) at optical angles $\{0°, 15°, 30°, 45°, 60°, 75°, 80°\}$. These are fit to a cubic spline function, $\psi(\ell)$, to map each radial distance (in pixels) on the detector to its angle with the optical axis.

The center pixel offset is applied to each pixel $(i, j) \rightarrow (x_{ij}, y_{ij})$,

$$x_{ij} = i - \delta x, \tag{2.32}$$

$$y_{ij} = j - \delta y. \tag{2.33}$$

Next, the distance from each of the offset pixels (x_{ij}, y_{ij}) to the center pixel (x_0, y_0) is computed,

$$\Delta_{ij} = \sqrt{(x_{ij} - x_0)^2 + (y_{ij} - y_0)^2}, \tag{2.34}$$

where $x_0 = \lfloor \max i/2 \rfloor$, $y_0 = \lfloor \max j/2 \rfloor$. The azimuth ($\alpha_{ij}$) and elevation ($\varepsilon_{ij}$) of each pixel are

[4]There are commercial software tools which can perform this operation automatically. In the case of the PICASSO systems, it has been performed semi-automatically with a human operator in the feedback loop to assess the goodness of fit and tune the update parameters.

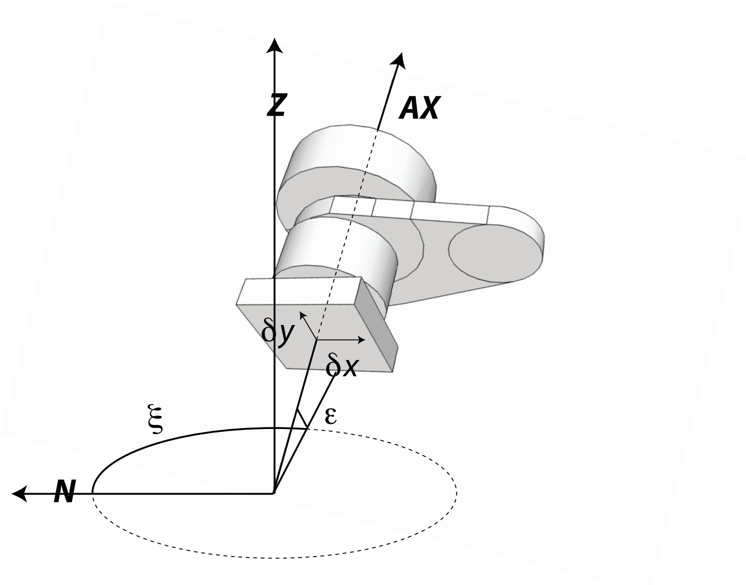

Figure 2.16: Illustration of the rotational and translational parameters for orienting an imaging system. North is indicated by N, zenith by Z, and the optical axis of the imager by AX. The optical axis is defined by the geographic location of the imager and its azimuth (ξ) and elevation (ε). The orientation of the CCD with respect to the optical axis is defined by a rotation γ and a translational offset $(\delta x, \delta y)$.

readily obtained:

$$\alpha_{ij} = \arctan \frac{y_{ij} - y_0}{x_{ij} - x_0}, \tag{2.35}$$

$$\varepsilon_{ij} = \frac{\pi}{2} - \psi(\Delta_{ij}). \tag{2.36}$$

In order to perform the orientation portion of the calibration, we treat each pixel azimuth/elevation pair as a unit vector and convert to Cartesian coordinates,

$$x_{ij} = \sin(\pi/2 - \varepsilon_{ij}) \cos \alpha_{ij}, \tag{2.37}$$

$$y_{ij} = \sin(\pi/2 - \varepsilon_{ij}) \sin \alpha_{ij}, \tag{2.38}$$

$$z_{ij} = \cos(\pi/2 - \varepsilon_{ij}). \tag{2.39}$$

Now, we use the specified (ξ, ε) orientation of the imager itself to orient the bundle of pixel unit vectors correctly. As a matter of notational simplicity, we will consider each of the unit vectors individually, although in practice this is easily vectorized. Initially, rotate about the y-axis by ε:

$$\mathbf{v}_{1,ij} = \begin{bmatrix} \cos(\pi/2-\varepsilon) & 0 & \sin(\pi/2-\varepsilon) \\ 0 & 1 & 0 \\ -\sin(\pi/2-\varepsilon) & 0 & \cos(\pi/2-\varepsilon) \end{bmatrix} \begin{bmatrix} x_{ij} \\ y_{ij} \\ z_{ij} \end{bmatrix}. \tag{2.40}$$

Now, rotate around the z-axis by ξ:

$$\mathbf{v}_{2,ij} = \begin{bmatrix} \cos\xi & \sin\xi & 0 \\ -\sin\xi & \cos\xi & 0 \\ 0 & 0 & 1 \end{bmatrix} \mathbf{v}_{1,ij}. \tag{2.41}$$

Then, rotate around the new optical axis $(u_x, u_y, u_z) = \mathbf{v}_{2,0}$ (that is, the $\mathbf{v}_2$ value corresponding to the center pixel) by γ:

$$\mathbf{v}_{3,ij} = \begin{bmatrix} 1+(1-\cos\gamma)(u_x^2-1) & (1-\cos\gamma)u_xu_y - u_z\sin\gamma & (1-\cos\gamma)u_xu_z + u_y\sin\gamma \\ (1-\cos\gamma)u_xu_y + u_z\sin\gamma & 1+(1-\cos\gamma)(u_y^2-1) & (1-\cos\gamma)u_yu_z - u_x\sin\gamma \\ (1-\cos\gamma)u_xu_z - u_y\sin\gamma & (1-\cos\gamma)u_yu_z + u_x\sin\gamma & 1+(1-\cos\gamma)(u_z^2-1) \end{bmatrix} \mathbf{v}_{2,ij}. \tag{2.42}$$

Finally, convert the Cartesian $\mathbf{v}_{3,ij} = [v_x, v_y, v_z]^T$ back to spherical coordinates:

$$E_{ij} = \frac{\pi}{2} - \arctan\left(\frac{\sqrt{v_x^2+v_y^2}}{z}\right), \tag{2.43}$$

$$A_{ij} = \frac{\pi}{2} - \arctan\left(\frac{v_y}{v_x}\right), \tag{2.44}$$

where E_{ij} and A_{ij} are elements of matrices $\mathbb{E}$ and $\mathbb{A}$, respectively. In summary, Equations (2.32)—(2.44) are encapsulated as a function that returns $\mathbb{E}$ and $\mathbb{A}$ given the CCD geometry and the five parameters that define the orientation of the system: optical axis azimuth (ξ, North-definite) and elevation (ε), CCD rotation with respect to optical axis (γ), and CCD translation ($\delta x, \delta y$) from optical axis.

The star catalog employed for this work is the Yale Catalogue of Bright Stars, hereafter referred to as BSC5 [*Hoffleit and Jaschek*, 1991]. It contains, in astronomical coordinates (right ascension, α, and declination, δ), the locations of all stars magnitude 6.5 and brighter, 9110 objects in all. The catalog is sorted by magnitude, brightest stars first, and the positions of the stars are computed for the site location and capture time of the calibration image. The conversion from astronomical coordinates to horizon coordinates is straightforward and given here using units of degrees: Compute the Julian date (JD) from the Gregorian calendar (M/D/Y, h:m:s):

$$JD = D + \left\lfloor \frac{153M+2}{5} \right\rfloor + 365Y + \left\lfloor \frac{Y}{4} \right\rfloor - \left\lfloor \frac{Y}{100} \right\rfloor + \left\lfloor \frac{Y}{400} \right\rfloor - 32045 + \frac{s + 60m + 3600(h-12)}{86400} \tag{2.45}$$

Compute the Greenwich Mean Sidereal Time from the Julian date of the observation:

$$\mathrm{GMST} = 280.46061837^\circ + 360.98564736629^\circ JD. \tag{2.46}$$

Compute the local MST for the site longitude (λ) from the GMST:

$$\mathrm{MST} \equiv (\mathrm{GMST} + \lambda) \bmod 360^\circ. \tag{2.47}$$

Compute the hour angle (H) of the object at this site and time:

$$H = \mathrm{MST} - \alpha. \tag{2.48}$$

Determine elevation (ε) and azimuth (ξ) of the object for this observation:

$$\sin\varepsilon = \sin\delta\sin\theta + \cos\delta\cos\theta\cos H \tag{2.49}$$

and

$$\cos\xi = \frac{\sin\delta - \sin\varepsilon\sin\theta}{\cos\varepsilon\cos\theta}. \tag{2.50}$$

The brightest stars with elevation angles above the local horizon (usually choose 10–15°) are retained for calibration. These points are utilized to initialize the search for the nearest stars in the star field of the calibration image. An example of this is shown in Figure 2.17. The triangles mark the estimated locations of BSC5 stars using the imager model. The circles are stars found in the vicinity of the triangles.

A distance measure such as the following is useful in establishing the end of iteration:

$$\rho = \sum_n \sqrt{({}^C\varepsilon_n - {}^O\varepsilon_n)^2 + ({}^C\xi_n - {}^O\xi_n)^2}, \tag{2.51}$$

where $({}^C\xi_n, {}^C\varepsilon_n)$ are the catalog star locations and $({}^O\xi_n, {}^O\varepsilon_n)$ are the locations of stars found in

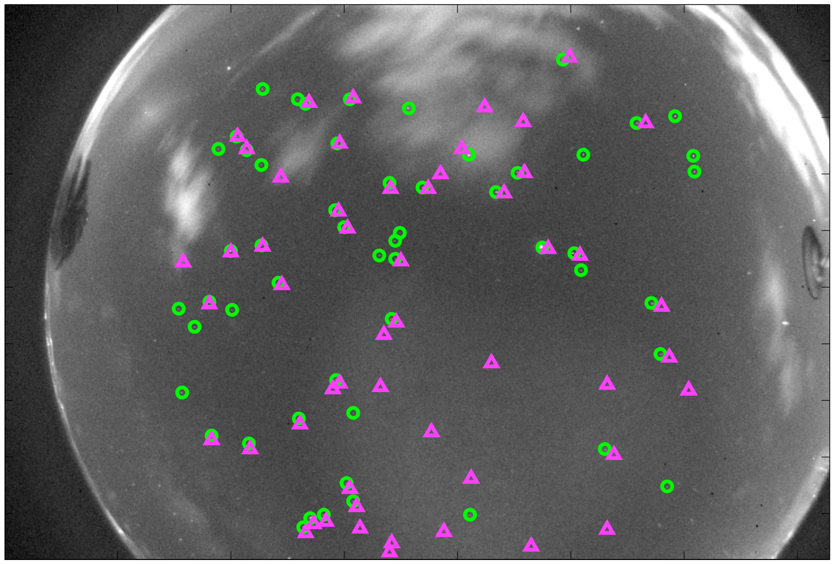

Figure 2.17: Example calibration iteration from the imaging system near Sangre Grande, Trinidad (similar to the Bonaire system discussed in Appendix B). The triangles are locations of stars from BSC5 given the proposed orientation of the imager. The circles are stars found in the image.

the image. For Figure 2.17, $\rho = 100.3$.

Once the azimuth and elevation associated with each pixel are determined, these values are mapped to arbitrary layer altitudes to match the emission centroid of the emission of interest. This computation is performed by computing the intersection of the look direction from each pixel with a spherical shell of given altitude. In order to compute the intersections, we define first a differential angle α, which measures the absolute (that is, jointly in latitude and longitude) displacement angle of the intersection from the imager location. This geometry is illustrated visually in Figure 2.18a in the two-dimensional plane containing the imager and intersection vectors, OA and OX, respectively. A little bit of manipulation yields

$$\alpha = \arccos\left[\frac{R_e \cos\epsilon}{R_e + h}\right] - \epsilon, \tag{2.52}$$

where R_e is Earth's radius, h is the layer altitude, ϵ is the elevation angle, and α is the differential angle. A given elevation ϵ angle corresponds to a unique α for all azimuths. Therefore, the latitude and longitude are separable. We consider first the latitude by defining OP as the vector through the North Pole of a spherical Earth. The procedure is illustrated by the spherical triangle in Figure 2.18b. Given the imager site colatitude (Δ_A), the pixel azimuth from the site (ξ), and the differential angle

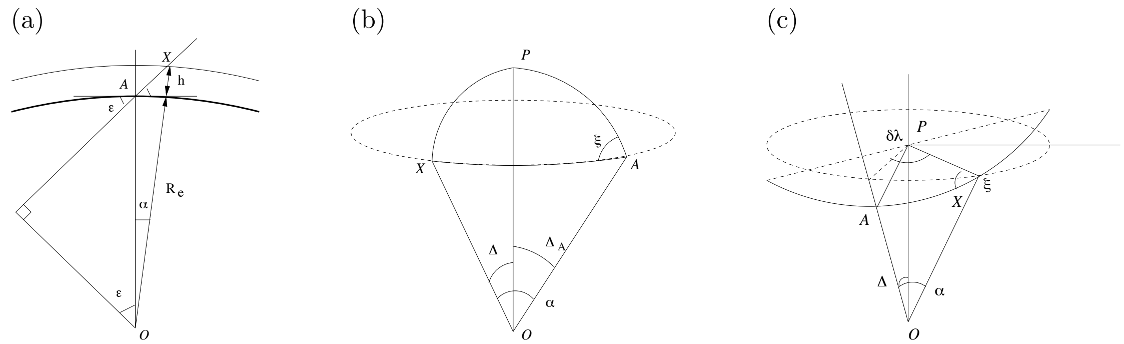

Figure 2.18: (a) Illustration of the differential angle α in the two-dimensional plane containing the intersection vector OX and the imager location vector OA. R_e is the Earth radius, h is the layer altitude, ϵ is the elevation, and α is the differential angle. (b) Derivation of the actual latitude of a pixel. XA appears to have a constant latitude only as a matter of illustrative convenience. In practice, XA may be any great circle that connects X and A. (c) Derivation of the actual longitude of a pixel. $\delta\lambda$ represents the differential longitude added to the site longitude for a given azimuth and elevation (via differential angle α).

(α), we can compute the colatitude of the pixel (Δ) by

$$\cos\Delta = \cos\alpha\cos\Delta_A + \sin\alpha\sin\Delta_A\cos\xi. \tag{2.53}$$

By converting from colatitude ($\cos\Delta$) to latitude ($\sin\delta$), we can rewrite this as

$$\delta = \arcsin\left(\cos\alpha\cos\delta_A + \sin\alpha\sin\delta_A\cos\xi\right). \tag{2.54}$$

The final computation is for the longitude. In a spherical triangle, the law of sines represents the relationships between the angles with vertices at the origin O ($\{a, b, c\}$, not illustrated) and the corresponding vertex angles on the surface of the sphere ($\{A, B, C\}$),

$$\frac{\sin A}{\sin a} = \frac{\sin B}{\sin b} = \frac{\sin C}{\sin c}. \tag{2.55}$$

Considering Figure 2.18c, we can write the law of sines for this figure as

$$\sin\delta\lambda = \frac{\sin\xi\sin\alpha}{\sin\Delta} = \frac{\sin\xi\sin\alpha}{\cos\delta}. \tag{2.56}$$

To obtain the actual longitude, we add $\delta\lambda$ to the site longitude,

$$\lambda = \arcsin\left(\frac{\sin\xi\sin\alpha}{\cos\delta}\right) + \lambda_{\text{site}}. \tag{2.57}$$

This mapping from pixel coordinates to geographic coordinates permits the interpretation of airglow images as maps of ionospheric irregularities. Figure 2.19 illustrates one such map. A detailed interpretation of this map will be offered in Chapter 3.

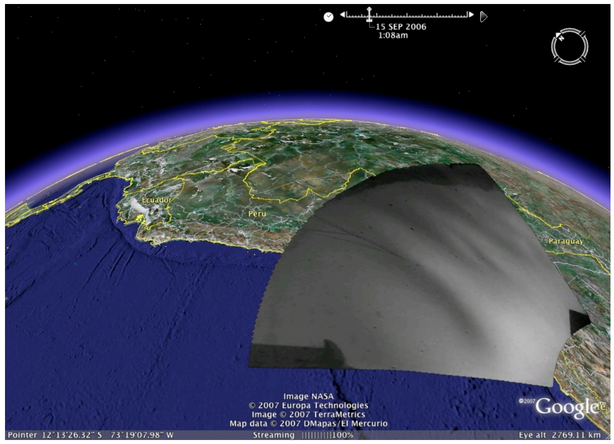

Figure 2.19: Airglow image from Cerro Tololo, Chile, from 15 September 2006 mapped to geographic coordinates at 250-km altitude. Note the dark irregularity bands stretching approximately from north to south.

2.3.6 Post-processing

Some post-processing can clarify the features of airglow images. Both destructive and non-destructive processing may be performed. That is, some techniques improve clarity at the expense of voiding the photometric interpretation of the intensity data, for example, adaptive histogram equalization. Most effort, however, is directed toward reducing noise in the images. For the purpose of this discussion, there are three sources of noise: dark current in the CCD, read-out noise in the CCD, and stars.

Figure 2.20 illustrates a typical approach to denoising airglow images, with each step providing slightly better SNR than the previous one. This example is of the 630.0-nm emission from a narrow-field airglow imager at the Cerro Tololo Inter-American Observatory (CTIO) near La Serena, Chile, at 0336 UT on 16 (259) September 2006 [*Makela and Miller*, 2008]. Figure 2.20a is the raw image from the CCD, with only the contrast adjusted. The first step is to remove the dark noise (and readout noise) by taking a dark image (Figure 2.20b) with the same exposure length as the observed image. The difference (Figure 2.20c) between the observed image and the dark image gains about 10.1 dB SNR over the original.

The stars (and hot pixels not removed by the dark subtraction) may be removed by locating the brightest points in the image and selectively applying a median filter to the surrounding region [e.g., *Lim*, 1990]. As shown in Figure 2.20d, this gains an additional 3.4 dB of SNR over the image with the dark noise subtracted. Perhaps the biggest remaining gain in SNR may be obtained by applying a wavelet filter (Figure 2.20e). The wavelet used for this filtering is a Daubechies type 3 wavelet applied using the MATLAB software package [*Daubechies*, 1992]. The Daubechies denoising filter improves the SNR another 5.8 dB to 19.2 dB over the original. This is quite good considering the nominal amount of effort required for these denoising steps.

Clearly, the image in Figure 2.20f has undergone contrast distortion and the pixel intensities are no longer photometrically meaningful. However, this adaptive histogram equalization step brings out details that are not evident in the unequalized images, notably the depletion to the right of the packet of depletions in the center of the image. While in Figure 2.20e the depletion just appears to be a dark patch in the airglow, the bifurcations are clearly evident in the equalized image.

Alternatively, a sequence of airglow images may be processed jointly to produce even better denoising results [*Atkinson et al.*, 2006]. An example of an image processed using this technique is presented in Figure 2.21. The small-area SNR estimation shows only a 0.7 dB increase in SNR over the sequence described in the previous paragraphs. However, a visual inspection of Figures 2.20e and 2.21 suggests that the technique of *Atkinson et al.* [2006] indeed produces more visually appealing images with particularly fewer dark pixels.

2.3.7 Keogram representation

In order to aggregate an entire night of airglow data into a printable (as opposed to a sequence of frames) format, the so-called "keogram" was developed. A keogram is constructed by taking strips from the same location in each image. The strips are assembled into a time series, as shown in Figure 2.22.

In the example of Figure 2.22, the cut was made along constant geomagnetic meridian (88° W magnetic longitude) with magnetic latitude as the spatial variable. The coherent dark curved structures particularly evident between 7–11 UT are equatorial plasma depletions. The slope of the depleted regions is indicative of their velocity and shape in much the same manner as the slit-camera model for radar backscatter. The lighter, less-coherent objects in the image are clouds.

In Chapter 4, we will see a distorted keogram whose spatial variable is the tangent point altitude of a radio occultation ray path. By plotting the received SNR on the radio link along side this plot, the altitude of scintillation-causing irregularities may be read directly off the plot. Finally, in Chapter 5, we will see a keogram with a the geomagnetic field line apex as the spatial variable. This

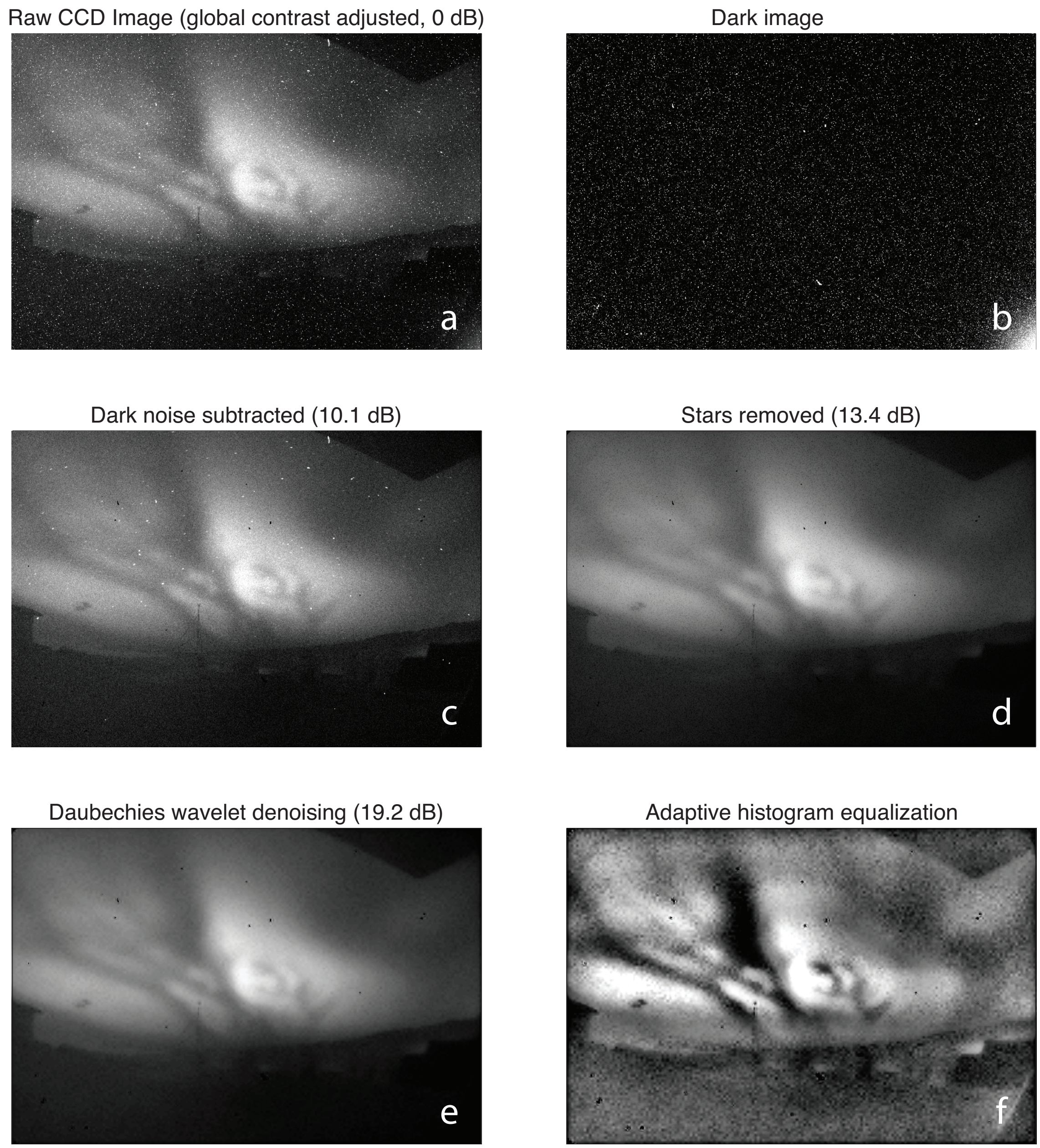

Figure 2.20: Airglow images from Cerro Tololo, Chile, from 16 September 2006 in CCD pixel coordinates showing (a) no denoising, (b) dark frame, (c) subtraction of dark frame, (d) star removal, (e) Daubechies wavelet denosing, and (f) histogram equalization. Each image processing step (c)–(f) is performed on the results of the previous step.

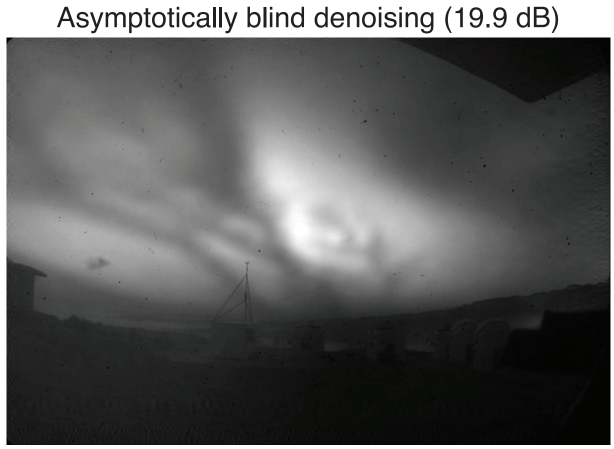

Figure 2.21: Airglow image from Cerro Tololo, Chile, from 15 September 2006 in CCD pixel coordinates. This image has had the dark noise removed and has been processed with the denoising algorithm presented by *Atkinson et al.* [2006].

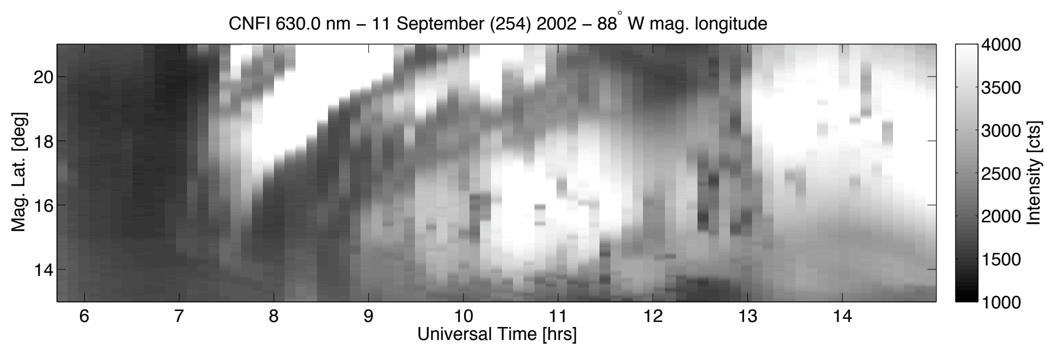

Figure 2.22: Example keogram of 630.0-nm airglow data collected at Haleakala, Hawaii, on 11 September 2002.

allows radar backscatter to be compared with the airglow.

2.4 Conclusion

In this chapter, we have reviewed several radio and optical remote sensing techniques for the ionosphere. VHF radar backscatter is capable of detecting coherent echoes from Bragg-scale plasma irregularities, as well as providing estimates of plasma temperature and density via incoherent echoes from ensembles of free electrons in the plasma. Although this work leverages theories and models developed using incoherent backscatter data, we will be primarily interested in coherent backscatter from F-region irregularities near the geomagnetic equator. The excellent frequency stability and good geographic coverage combined with inexpensive commercial receivers have made forward-scatter ionospheric observations using the Global Positioning System practical. These observations are either dispersive multi-carrier observations of the ionospheric plasma density or signal power and phase observations to detect diffraction from 100-meter scale irregularities. One innovative use of GPS receivers is radio occultation, which involves placing them in low-Earth orbit (LEO) to gather plasma (and neutral) density profiles from regions that are ordinarily sparsely probed. This technique may also be useful for imaging or locating diffraction-causing irregularities.

Images of airglow emissions provide snapshots of a large (100s or 1000 km) geographic region of the ionosphere with relatively high spatial (1–10 km) and temporal (1–2 min) resolution. Several emission lines are useful for observing F-region irregularities, although most of the work in this dissertation is focused on the 630.0-nm emission. Imaging systems are calibrated using the star field to determine the extent of the ionosphere observed within their field of view. As with any low-light photometry process, noise is an important consideration. Several steps were outlined, including subtracting a dark frame and wavelet filtering, to improve the signal-to-noise ratio by almost 20 dB.

The next chapter describes how the geomagnetic-field-aligned nature of irregularities may be exploited to infer the three-dimensional extent of plasma density structures from two-dimensional airglow images. This assumption also links data from radio observations and optical airglow imaging in a common geomagnetic coordinate system. The remaining chapters discuss applications to ionospheric problems.

CHAPTER 3

ELECTRIC FIELD MAPPING AND THE FIELD-ALIGNED AIRGLOW IMAGING TECHNIQUE

3.1 Introduction

Observation of the equatorial ionospheric irregularities discussed in Chapter 1 using the airglow techniques of Chapter 2 depends on the "impression" of electric fields associated with the irregularities on the airglow emission layer. Due to the high anisotropy of the ionospheric conductivity tensor, particularly in the F region, electric fields map efficiently along the geomagnetic field. However, at small scales and lower altitudes, the Pedersen and Hall conductivity terms begin to play an important role. The field-aligned nature of the irregularities suggests a special imaging geometry which is optimal for observing longitudinal structures. This chapter explores the efficiency of mapping electric field structures of different scales from the geomagnetic equator into the off-equator regions where depletions are observed in the airglow as well as the field-aligned imaging geometry and the geomagnetic interpretation of airglow images.

3.2 Electric Field Mapping

Fundamentally, the mapping of electric fields is a classic problem first tackled rigorously by *Farley* [1959]. The present chapter contains a review of Farley's work utilizing modern computer solution techniques and ionosphere models. The results are compared and discussed. The technique is extended to two cases of interest to this work. The first is the simpler case in which irregularities are generated in the local (mid-latitude) ionosphere and mapped to the geomagnetic equator as suggested by the observations presented in *Makela et al.* [2009]. A similar case was considered by *Saito et al.* [1995]. The second case is more complicated and more relevant to this work in general: mapping of electric fields from the geomagnetic equator over the entire airglow imager field of view. This suggests the "sweet spots" for observing fine structure.

3.2.1 Physical derivation

In a companion set of two papers, *Farley* [1959, 1960] derived relationships for the impact of electric fields of different scales acting at different heights in the ionosphere. He was interested in the effects of electric fields generated in the E region on the F region. In the first paper, he developed the "polar case" illustrated in Figure 3.1a to determine the attenuation of the potential field $\phi(x, y, z)$ in the plane perpendicular to the geomagnetic field, $\mathbf{B}$, with altitude. In the second paper, he developed the "middle latitude case" illustrated in Figure 3.1b by keeping the potential field parallel to the Earth's surface and projecting it along the magnetic field. An approximate "equatorial case," illustrated in Figure 3.1c, was also developed in the second paper under the assumption that the small-angle approximation for the tangent is valid for the dip angle and that Earth's magnetic field may be approximated by the dipole term of the multi-pole expansion. In each of the "polar" and "middle

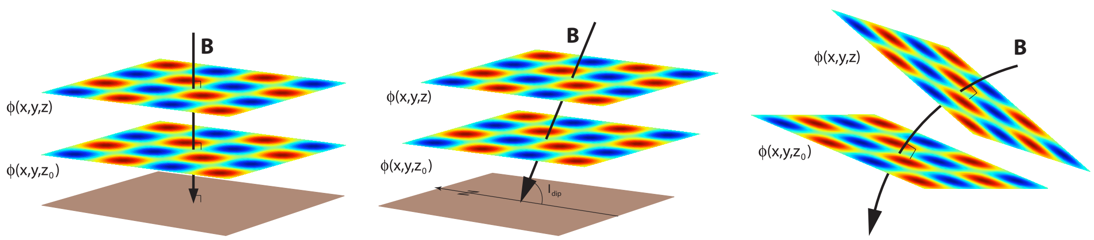

(a) (b) (c)

Figure 3.1: The (a) polar, (b) middle latitude, and (c) equatorial geometries.

latitude" cases, the geomagnetic field line is assumed to be approximately linear over the region of interest. Due to the scarce computing resources available at the time, analytical solutions were favored. In the present analysis, computational resources are no longer a primary concern and a technique similar to that employed in the polar case is utilized over many small, discrete regions, to perform the mapping between any two arbitrary points on the same field line.

In a coordinate system with $\hat{\mathbf{a}}_z$ parallel to $\mathbf{B}$ and $\hat{\mathbf{a}}_x$ perpendicular to $\mathbf{B}$ in the plane of $\mathbf{B}$, the ionospheric conductivity tensor is defined as

$$\bar{\bar{\sigma}} = \begin{pmatrix} \sigma_P & -\sigma_H & 0 \\ \sigma_H & \sigma_P & 0 \\ 0 & 0 & \sigma_0 \end{pmatrix}, \tag{3.1}$$

where σ_0 is the specific conductivity along $\mathbf{B}$, σ_P is the Pedersen conductivity perpendicular to $\mathbf{B}$ in the plane swept out by $\mathbf{B}$, and σ_H is the Hall conductivity perpendicular to both $\mathbf{B}$ and the plane swept out by $\mathbf{B}$. In the absence of a neutral wind, the current due to an applied electric field $\mathbf{E}$ can be computed from the electromagnetic form of Ohm's law, neglecting wind-driven currents:

$$\mathbf{J} = \bar{\bar{\sigma}} \cdot \mathbf{E}. \tag{3.2}$$

Next, we exploit the fact that the electric field can be written as the gradient of a potential distribution, $\mathbf{E} = -\nabla\phi$. Furthermore, over a short time scale, the current $\mathbf{J}$ is constrained to be divergence-free,

$$\nabla \cdot \mathbf{J} = -\nabla \cdot (\bar{\bar{\sigma}} \cdot \nabla\phi) = 0. \tag{3.3}$$

The expanded divergence of the product evaluates to

$$\frac{\partial^2\phi}{\partial x^2} + \frac{\partial^2\phi}{\partial y^2} + \frac{1}{\sigma_P}\frac{\partial}{\partial z}\left(\sigma_0\frac{\partial\phi}{\partial z}\right) = 0. \tag{3.4}$$

3.2.2 Solution

We now introduce a coordinate transformation

$$\begin{aligned} x' &= x \\ y' &= y \\ dz' &= \sqrt{\tfrac{\sigma_P}{\sigma_0}}dz \end{aligned} \quad . \tag{3.5}$$

Note that because z' is defined in terms of differentials, it must be referenced to a certain height. In *Farley* [1959], $z' = 0$ at $z = 300$ km, which corresponds to the observation height. After some algebra and recognizing that $\partial/\partial n(\ln u(n)) = (1/u(n))\partial u(n)/\partial n$, we can let ∇'^2 be the Laplacian in the new coordinate system and rewrite Equation (3.4) as

$$\nabla'^2\phi + \frac{\partial}{\partial z'}\ln\left(\sqrt{\sigma_0\sigma_P}\right)\frac{\partial\phi}{\partial z'} = 0. \tag{3.6}$$

In the interest of finding a tidy solution, we introduce the geometric mean conductivity

$$\sigma_m = \sqrt{\sigma_0\sigma_P} \approx Ce^{c_0 z'}, \tag{3.7}$$

yielding the analytical form

$$\nabla'^2\phi + c_0\frac{\partial\phi}{\partial z'} = 0. \tag{3.8}$$

If we consider the boundary condition that the potentials with source at z'_0 decay to zero as $z' \to \infty$, we recognize that potentials will have solutions of the form

$$\phi = \phi_0 \exp\left(j\left(k_x x' + k_y y'\right)\right) \exp\left(-\gamma\left(z' - z'_0\right)\right). \tag{3.9}$$

The decay and growth parameters α and β are the solutions to the characteristic polynomial in γ, letting $k^2 = k_x^2 + k_y^2$ and solving Equation (3.7) for c_0:

$$\begin{array}{c} \alpha = \frac{\sqrt{c_0^2+4k^2}+c_0}{2} \\ \\ \beta = \frac{\sqrt{c_0^2+4k^2}-c_0}{2} \end{array}. \tag{3.10}$$

Farley [1959] divided the ionosphere into three discrete regions by height, setting the source field at z'_0 and observing the mapped field at $z' = 0$. We extend Farley's solution to an ionosphere with N regions, allowing us to consider more general problems. We assume that each region has a solution of the form

$$\phi_i = \Phi(x', y')\left[G_i \exp(-\alpha_i(z' - z'_{i-1})) + H_i \exp(\beta_i(z' - z'_{i-1}))\right]. \tag{3.11}$$

At the source, where $z' = z'_0$, the following boundary condition exists:

$$\phi_1 = \Phi(x', y'). \tag{3.12}$$

At the other region interfaces, we assume continuity of ϕ and $\partial\phi/\partial z'$. Recalling that the potential decays to zero as $z' \to \infty$, the growing solution should be suppressed at the observation point. Therefore, the final H_i is constrained to be zero and is not solved. For N regions, this yields a system of $2N - 1$ equations and unknowns, which can be represented in matrix form as

$$\mathbf{i} = \mathbb{A}\mathbf{x}, \tag{3.13}$$

where $\mathbf{i}$ is a $(2N-1)\times 1$ column vector with one in the first position and zeros elsewhere, representing the boundary condition at the source. The $\mathbf{x}$ column vector contains the G_i's and H_i's. The matrix $\mathbb{A}$ is a $(2N - 1) \times (2N - 1)$ sparse matrix encoded with the interfacial boundary conditions. We are really only interested in $G = G_N$, which corresponds to the decaying solution in the last region.

There is no H_N, per the decaying boundary condition. The attenuation factor (A) is obtained as

$$A = G_N \exp\left(-\alpha_{2N-1}(z'_N - z'_{N-1})\right). \tag{3.14}$$

Note now that given a well-characterized ionosphere or model ionosphere, we have a solution method not only for the polar case, but for any field-aligned trajectory over which the variation in the conductivities is dominated by the position along the field line. This interpretation is fundamentally similar to that of *Saito et al.* [1995], although employing a slightly different form written in the terms of *Farley* [1959].

3.2.3 Model ionosphere

For the purpose of modeling the conductivity tensor at an arbitrary point (both spatial and temporal) in the ionosphere, it is helpful to begin with an empirical model of the plasma and neutral constituents plus the Earth's magnetic field. The International Reference Ionosphere (IRI2007) [*Bilitza*, 2001; *Bilitza and Reinisch*, 2008], the NRLMSIS00E [*Picone et al.*, 2002], and the International Geomagnetic Reference Field (IGRF) [*Maus et al.*, 2005] are employed to provide plasma ion and electron densities, neutral densities, and magnetic field intensities, respectively, as a function of position and time.

The electron-ion and electron-neutral collision frequencies are computed using the Chapman formulas in *Farley* [1959] and *Kelley* [1989]. T_e is the electron temperature in K; n_e and n_n are the electron and neutral densities in cm^{-3}, respectively:

$$\nu_{ei} = \left(34 + 4.18\log_{10}\left(\frac{T_e^3}{n_e}\right)\right) \times n_e T_e^{-3/2} \tag{3.15}$$

$$\nu_{en} = \left(5.4 \times 10^{-10}\right) n_n \sqrt{T_e} \tag{3.16}$$

$$\nu_e = \nu_{ei} + \nu_{en}. \tag{3.17}$$

The ion-neutral collision frequency is computed following *Makela and Kelley* [2003b]:

$$\nu_{in} = \left(0.393\sqrt{\frac{T_n + T_i}{2}}[O] + 6.9[N_2] + 6.7[O_2]\right) \times 10^{-10}. \tag{3.18}$$

Finally, the specific conductivity, parallel to the geomagnetic field, is computed using Chapman's formula

$$\sigma_0 = n_e q_e^2 \left(\frac{1}{m_e \nu_e} + \frac{1}{m_i \nu_{in}} \right). \tag{3.19}$$

The Pedersen conductivity (S/m) perpendicular to **B** is also computed from the Chapman formulas:

$$\sigma_P = n_e q_e^2 \left(\frac{\nu_{in}}{m_i \left(\Omega_i^2 + \nu_{in}^2\right)} + \frac{\nu_e}{m_e \left(\Omega_e^2 + \nu_e^2\right)} \right). \tag{3.20}$$

The electron and ion gyro frequencies (Ω_e and Ω_i, respectively), are derived from the Lorenz force law and Newton's second law [e.g., *Heelis*, 2004]. The fundamental unit of electronic charge is $q_e = 1.602 \times 10^{-19}$ C.

3.2.4 Results

Polar case

To perform a first-order evaluation of the method outlined above, we reproduce the result of *Farley* [1959]. Using the empirical model described in the previous section, a vertical rocket trajectory is simulated from Fort Churchill, Manitoba, at noon local time under solar maximum conditions. Figure 3.2 illustrates the result for wavenumbers $k = \{0.1, 0.25, 0.5, 1.0, 2.0, 4.0, 8.0\}$, where $\lambda = 2\pi/k$. As expected, small scale sizes (large wavenumbers) are attenuated more aggressively than larger scales. Attenuation is lower for all scales when the source is located at a higher altitude. The ionosphere model used by Farley differs slightly from that used in this analysis. However, the salient features are visible in both plots.

Transequatorial case

For the transequatorial case, a geomagnetic field line approximately linking sites at Cerro Tololo, Chile (geo 30.17° S, 289.19° E; mag 16.72° S, 0.42° E), and Villa de Leyva, Colombia (geo 5.57° N, 287.37° E, mag 17.79° N, 0.13° W), is modeled using the suite of models discussed above. The conditions are early evening (2000 LT) in September during high solar activity and quiet geomagnetic field. Figure 3.3a illustrates the effect of mapping different scale sizes from a variety of source heights (E-region all the way to apex at the equator) in the southern hemisphere to 250 km (approximately the layer height for the 630.0-nm airglow emission) in the northern hemisphere. Large scales are well-preserved, while smaller scales are not. For all scale sizes, the attenuation decreases for sources at higher altitudes near the equator. The adjacent Figure 3.3b shows the trajectory of the field line and the background plasma density.

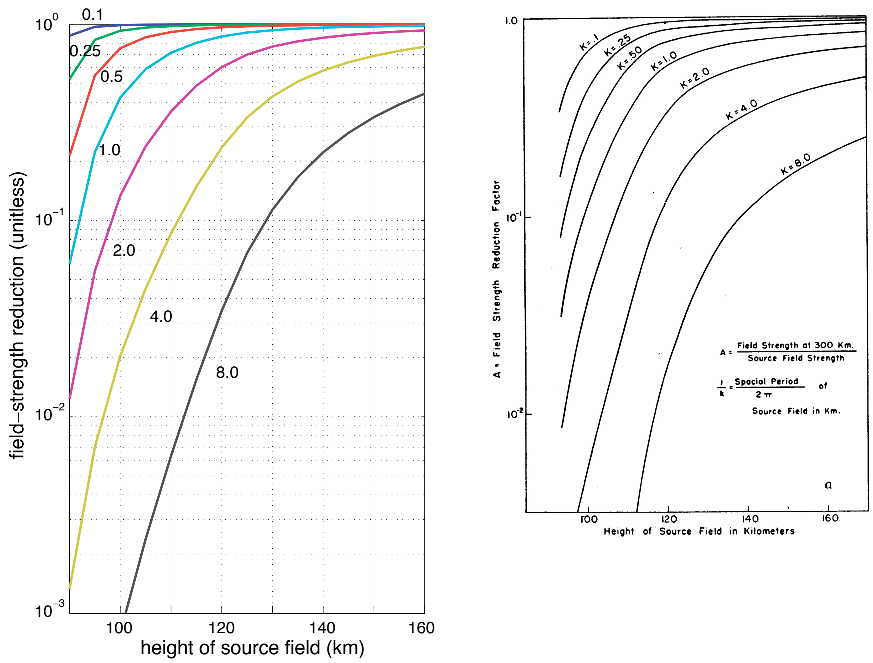

(a) (b)

Figure 3.2: (a) Reduction of field strength reduction at 300 km for different wavenumbers. (b) Original result of *Farley*, 1959. (Reproduced with permission of the American Geophysical Union.)

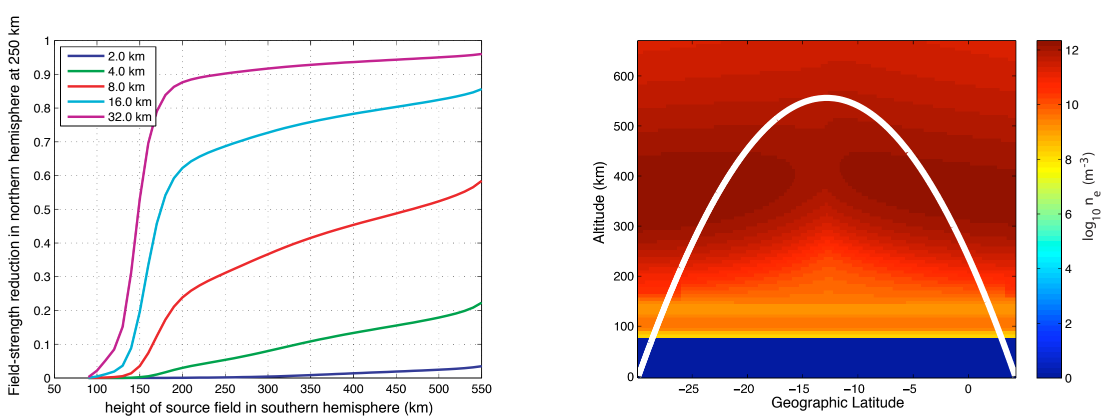

(a) (b)

Figure 3.3: (a) Relative strength at 250 km in the Northern hemisphere for field sources of different scale sizes at different heights in the Southern hemisphere. (b) Geometry of the field line with $\log_{10} n_e$ in the background (units of m^{-3}).

Airglow imaging case

This case is for the Cornell Narrow-Field Imager system located atop Mt. Haleakala (CNFI; geographic: 20.71° N, 203.83° E; geomagnetic 21.03° N, 271.84° E) on the Hawaiian island of Maui. This system was installed particularly for the purpose of studying field-mapped irregularities such as the ones described in this chapter. The ionosphere was modeled for a day in September 2005 with relatively quiet geomagnetic conditions.

Figure 3.4 illustrates, over CNFI's entire geographic field of view, the efficiency of mapping electric fields at the geomagnetic equator to the local ionosphere, similar to Figure 3.3a. At 8 km scales, the crest region of the equatorial anomaly permits the strongest response in the airglow layer. This is frequently observable in practice, particularly with very high resolution imagers. Nothing else is particularly noteworthy about this in light of the previous results, except perhaps that it explains the difficulty in observing the bottom-type layers described by *Hysell and Burcham* [1998] with airglow imagers.

3.2.5 Discussion

One of the drawbacks to the Farley model and similar models is that current continuity is enforced at the source and response points under the assumption that no current flows in the regions beyond these points, as illustrated in Figure 3.5. This model is conceptual only and does not completely consider that Equation (3.8) is not reversible. That is, in the model and the actual ionosphere, exchanging the positions of the source and observation points may not yield exactly the same attenuation for the same-size structure.

Unfortunately, there are several interesting special cases in the growth of equatorial plasma depletions that are ignored under this assumption. The most notable cases are when the E region at one or both ends of the flux tube (magnetic field line) is highly conductive. This could occur because the E region is still in sunlight or due to the presence of a sporadic-E layer. This situation might effectively be approximated by adding an additional equivalent Pedersen conductivity term representing the rest of the flux tube at each end point. In both of these circumstances, we expect the field to disappear completely by driving currents perpendicular to $\mathbf{B}$.

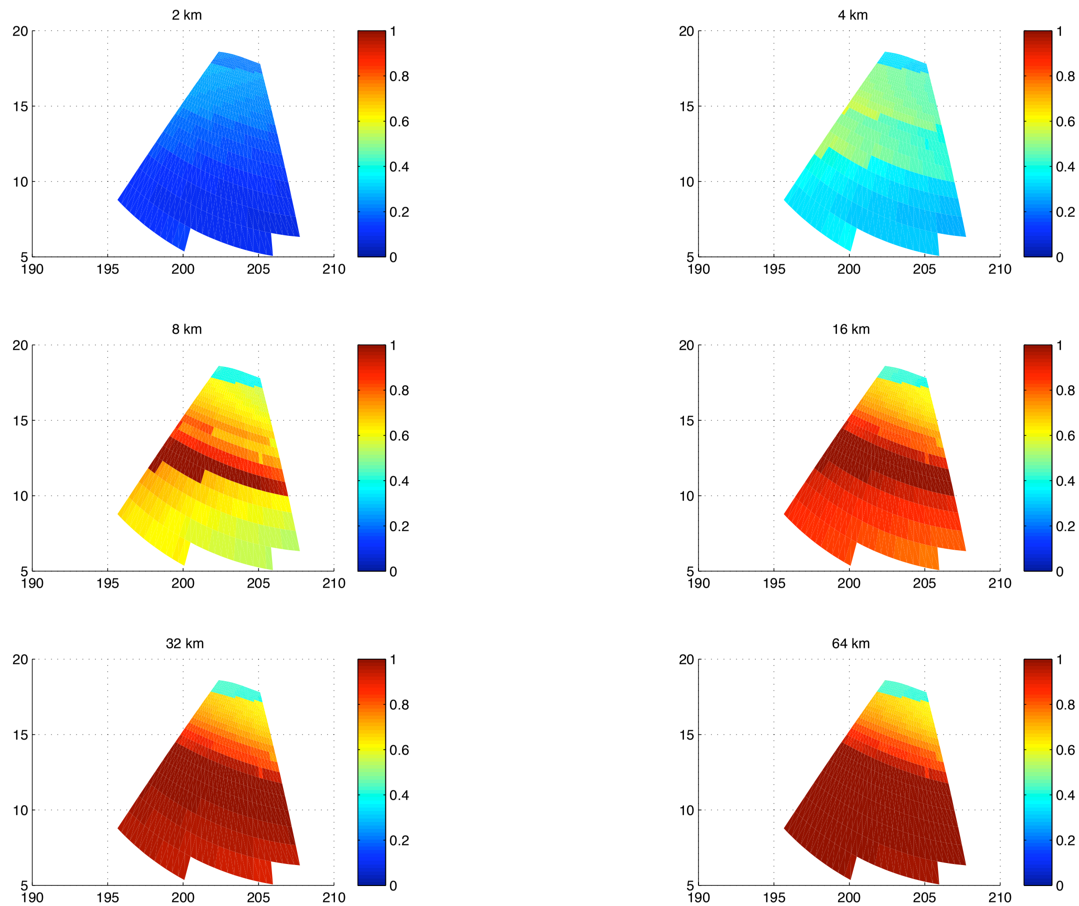

Figure 3.4: Electric field strength mapped from geomagnetic equator (apex) to nominal 630.0-nm airglow emission altitude (250 km) in the CNFI field of view for field structure scales of {2,4,8,16,32,64} km.

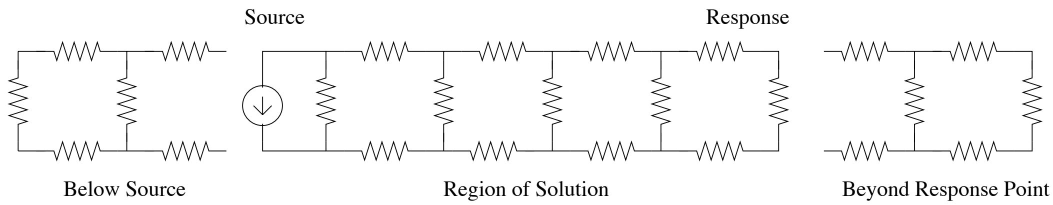

Figure 3.5: Circuit model of two magnetic field lines showing the specific (series) and Pedersen (shunt) conductivities. This model is inaccurate in the sense that the flux tube might be better modeled with dependent sources mixed among the resistors to represent other current sources. The $c_0 \partial\phi/\partial z'$ term in Equation (3.8) belies this condition. This model is conceptual only and does not accurately model all aspects of the ionosphere circuit. See text.

3.3 Interpretation of Airglow Images

3.3.1 Equatorial plasma depletions

Once an airglow image of one or more equatorial plasma depletions has been mapped into geographic coordinates, it can be interpreted physically in the following way. As discussed in the previous section, large-scale polarization electric fields associated with the depletion map efficiently along the geomagnetic field. Due to these mapped polarization fields, the depletion expands into its characteristic wedge shape. Where this wedge punctures the airglow layer, it is observable in airglow images. It is important to recall that even when the airglow emission diminishes, the depletion may still be present, although not visible. This is particularly true of the 630.0-nm emission.

Since the depletion in the airglow is the result of electric fields that map along the geomagnetic field, the airglow image may also be mapped along the geomagnetic field to the apexes of the field line [*Mendillo and Tyler*, 1983]. For sufficiently large scales, this concept may be generalized to any point along the field line [e.g., *Otsuka et al.*, 2002]. Figure 3.6a shows an airglow image projected onto a spheroidal shell at 250 km altitude in geographic coordinates. Figure 3.6b is a three-dimensional map of the depleted wedges extruded from the airglow image.

One convenient representation of the field-aligned nature of equatorial plasma depletions is to convert the latitude and longitude of the pixels in an airglow image to a "geomagnetic" coordinate system. One example of a geomagnetic coordinate system is AACGM, the Altitude-Adjusted Corrected GeoMagnetic coordinate system [*Baker and Wing*, 1989]. In a geomagnetic coordinate system, the latitude, longitude, and altitude define a geomagnetic field line rather than a point in a grid mapped onto a surface. The geomagnetic equator is defined as the apex point of each field line. This representation allows images to be mapped from the airglow layer to the geomagnetic equator, where the images may be directly compared with radar backscatter maps. AACGM has

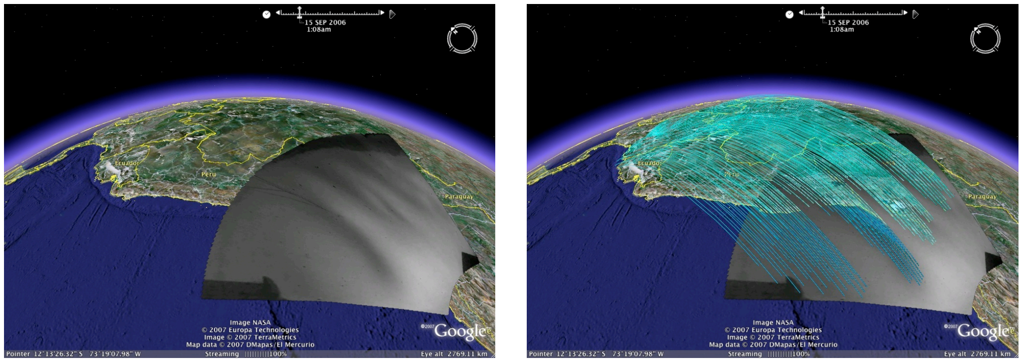

(a) (b)

Figure 3.6: (a) A field-aligned 630.0-nm airglow image from Cerro Tololo, Chile, projected onto the assumed emission layer at 250 km. (b) The same image as (a) with the airglow depletions extruded along the geomagnetic field to produce a three-dimensional map of the irregularities.

the advantage that it is quite fast in converting between geographic and geomagnetic coordinates, something that is vital when processing a large quantity of data. However, it was developed for use at high latitudes and is not presently maintained. Whenever possible, it is better to use IGRF, the International Geomagnetic Reference Field [*Maus et al.*, 2005]. A discussion of IGRF versus AACGM and field tracing steps in IGRF is presented in Appendix C.

3.4 Field-Aligned Imaging Geometry

A traditional airglow imaging system utilizes a zenith-pointing camera with a wide field of view. This type of system offers a view of nearly the entire sky. One of the major drawbacks to this imaging technique is that, for field-aligned density depletions, the ray (integration) paths for each pixel tend to cross magnetic field lines in the airglow layer rather than nearly parallel to them. This leads to spatial blurring as the rays cross both dense and depleted regions. Since depletions are field-aligned, an airglow imager with ray paths that are parallel to the geomagnetic field in the airglow layer gives the optimal viewing geometry [*Tinsley*, 1982]. This configuration is depicted in Figure 3.7. Several months' data were collected from Hawaii in the late 1980s using the field-aligned imaging geometry [*Rohrbaugh et al.*, 1989]. A more comprehensive data set has come from the CNFI and CASI systems operating at Haleakala, Hawaii, since 2001 [*Kelley et al.*, 2002]. The details of these instruments were discussed in Chapter 2.

No imager has been created that can have all of its rays parallel to the geomagnetic field. Therefore, some parts of the image will be subject to more or less spatial blurring than others.[1] The

[1]In principle, this relates to the field-aligned irregularity assumption discussed in §2.2.4 and *Sokolovskiy et al.*

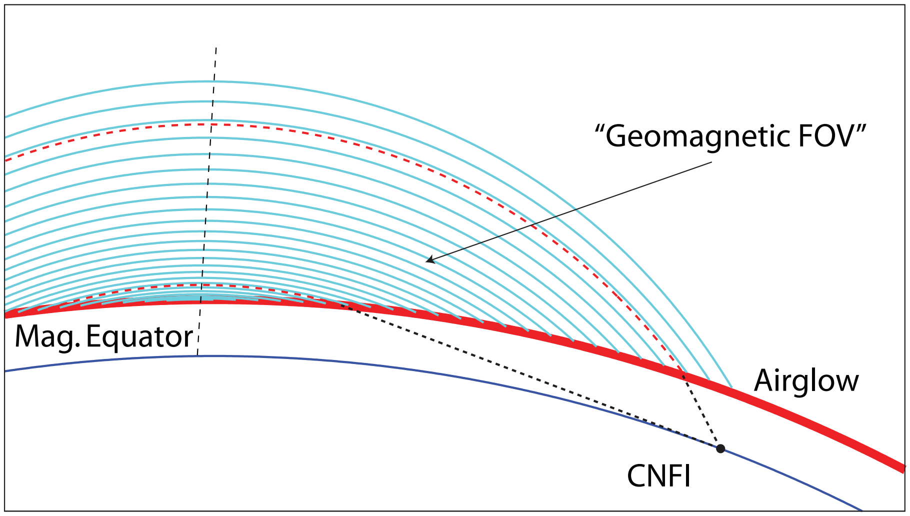

Figure 3.7: Field-aligned imaging geometry from Haleakala, Maui, Hawaii.

amount of spatial blurring has been quantified as the minimum-scale resolvable feature and can be computed through geometry [*Tinsley*, 1982]. Figure 3.8 is an example of the spatial blur across the field-of-view of the imager operating at Cerro Tololo, Chile [*Makela and Miller*, 2008]. In practice, it is best to interpret the contours as a relative measure of the blurring rather than a strict scale limit.

Figure 3.9 is an illustration of the same spatial blurring estimation performed on the CNFI system in Hawaii. This is particularly interesting to compare with Figure 3.4. It is clear that there is a "sweet spot" near 12° N, 202° W. Although this spot does not approach the native imager resolution (about 3 km with 2×2 binning) in that part of the image, it does suggest that field-aligned features below 10 km can be identified there.

Comparing Figures 3.8 and 3.9 illustrates something that has been observed in practice. In the case of the PICASSO2 system at Cerro Tololo, depletions are rarely observed in the western 25% of the image, approximately west of the 283° meridian. Rather, they slide into view fully formed near this point. This behavior is less common at Haleakala, where the CNFI system has a narrower field of view. This suggests that PICASSO's field of view might be a little too wide for its location, resulting in wasted CCD space. On the other hand, the wider field of view permits spacing between multiple packets of depletions to be estimated [*Makela and Miller*, 2008].

[2002].

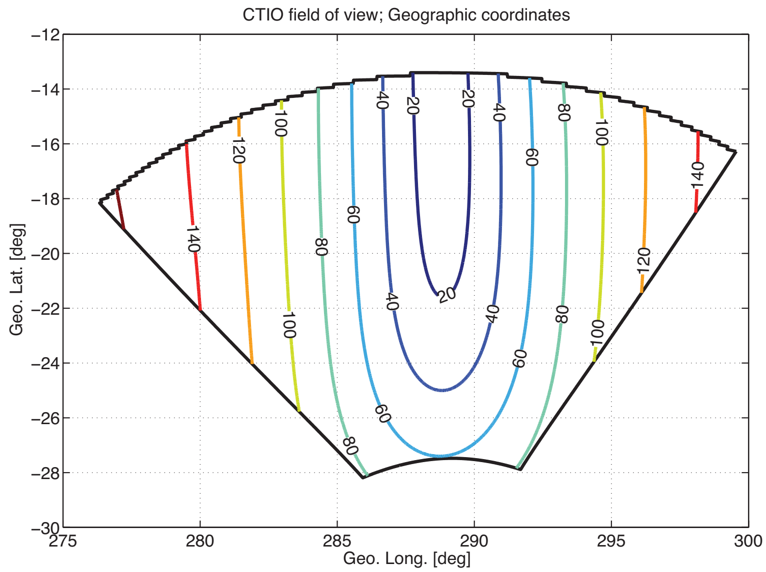

Figure 3.8: Relative spatial blurring across the field-of-view of the PICASSO2 narrow-field imager operating at Cerro Tololo, Chile. In theory, the contours refer to the smallest resolvable feature dimension. In practice, it is best to interpret them as a relative measure.

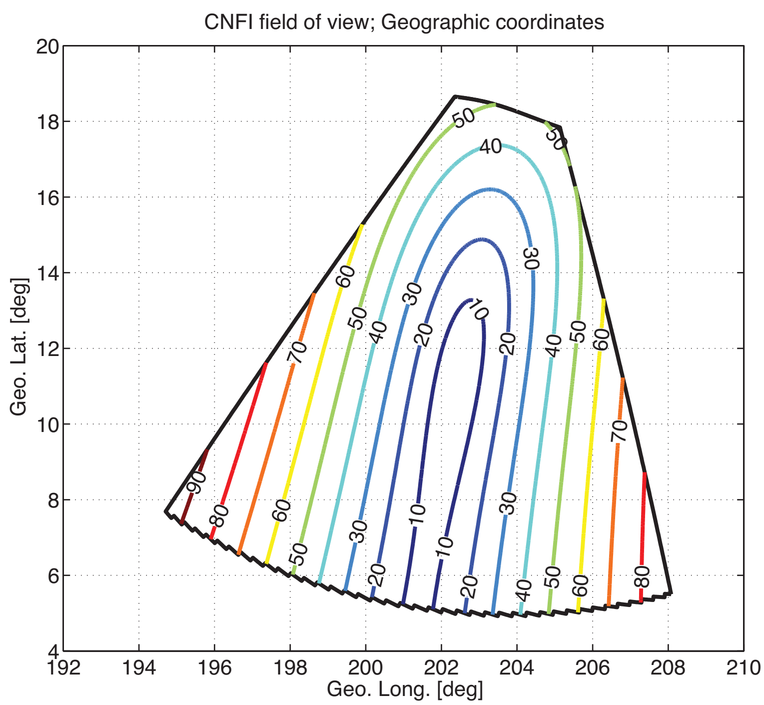

Figure 3.9: Relative spatial blurring across the field-of-view of the Cornell Narrow-Field Imager operating at Haleakala, Hawaii.

3.5 Conclusion

Large-scale electric fields associated with equatorial irregularities map efficiently along the geomagnetic field from hemisphere to hemisphere. This allows the irregularities to grow in a wedge-shape and create an observable impression on the airglow layer. As a consequence of this impression, a three-dimensional map of the irregularities observed in the airglow layer may be created by extruding the image along the geomagnetic field, sweeping out the entire depleted channel. In order to reduce blurring from ray paths that pass through both depleted and normal regions of plasma which are field-aligned, it is advantageous to align imaging systems such that their ray paths are parallel to the geomagnetic field in the airglow layer for this kind of analysis.

CHAPTER 4

LOCALIZATION OF SCINTILLATION-CAUSING REGIONS

4.1 Introduction

There are at least two compelling motivations for locating irregularities in three dimensions. The first is to understand the physics of the irregularity formation and distribution. The second is to compliment, verify, and refine observations made solely from the ground or space.

One common measurement apparatus for scintillation patterns associated with the passage of equatorial plasma bubbles is an array of single-frequency GPS receivers installed on the ground, frequently along a line in the magnetic East-West direction [e.g., *Kintner et al.*, 2004]. For such a system operating at the GPS L_1 frequency (1.57542 GHz), the Fresnel scale is approximately 240 m when the irregularities occupy a slab between 250 and 350 km (z = 350 km, L = 100 km, in Equation (1.8)). For such a system, with the source at zenith, an error of 100 km in altitude results in an error of about 40 m, or 17%, in Fresnel scale. It can be shown that the relative error sensitivity in Fresnel scale is frequency independent. The sensitivity of the irregularity velocity estimate is more difficult to quantify because it involves both geometry- and satellite-dependent terms. Depending on the satellite trajectory with respect to the receiver and irregularities, *Cerruti et al.* [2006] calculated sensitivities from less than 6 m/s for a 100 km altitude error to as much as 36 m/s for the same 100-km error in altitude when using the GPS L_1 signal. For typical zonal irregularity velocities on the order of 150 m/s [e.g., *Kintner et al.*, 2004], this represents an error of 4–24%, respectively.

Occultation experiments are designed to take high resolution vertical cuts through the ionosphere, making them good candidates for observing the altitude of irregularities. However, occultation measurements lack a reliable method of locating irregularities along a ray path to the transmitting satellite. As *Straus et al.* [2003] point out, one cannot simply assign the scattering region to the ray tangent point under scintillation conditions. The argument can be made that the most intense scattering occurs at the location of highest background electron density, which is the F-peak [*Yeh and Liu*, 1982]. As evidenced by reports of scattering regions at high altitudes [*Sokolovskiy et al.*, 2002; *Cerruti et al.*, 2006], this may not strictly be the case.

Another possible analysis technique in the presence of irregularities is to perform a back-propagation inversion on the amplitude and phase data in the phase-screen approximation [*Sokolovskiy et al.*, 2002]. While elegant in principle, this inversion assumes stationarity of the sampled complex field and that a single, well-defined phase screen is the cause of the observed scintillation. Pure radio techniques involving tomographic reconstructions have been proposed [*Bernhardt and Siefring*, 2006]. However, in order to obtain useful resolution, they require sufficient density of instruments, something which is not readily achieved in practice.

In contrast to these techniques that rely solely on data from radio instrumentation, a complimentary technique based on data from a radio instrument and another modality, in this case an optical imager, can be used to reduce the number of assumptions that have to be made in analyzing data in the presence of irregularities. Furthermore, such a dual-modality technique can provide the context of the irregularity regions that cannot easily be obtained from radio-only measurements.

In this chapter, a novel technique for three-dimensional localization of irregularities using GPS radio occultation and a ground-based airglow imager is presented. This demonstrates the field-mapped extent of equatorial plasma depletions and associated irregularities. Furthermore, it provides an independent method to estimate the altitude of an irregularity layer. We begin with a detailed discussion of the instrumentation and technique. Then, we apply the technique to measurements from the American sector during the September–October equinox period in 2006. A discussion of the results and associated caveats is presented.

4.2 Instrumentation and Analysis

For this study, the CTIO narrow-field imager described in Chapter 2 observes the 630.0-nm line due to its relatively high volume emission rate, even during solar minimum. Launched in April 2006, the COSMIC/FORMOSAT-3 constellation of six satellites in low-Earth orbit (LEO) is designed to provide in excess of 2000 radio occultation measurements daily using Integrated GPS Occultation Receivers [*Cheng et al.*, 2006]. Initially, the satellites were placed in a low-altitude orbit at about 515 km. Later, they were raised to final orbits at 800 km one at a time. The data products are provided for each occultation in a variety of formats. Two products of interest to this work are the ionospheric signal-to-noise ratio (SNR) and excess phase data (1-Hz sampling), and the atmospheric SNR and excess phase data (50-Hz sampling). However, the high-rate atmospheric data are only provided for tangent altitudes up to about 150 km, making them less useful for the purposes of this work, which is focused on irregularities at altitudes above 150 km.

Rather than inverting the entire occultation data set from an occultation through irregularities, it is instead instructive to consider other metrics from the data. For example, variation of the received signal strength can be used to compute the normalized variance of the SNR. We infer that radio links exhibiting higher SNR variance traverse irregularities. The SNR variance is computed from the familiar S_4 formula,

$$\sigma^2 = \frac{\langle I^2 \rangle - \langle I \rangle^2}{\langle I \rangle^2}. \tag{4.1}$$

The ray tangent point moves at a velocity on the order of 3000 m/s. At 1-Hz sampling, this suggests that spatial sampling distance is longer than the Fresnel scale, which varies from about 200 to 1200 m for practical occultation geometries. Thus, for the purposes of this technique the SNR variance can serve only as a tracer for the presence of irregularities along the path and not a measure of scintillation intensity or characteristics. Equation (4.1) utilizes the symbol σ to avoid ambiguous interpretation of the results.

In order to corroborate data from the occultations, ground-based scintillation observations from two sites are also considered. The SCINDA (Scintillation Network Decision Aid) station at Ancón, Perú, samples VHF (approximately 250 MHz) beacon signals from the FLEETSAT 7 and 8 satellites at 50 Hz. The approximate ionospheric pierce points of the VHF ray paths are plotted in Figure 4.1. (See *Groves et al.* [1997], *Sheehan and Valladares* [2004], and *Valladares et al.* [1996] for details on the SCINDA instruments.) There are also two GPS scintillation monitors co-located with the airglow imager at Cerro Tololo, Chile. These receivers monitor the GPS L_1 and WAAS (Wide Area Augmentation System) signals for scintillation at a 50-Hz sampling rate. The scintillation monitors are similar to those described in *Beach and Kintner* [2001].

Figure 4.1 outlines the new analysis technique proposed in this chapter. Initially, airglow images captured by the imager at Cerro Tololo, Chile, in which equatorial plasma depletions are visible, are selected for study. COSMIC/FORMOSAT-3 radio occultation events are then selected from the same time and region. Each airglow image can be projected onto the layer representing the peak airglow emission altitude, nominally 250 km for 630.0-nm, as shown in Figure 4.1a. A depletion mask containing the region of the image in which a depletion is present is created from each of the airglow images nearest to the times of occultation. The depletion mask is then projected onto the airglow layer. In order to reduce computational complexity when handling the geomagnetic field lines (discussed below), the masks are binned-down by 16×16, yielding a horizontal resolution of

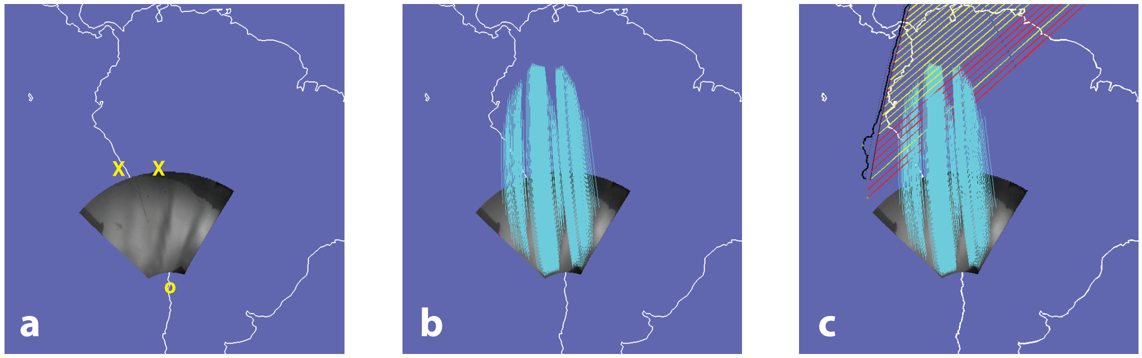

Figure 4.1: Illustration of the three-step extrusion procedure used in this work. (a) The airglow image is projected onto the assumed airglow layer height of 250 km. The locations of the ionospheric pierce points (x) of two look directions of the SCINDA station at Ancón, Perú, and the imager (o) at Cerro Tololo, Chile, are marked. (b) The field lines corresponding to depletions in the airglow are selected to create a three-dimensional map of the field-aligned depletion. (c) Occultation ray paths connecting a GPS satellite and a COSMIC/FORMOSAT-3 satellite have been added. The COSMIC/FORMOSAT-3 satellite is orbiting over the western coast of South America and over Panama. The ray paths in red correspond to $\sigma > 0.10$, indicating some irregularities are present along the ray path. Note that these ray paths are also crossing the geomagnetic field lines associated with the depletion.

approximately 20–150 km at the airglow layer altitude of 250 km. The field lines with the lowest apex altitudes yield the better resolutions. It is well-understood that large-scale (> 10s of km) electric fields associated with depletions map efficiently along the geomagnetic field lines from the geomagnetic equator to low latitudes [e.g., *Farley*, 1960; *Otsuka et al.*, 2002]. At smaller scales, this approximation breaks down. Since this scale is of the same order as the horizontal resolution above, that approximation is valid. Invoking this assumption, the resulting projection is extruded along the geomagnetic field using the AACGM (altitude-adjusted corrected geo-magnetic) model with epoch 2000 coefficients [*Baker and Wing*, 1989]. Extrusion along the geomagnetic field represents the three-dimensional space occupied by the depletion, as shown in Figure 4.1b.

Neglecting diffraction and refraction effects, which should be negligible, the straight line between the COSMIC/FORMOSAT-3 and GPS spacecraft define a ray path. The occultation ray paths that cut through the extruded depletion map are located by computing the intersection between the ray paths and the affected field lines. The present algorithm only locates intersections below the satellite orbit. This computation is performed at each time step, regardless of the variance at the time, and the resultant ray paths are sorted by intersection altitude and SNR variance. The variance (σ^2, Equation (4.1)) is computed from the SNR of the GPS signal received during occultation. For this work, the variance was taken on L_2 over twenty 1-Hz samples. Figures 4.1c and 4.2 show example composites of SNR variance, ray paths, and airglow, for the same event on 15 September 2006.

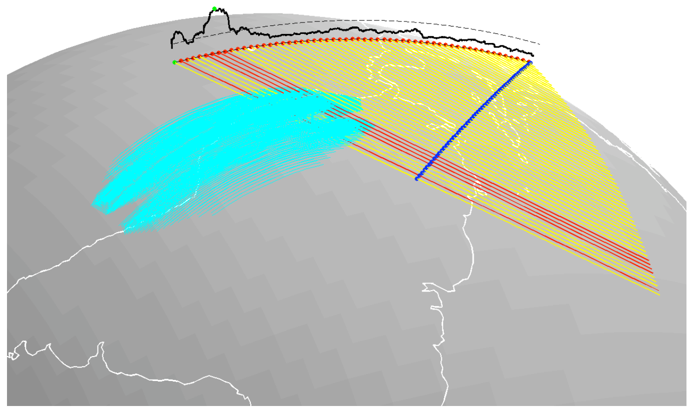

Figure 4.2: Three-dimensional view illustrating the problem geometry. The cyan curves represent the depletion region as estimated by extruding the airglow image. The black curve above the LEO (COSMIC/FORMOSAT-3) orbit on the top (left) ends of the ray paths is a relative measure of SNR variance. Only every 10th ray path is shown for clarity. The ray paths highlighted in red have increased SNR variance, suggesting that they host irregularities. Only the portions of the ray paths that are below the orbit of the LEO are shown. Blue dots are placed at the tangent point for each ray path. This illustrates the distance ($\sim$ 500 km) between the bubble intersection and the tangent point.

These illustrate clearly the increase in SNR variance as the ray paths cut through the depleted wedges of field lines.

An alternate viewing geometry is that in Figure 4.3. The airglow image has been mapped along the geomagnetic field onto the surface formed by the occultation ray paths. Doing so allows the intersection altitude between the occultation ray paths and bubbles to be easily inferred. The broken and solid lines indicate the beginning and end of fading on the GPS signal received during the occultation. Intersections with three bubbles are also indicated by dots. Note that due to the geometry and projections involved in creating this figure, part of the image is mapped to physically unrealistic low altitudes. However, note that there are no SNR variations associated with ray path intersections at these low altitudes. Finally, Figure 4.3 illustrates the amount of each ray path that passes through the imager's extruded field of view. The most suitable occultation events were selected for this study by requiring that at least 50% of the segment of each ray path below the LEO orbit be within the field-aligned volume observable by the imager. This ensures the best possible chance of unambiguously observing the irregularities.

It is evident from Figures 4.2 and 4.3 that ray paths frequently cross multiple depletions, particularly on East-West ray paths. In this work, we take the mean altitude of intersections that occur on ray paths with "shallow" slopes that vary less than 50 km over the depleted region. For example,

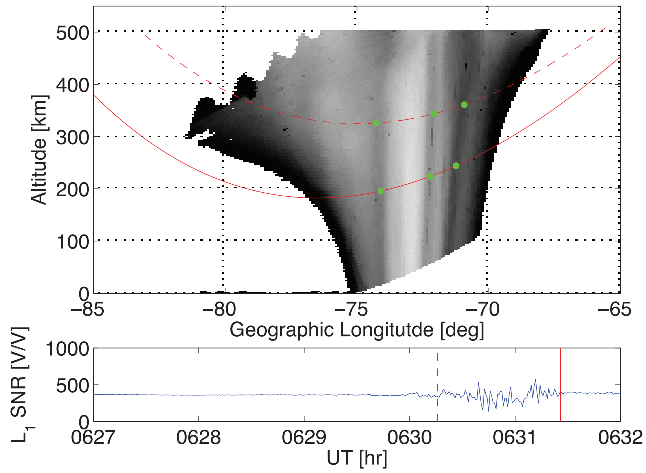

Figure 4.3: The top panel shows an example of an airglow image mapped along the geomagnetic field onto the surface swept out by the occultation ray paths. This extrusion allows the altitude of the irregularities to be read off the plot directly. COSMIC GPS L_1 SNR is shown in the bottom panel. The dashed and solid lines correspond to the beginning and end of irregularities inferred from the COSMIC occultation SNR data, respectively. Corresponding lines are drawn on the projected airglow image in the top panel. Markers indicate the position of depletions in the airglow image. The mean altitude of the intersection of the ray path and airglow depletions is recorded as the irregularity altitude for that ray path. Thus, irregularities are inferred to occur over a range of 210–350 km.

in the case of the end of the irregularity observation (solid line) shown in Figure 4.3, intersections are found at 190 km, 210 km, and 230 km. A value of 210 km is recorded for that ray path. Ray paths that cut through depletions over a range of altitudes larger than 50 km are not included in this analysis. Figures 4.2 and 4.3 also show the distance from the tangent point to irregularities. Although the tangent point is not specifically marked in Figure 4.3, it is at the point of minimum altitude in each of the ray paths. It is clear that the irregularities may be some distance, in this case $\sim$ 500 km, from the tangent point.

4.3 Results and Discussion

The temporal distribution of airglow images (thick colored bars) and occultation measurements (points) considered in this study is plotted in Figure 4.4. During the study period, 7 September–27 October 2006 (days 254–300), there were 14 individual occultation events (marked by blue circles) that substantially crossed the "geomagnetic" field-of-view of the imager when bubbles were observed. Several of the events are nearly temporally coincident and therefore indistinguishable on the plot. All of these occultation events exhibited some increase in SNR variance over a portion of the altitudes

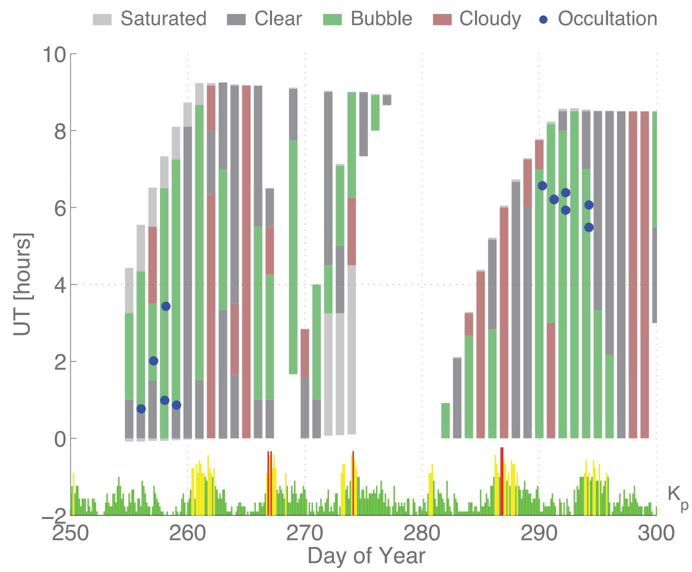

Figure 4.4: The temporal distribution of selected occultation events and the availability of airglow imagery data. Individual occultation events are marked with a blue dot. By default, the imager collects data between sunset and moonrise or between moonset and sunrise, as the case may be. The relative lack of coincident airglow and occultation data for days 260–289 is mostly a function of data availability, not a lack of bubble activity. The K_p index is plotted along the bottom.

covered by the occultation. Geomagnetic activity, plotted through the K_p index at the bottom of Figure 4.4, was relatively quiet on the days of interest, so this study focuses on quiet behavior of irregularities associated with bubbles and scintillation. In Figure 4.4, the lack of events during days 260–289 is because there were no coincident examples of bubbles and occultations in the data sets. The time period from 276–282 has no imaging data due to moon-up conditions.

The data fall cleanly into pre-midnight (UT < 0400) and post-midnight (UT ≥ 0400) bins. The altitude distribution inferred from the pre-midnight events is shown in Figure 4.5. The envelope of the plot shows the number of occultation ray paths intersecting plasma bubbles in each altitude bin. Intersections are considered all the way down to the Earth's surface, although the irregularity electric fields dissipate with decreasing altitude. Ray paths are considered to intersect irregularities if the SNR variance $\sigma > 0.10$, which is larger than the apparent noise floor of the COSMIC GPS occultation receivers. These irregularities are seen to be constrained between 200 and 375 km with a mean altitude for $\sigma > 0.10$ is 306 km and a standard deviation of 50 km.

After midnight, shown in Figure 4.6, the data become more interesting. Notice that the relative proportion of high-altitude intersections (any shading, not just irregularities) is greater than before midnight. This is indicative of mature plasma depletions observed in the airglow that have grown to high altitude, but no longer contain irregularities at the correct scale to cause scintillation of

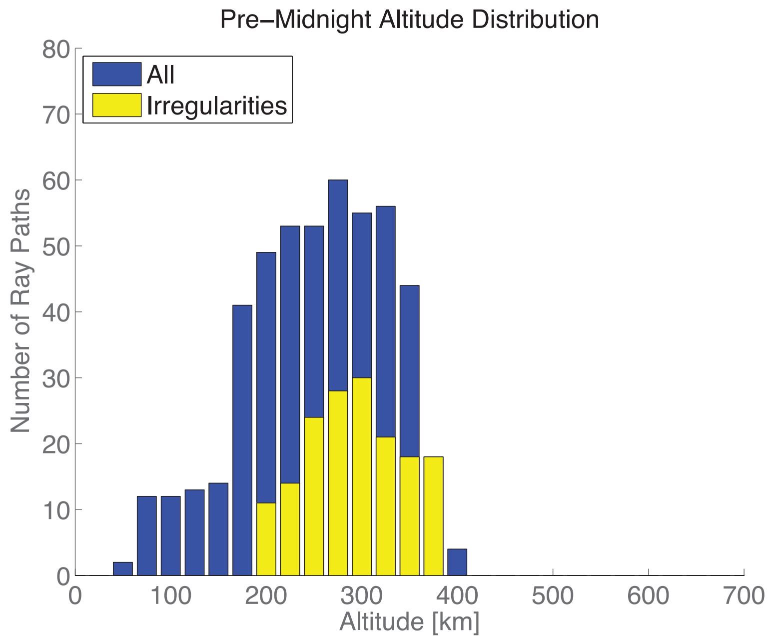

Figure 4.5: Distribution of intersection points with altitude and σ in the pre-midnight (UT < 4) time frame. Due to the availability of coincident data, this corresponds to data taken during days 254–270. The "All" statistics show all intersections between identified depleted flux tubes and occultation ray paths, regardless of σ. The "Irregularity" statistics show the distribution of intersections between depleted flux tubes and occultation ray paths that exhibit $\sigma > 0.10$.

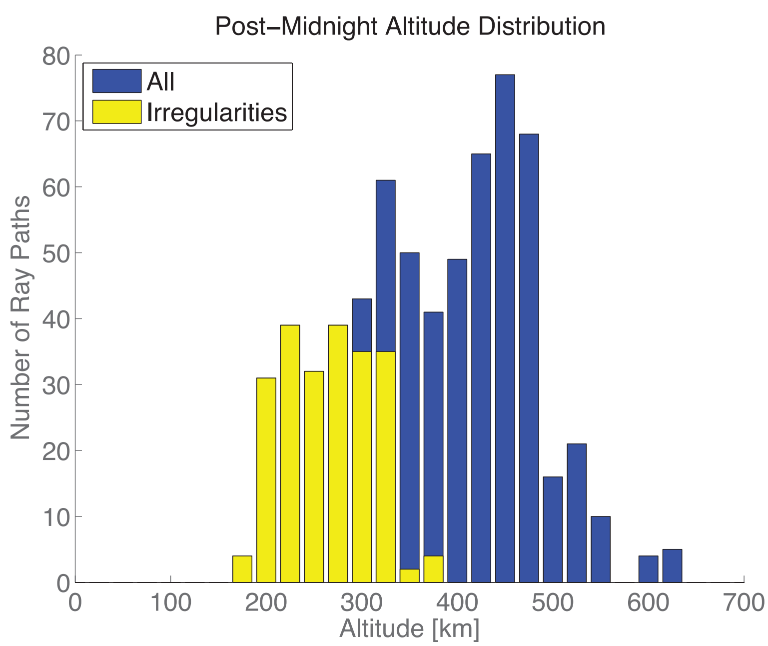

Figure 4.6: Similar to Figure 4.5. Due to the availability of coincident data, this corresponds to data taken during days 280–300.

the GPS signal. As observed in airglow images, these depletions will persist until ion production resumes at sunrise. The mean altitude for the post-midnight events with $\sigma > 0.10$ is 278 km with a standard deviation of 46 km.

There is also an abrupt decrease in the number of intersections at 500 km since we have only computed intersections below the satellite orbit altitude. Most of the COSMIC/FORMOSAT-3 satellites were in a low-altitude holding orbit of 515 km during the observation period. This upper limit will be improved for dates after all of the satellites reached their final 800 km orbit altitude in Fall 2007. At that point, the particular imager used in this study will limit the useful altitude to about 700 km. However, this restriction is not universal and there are imaging systems whose fields of view map to higher apex altitudes.

Together, the irregularities detected pre- and post-midnight span an altitude range of 175-375 km. Detection of irregularities along the occultation link would require sufficient electron density at the irregularity layer, implying that for the lower end of our height estimates to be valid, the F peak would have to descend to a relatively low altitude. Using the Jicamarca incoherent scatter radar, *Hysell et al.* [2008b] have shown that the F layer can indeed descend to low altitudes at night, approximately 250 km, during solar minimum conditions, such as those prevalent during our observations. This suggests that the lower irregularity heights obtained from our method are indeed feasible although we lack direct evidence.

In order to verify that ground-based scintillation was observed coincident to that on the occultation paths, 250-MHz and L-band scintillation observations from the SCINDA station at Ancón, Perú, were studied. Scintillation index (S_4) data are plotted for the VHF links in Figure 4.7. The black dashed lines correspond to occultation events considered in this study. Since some of the occultation events are nearly coincident in time, some of the lines are indistinguishable. Each occultation event identified in this study corresponds to 250-MHz $S_4 > 0.25$ at the SCINDA site. No scintillation was observed at L-band for this station (not shown). However, a GPS L_1 scintillation monitor co-located with the airglow imager at Cerro Tololo, Chile, did observe increased S_4 around most of the events, including several at $S_4 \approx 0.4$. These S_4 data are plotted in Figure 4.8. The difference in L-band scintillation at the two sites probably arises from $\nabla N/N$ differences for ray paths to the two stations. Ancón lies in the lower density region between the equatorial arcs, while Cerro Tololo lies near the southern edge of the southern arc.

One of the assumptions made in this new technique is the altitude of the airglow emission layer. As mentioned above, deviation from the assumed layer height will affect the spatial characteristics

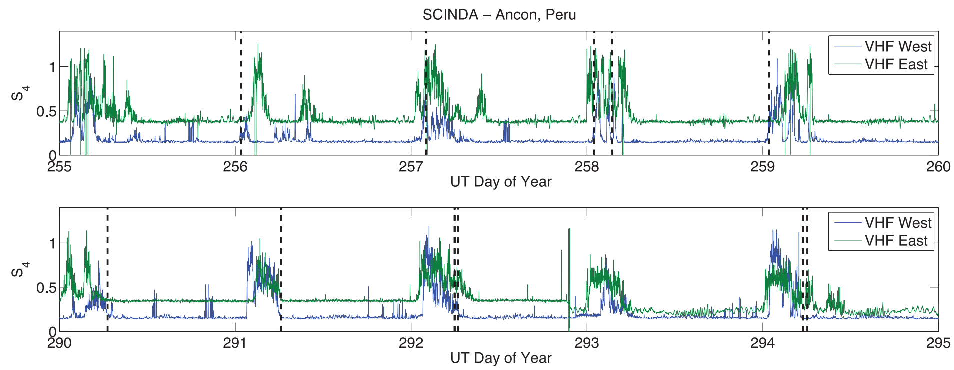

Figure 4.7: VHF scintillation recorded by the SCINDA station at Ancón, Perú. The heavy vertical dashed lines correspond to the times of occultations used in this study. Each occultation corresponds to scintillation on one or both of the VHF links; see text for discussion. Note that several of the occultations are nearly coincident in time and are not distinguishable on these plots.

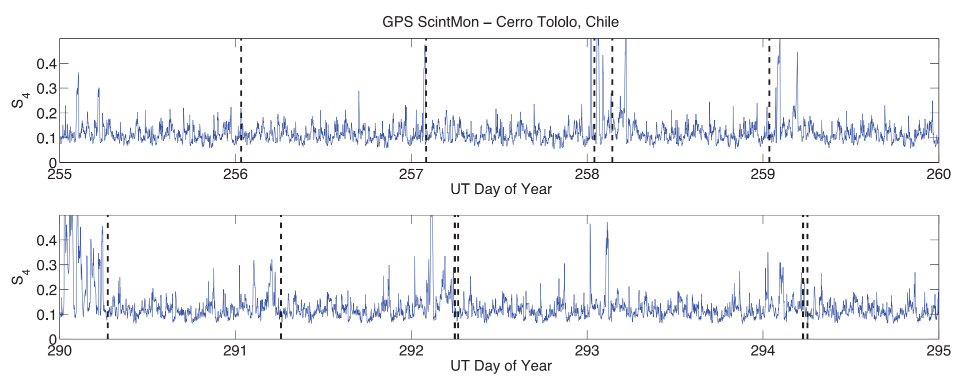

Figure 4.8: *L*-band scintillation recorded by a GPS scintillation monitor at Cerro Tololo, Chile. Occultations are marked with dashed vertical lines. Notice that Cerro Tololo's position below the equatorial arcs affords greater opportunity to observe scintillations due to increased background electron density. See text.

inferred from the images. Thus, it may be reasonable to expect these errors to affect our results. To examine the effects of our assumed airglow emission altitude, we performed a simple numerical experiment. The error in the predicted field line apex altitude between two layer heights can be considered an upper-bound for the altitude error due to an incorrect airglow layer height estimate. Emission layer modeling using NRLMSIS-2000E [*Picone et al.*, 2002] and IRI 2000 [*Bilitza*, 2001] suggest that a height perturbation of $\pm$ 10 km is common in the region of interest. However, for the purpose of demonstration, we have perturbed the emission height by 50 km up to 300 km. From the AACGM with 2000 coefficients, we computed the field line apex altitudes using the 250 km and 300 km layer heights and the viewing geometry from the imaging system at CTIO. Most of the errors were considerably lower than the layer perturbation of 50 km, with 92% of errors being 30 km or less. For a more typical height perturbation of 10 km, an error of less than 12 km is expected. Note that these errors do not necessarily scale linearly. Thus, the results presented here can be viewed with confidence even if the actual height of the airglow layer varies significantly.

The present results are in agreement with the forward-scatter observations of *Bhattacharyya et al.* [2001] of an irregularity layer near 350 km in western South America using data from the Ancón SCINDA station. However, our data suggest that irregularities may be present over a wider range of altitudes, 200–375 km. Our technique also confirms the assertion of *Straus et al.* [2003] that the scattering region may be far from the ray tangent point, as evidenced in Figure 4.2 in which the tangent location is far to the east of the intersections observed by the imaging system. Although the technique presented here does require a ground-based imager, no geostationary satellite is required as a reference data source as in *Cerruti et al.* [2006]. Perhaps the most important feature of this technique is that unlike the others cited, it does not require 50-Hz GPS data to be stored for analysis. Variance indices computed internally from 50-Hz data or from even lower sampling frequencies such as those used here are acceptable, although irregularity scale and scintillation parameters may be difficult to interpret from under-sampled measurements such as these.

4.4 Summary

In this chapter, a novel technique for localizing scintillation-causing irregularities in the equatorial ionosphere using radio occultation and field-aligned airglow images was discussed. Data collected during days 254–300 of 2006 suggest that most ionospheric scintillation during this time period occurred due to irregularities in the 200–375 km altitude range. The present results indicate that higher-altitude irregularities are uncommon during relatively quiet geomagnetic conditions.

CHAPTER 5

RELATIONSHIP BETWEEN COHERENT BACKSCATTER AND AIRGLOW DEPLETIONS

5.1 Introduction

The post-sunset equatorial ionosphere is capable of extreme volatility due to the abrupt transition from the daytime E-region dynamo to the nighttime F-region dynamo. This transition manifests itself in the pre-reversal enhancement of the zonal eastward electric field and various irregularities known collectively as equatorial spread-F [*Kudeki et al.*, 2007]. Both forward-scatter radio scintillation observations and in-situ rocket and satellite density probes suggest that a broad spectrum of irregularity scales are present. These measurements also suggest that there are at least two different spectral characteristics, one at smaller scales ($\leq$ 100 m), and the other at larger scales. In response to this observation, it has been theorized that there are two or more irregularity process classes operating [e.g., Chapter 1; *Woodman and Basu*, 1978; *Yeh and Liu*, 1982; *Kelley*, 1989; *Hysell and Farley*, 1996, and references therein].

The larger irregularity scales are widely supposed to be the result of an interchange instability, as first suggested by *Dungey* [1956]. The smaller scales are thought to be a drift wave operating within the depleted regions and driven by non-linear coupling to a larger-scale interchange instability [*Hysell and Farley*, 1996]. Another suggested mechanism is a wind-driven gradient-drift instability—either meter-scale or in cascade [*Sekar et al.*, 2007]. Although the irregularities represent a continuum of scales, most remote techniques for observing them are sensitive to particular scales. Radio scintillation and coherent radar echoes are due to smaller scale irregularities at the Fresnel and Bragg scales, respectively. Optical airglow imaging and incoherent radar backscatter are able to detect the larger-scale structures, on the order of a few kilometers and larger. It is well-known that the meter-scale irregularities observed via coherent backscatter decay more rapidly than the 100-meter-scale irregularities responsible for scintillation [*Basu et al.*, 1978]. This also extends to the even larger depletions observed in the airglow, which frequently remain until ionization resumes at sunrise [e.g., *Makela*, 2006].

The first comparative study of the relationship between Bragg-scale irregularities causing coherent echoes and plasma depletions was undertaken by *Tsunoda* [1980] using the ALTAIR (ARPA Long-range Tracking and Identification Radar) system on Kwajalein Atoll in the Marshall Islands. This study utilized the steerable capability of ALTAIR to confirm the aspect sensitivity of coherent backscatter echoes to the geomagnetic field. Furthermore, the aspect sensitivity of coherent echoes was leveraged to perform an incoherent backscatter analysis of the off-perpendicular returns and confirm that the coherent backscatter emanates from the depleted regions. More recently, this type of work has been extended to optical airglow imaging systems and coherent backscatter in the East Asian Sector [*Otsuka et al.*, 2004b; *Saito et al.*, 2008]. In both cases, the data have come from limited periods of time due to instrument availability (notably ALTAIR) and, in the later studies, atmospheric observing conditions at the airglow imaging site. Given the manifest variety of formations in which equatorial irregularities appear, it is compelling to consider a long-term data set.

In this chapter, a long-term coincident study of airglow and radar data is presented from a field-aligned airglow imaging system (CNFI) at Mount Haleakala, Hawaii, and a 50-MHz coherent backscatter radar at Christmas Island, Kiribati (CXI). Several interesting examples are considered, as well as a reduction of the entire airglow imaging and radar backscatter data set from January 2002–January 2009. The first section treats analysis techniques employed to reduce the data. The next section discusses the selection of the data and general characteristics. The final section considers specific geophysical implications.

5.2 Instrumentation and Analysis

Equatorial plasma depletions are observed by the CNFI system described in Chapter 2 through the impression left by their internal electric fields in the airglow emission layer (nominally 250-km altitude for the 630.0-nm emission). In Chapter 3, we saw that electrostatic modeling and observations suggest that electric fields associated with irregularities of scales greater than approximately 10 km map efficiently along the geomagnetic field, affecting a wedge-shaped region that extends from the northern to southern hemisphere. Given that the range gates of the CXI radar are also spaced at 10-km intervals in altitude and that the integrations occur every 75 seconds (assuming an eastward drift of 100 m/s, this works out to 7.5 km in the zonal direction), we are comfortable making the approximation that irregularities observed in the airglow can be extruded along the geomagnetic field for comparison with the radar as described in Chapter 4 and Appendix C.

The extrusion is performed by mapping the pixels of the imaging sensor to an assumed peak emission altitude of the airglow, 250 km for this work, unless specified otherwise. That is, the ray path corresponding to each pixel is traced until it intersects the airglow layer. The intersections are recorded in geographic coordinates. For the purpose of this work, the centroid location of each range gate on the north beam of the Christmas Island radar has been traced along the geomagnetic field until it insects the airglow layer as well. This allows the airglow intensity corresponding, geomagnetically speaking, to each range gate to be interpolated. Thus, for each radar integration time step, there are 100 backscatter range gates *and* 100 airglow intensities. These may be assembled in a standard range-time-intensity (RTI) backscatter map [*Woodman and Hoz*, 1976] and a so-called keogram of the airglow. We will refer to the combination of an RTI map and a keogram, examples of which are shown in Figure 5.1, as an "RTI gram." This kind of representation was first employed by *Makela et al.* [2009].

Furthermore, we have extracted an estimate of the plasma drift velocity as a function of time and apex altitude from the sequence of airglow images. This technique is a modification of those described by *Makela and Kelley* [2003a] and *Yao and Makela* [2007]. The drift velocity extraction procedure begins by detecting the brightest stars in the image and applying a median filter to their vicinities to remove them. Next, the image is convolved with a 3×3 Sobel edge-detection operator. Pixels corresponding to the desired field-line apex altitude are selected to produce a one-dimensional slice of the image, which is filtered with a boxcar filter (length 16, corresponding to about 40 km) to reduce noise. The correlation between slices at adjacent time steps can be used to estimate the drift velocity by converting the lag from pixel space to geographic space to linear distance. While this technique for computing the drift velocity is not new, applying it to different apex altitudes provides insight into the types of drifts observed and may be an important classification tool in the future. A quality-of-fit index is assigned to each velocity computation based on the strength of the correlation. Presently, this is the value of the maximum correlation at the lag used to compute the velocity. The velocity and quality-of-fit data are combined as altitude-time series for plotting on axes similar to the RTI gram.

The drift velocity estimation is important primarily from a classification standpoint. It allows different structures to be detected in the airglow, notably clouds, depletions, and MSTIDs. This permits the reader to quickly identify the relationship between the structures seen in the RTI gram (both radar and airglow) and their motions in the airglow.

5.3 Data

The data selected for daily study come from 2004 and 2005, all during the period 12 August through 12 September, which is during the season in which equatorial irregularities are typically prevalent in the central Pacific as shown in previous climatology studies from Haleakala and the U.S. Defense Meteorological Satellite Program (DMSP) [*Makela et al.*, 2004; *Gentile et al.*, 2006]. There are two consecutive days selected from 2004 and six consecutive in 2005, plus one other that is interesting. These days were picked for their illustrative value or because they were representative, not because they constitute a valid statistical sample. Most of the days correspond to relatively quiet geomagnetic conditions and clear or mostly clear observing conditions at Haleakala. There is one storm day, 24 August 2005, with $K_p = 8+$ observed at 0900 UT. All daily plots have a header that indicates the year, day-of-year, and date, in addition to a plot of 11 days' K_p data, five preceding and five following the day of interest. The bars are color-coded with the usual green for $K_p \leq 3$, yellow for $3 < K_p < 5$, and red for $K_p \geq 5$. A small gray box behind the bars indicates the exact time period for the optical and radar data shown, which corresponds to approximately 0600–1500 UT every day.

Figure 5.1 shows composite RTI gram and drift velocity estimates (from the airglow) on 19–20 August 2004. In order to make a meaningful comparison between the keogram (top for each day), RTI gram (middle), and velocigram (bottom), the altitude coordinates have been transformed to the field line apex altitude. Unless specifically described otherwise, this will be the standard display format for all daily data in this chapter.

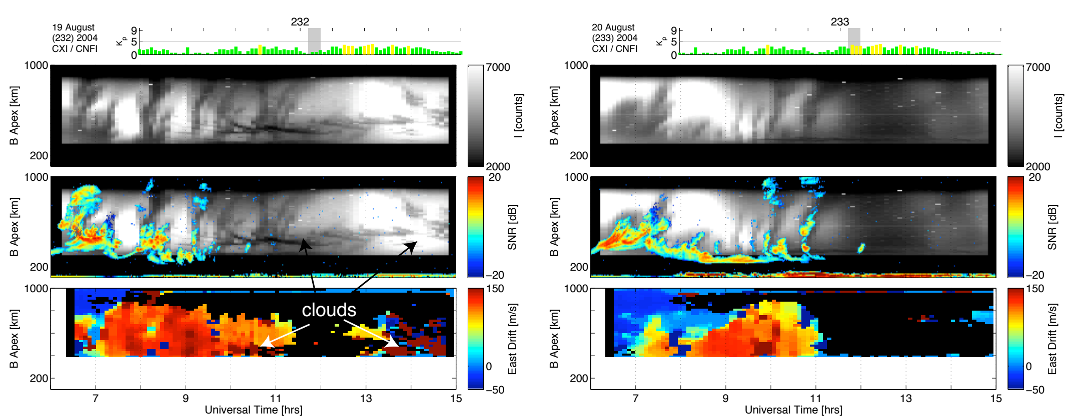

Figure 5.1: Composite keogram (top for each day), RTI gram (middle), and airglow velocigram (bottom) for 19 and 20 August 2004. See text for discussion.

The radar backscatter data in the RTI gram are a classical RTI backscatter map showing SNR as a function of (apex) altitude and time. The relatively solid line of backscatter along the bottom of the map around 100 km in altitude is due to electrojet instability waves. The blackened regions in the velocigram correspond to points for which the logarithm of the peak frame-to-frame airglow correlation value is at least 0.25 standard deviations below the mean for the entire data set. This condition is an ad hoc indicator that little coherent object motion was tracked in the image at that time and location. The algorithm also tends to recognize the rapid brightening or dimming of the airglow as a coherent motion, although it often reports zero velocity. Also note in Figure 5.1 that saturations ($\geq$ 150 m/s) in the drift velocity tend to correspond to clouds, which appear to move much faster than the depletions due to the parallax effect. The drift velocity also helps identify airglow structures that remain in the image after the backscatter ceases.

Figure 5.2 contains data from six consecutive days, 24–29 August 2005 in the same format as Figure 5.1. This is meant largely to illustrate the day-to-day variability of the structures. The first two days, 24 and 25 August, show some geomagnetic activity. 24 August (236) 2005 is interesting because there are two layers of backscatter. This is relatively uncommon and occurs perhaps once or twice per year. The finger-like structure between 1300 and 1430 UT propagates with a westward component, as seen in the drift velocity plot. Common structures that propagate with a westward component are mesoscale traveling ionospheric disturbances (MSTIDs), which propagate to the southwest in the northern hemisphere under geomagnetic quiet conditions. The next three days, 26–28 August, are typical geomagnetic quiet days. And, finally, 29 August is a day with no bubble activity included as a control and to illustrate the effectiveness of the airglow velocity extraction method as a technique for detecting depletions.

Figure 5.3 is a climatological reduction of CNFI and CXI data for 2002–2009. The black regions in each plot indicate periods when data were unavailable or unusable (poor SNR). The color-coded percentages correspond to the percentage of days in a 20-day sliding window in which equatorial plasma bubbles or 3-meter backscatter were observed, respectively. The CNFI airglow images were classified visually into four categories: clear, cloudy, bubble, or unusable. Cloudy and unusable days were lumped together as unusable for this presentation. The CXI backscatter was tallied for received levels of > -10 dB and > 0 dB above the thermal noise level on the CXI east beam. We have also included the 3-hour K_p index and the daily 10.7-cm solar flux for the period. The K_p index is sorted into bins and color coded just as it is for the composite RTI grams: green for $K_p \leq 3$, yellow for $3 < K_p < 5$, and red for $K_p \geq 5$.

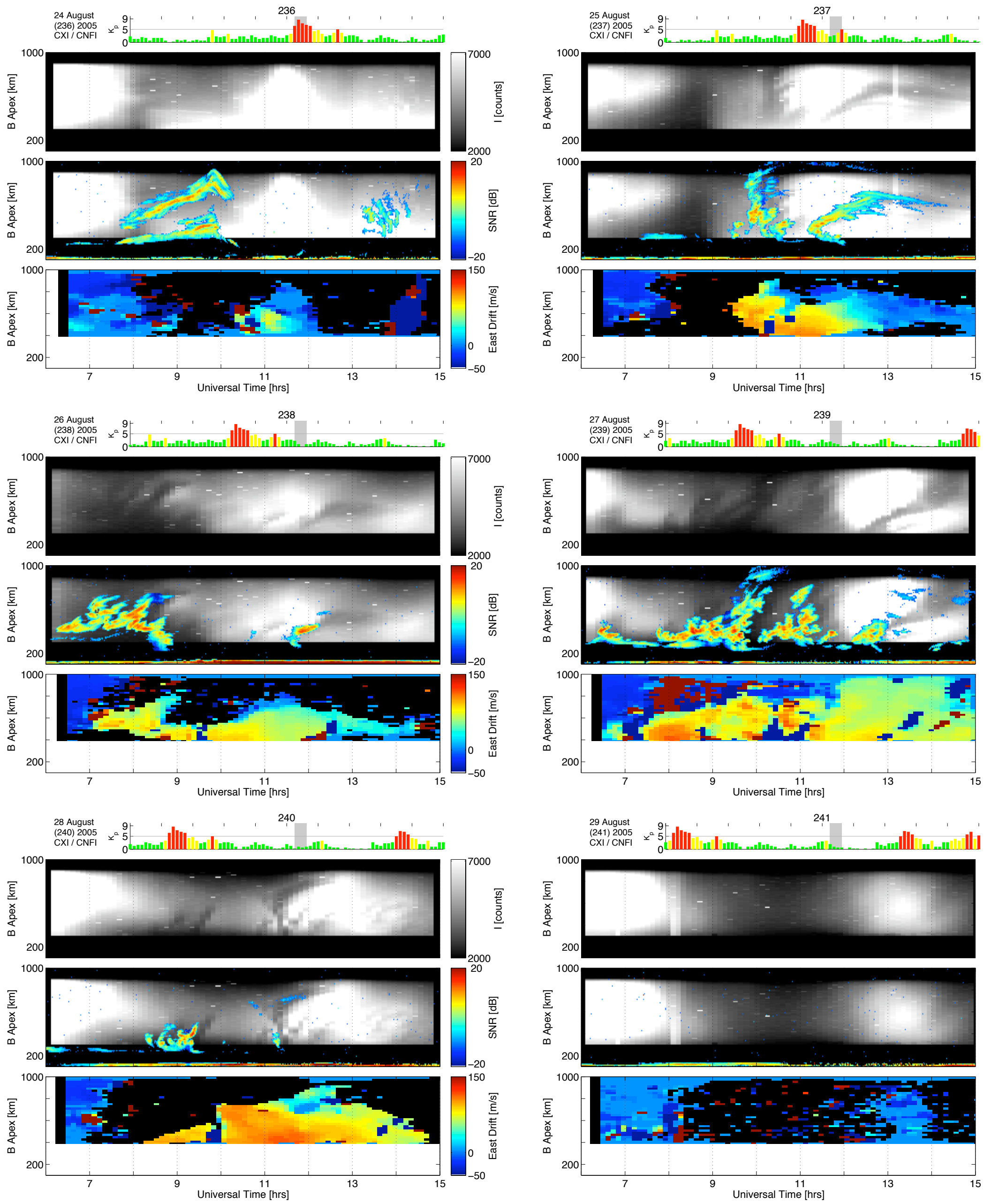

Figure 5.2: Composite data for each day 24–29 August 2005. The format of the plot is the same as Figure 5.1.

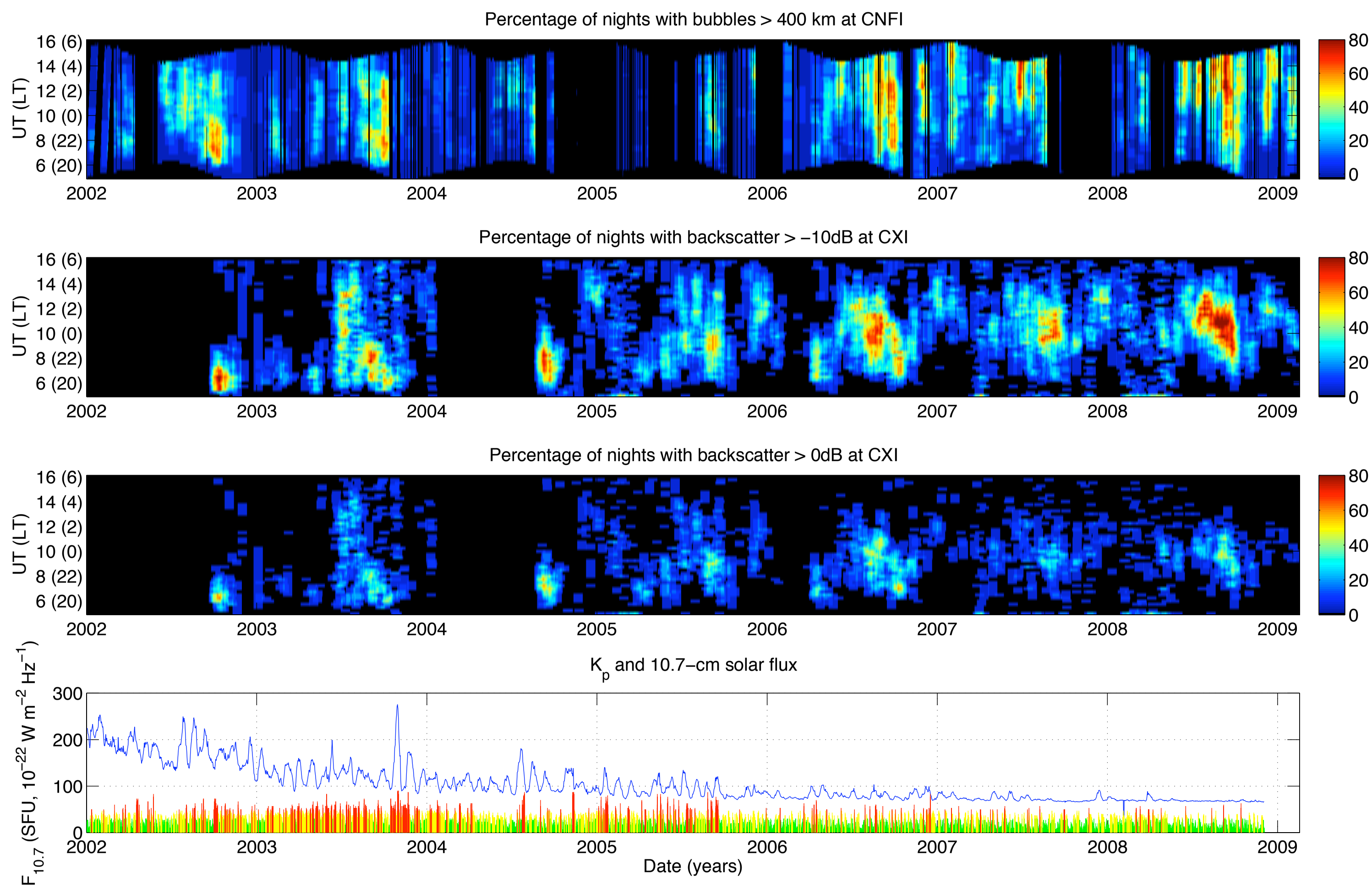

Figure 5.3: Climatological reductions of the CNFI airglow image (top), CXI radar backscatter (center two), and solar flux and K_p index (bottom) data sets for 2002–2009. The colors represent 20-day sliding percentages of days when irregularities were observed.

5.4 Discussion

5.4.1 Depletions and backscatter

Even at a visual glance, the observations in Figures 5.1 and 5.2 appear to confirm assertions that the most intense backscatter emanates from locations that are geomagnetically connected to the depleted regions observed in the airglow. A cut across all times at a fixed altitude (single range gate) illustrates this even better. Figure 5.4a shows normalized cuts of airglow and backscatter intensity at ranges corresponding to apex altitudes of 300, 450, and 600 km, from 19 August 2004. The backscatter does appear to be well-correlated with the depleted regions of airglow. In contrast, Figure 5.4b, from 12 August 2005, exhibits a time-lag between the backscatter and some of the airglow depletions. This raises two possibilities, assuming proper spatial calibration of the imager system and radar. The first is that there is indeed backscatter coming from the eastward wall of the depletion. That is, since the depletion is drifting eastward, irregularities on the wall begin to appear in the radar beam before the depletion is observed in the airglow image. This theory gains credence from the observation by *Ledvina and Makela* [2005] that the eastern walls of depletions contained more spectral power at small scales than the western walls as they passed a geostationary SBAS satellite link. The second alternative explanation is that the airglow emission altitude has deviated from the nominal 250-km estimate. This will be discussed further in the next subsection.

Another compelling observational argument for the majority of the backscatter arising from the depleted region may be illustrated by the following cartoon. Consider a radar beam convolved with a medium containing backscattering irregularities frozen onto two walls of a depletion. Next, consider the same radar beam convolved with a medium containing a single (again frozen) block of scattering irregularities. Unless the beam is sufficiently wide to illuminate both walls of the depletion, the signatures of the two structures differ greatly, as illustrated in Figure 5.5. Naturally, this argument requires that the drift is constant and the morphology of the scatterers remains constant. The drifts extracted from the airglow, plus the *fact that the drifts can be extracted* from the airglow using correlation, suggest that these conditions are approximately met. Notice that the backscatter envelopes tend to have soft edges, coming to a near maximum in the middle of the envelope before tapering back to a soft edge on the other side. If backscatter were to be arising from both edges, the backscatter would be greater at the edges than in the center. A gradient drift instability requires the wind to be antiparallel to the plasma density gradient in order to grow, which in the case of an eastward wind, would not occur on the eastward wall of the depletion [*Sekar et al.*, 2007]. It is most likely, therefore, that the 3-meter irregularities are indeed within the depleted region, perhaps being driven by or propagating from a gradient drift instability on the western wall.

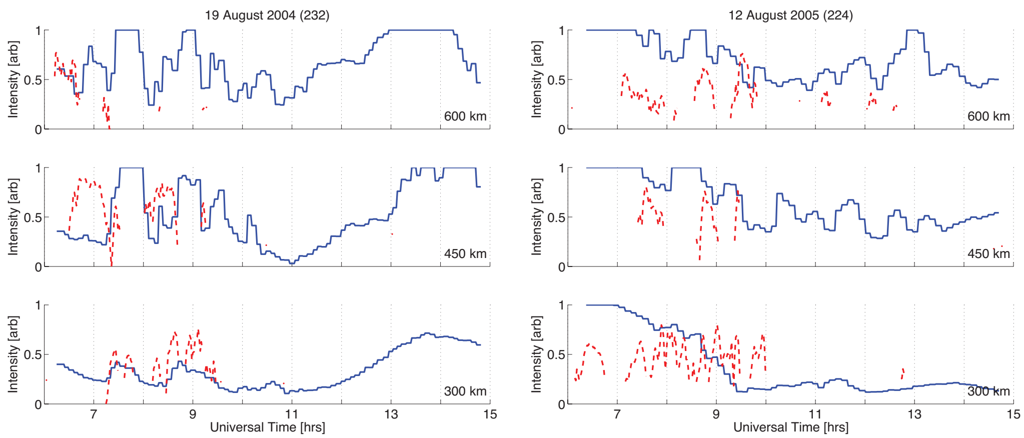

Figure 5.4: (a) RTI gram time series cuts from 19 August 2004 corresponding to apex altitudes of 300, 450, and 600 km. The solid (blue) line corresponds to the airglow intensity. The dashed (red) line corresponds to radar backscatter. These quantities are normalized over ranges of [1000,7000] counts and [-20,20] dB, respectively, to create the [0,1] scale. Although it is difficult to make out some of the structure on the low-altitude plot, the higher altitude plots show that the backscatter coincides with the depleted regions. (b) RTI gram time series cuts from 12 August 2005. In this case, there appears to be some “phase shift” between the airglow images and the radar backscatter, e.g., 600 km between 1100 and 1300 UT. See text for discussion.

5.4.2 Airglow layer altitude estimation

One of the well-known limitations of airglow imaging is knowledge of the emission layer altitude. This problem is particularly vexing with the 630.0-nm emission because, although easy to observe due to its high emission rate, it is strongly dependent on both neutral density and electron density profiles. Knowledge of the emission altitude is crucial because it affects the perceived interpretation of the impact of the irregularities observed in the image when they are transformed from pixel coordinates to geographic coordinates. Figure 5.6 illustrates the effect of varying the assumed emission altitude from 220 to 440 km when producing RTI grams of data from 12 August 2005. Notice that the airglow and backscatter seem to match best at layer altitudes above 300 km on this day. The brightening around 1300 UT corresponds to the lowering of the ionosphere. Correspondingly, the little remaining backscatter at 1400 UT seems to match better at lower altitudes again.

Correlations have been computed over a 60-minute window in 20-minute steps to estimate the layer altitude. In Figure 5.7, these altitudes are compared with an airglow emission profile modeled

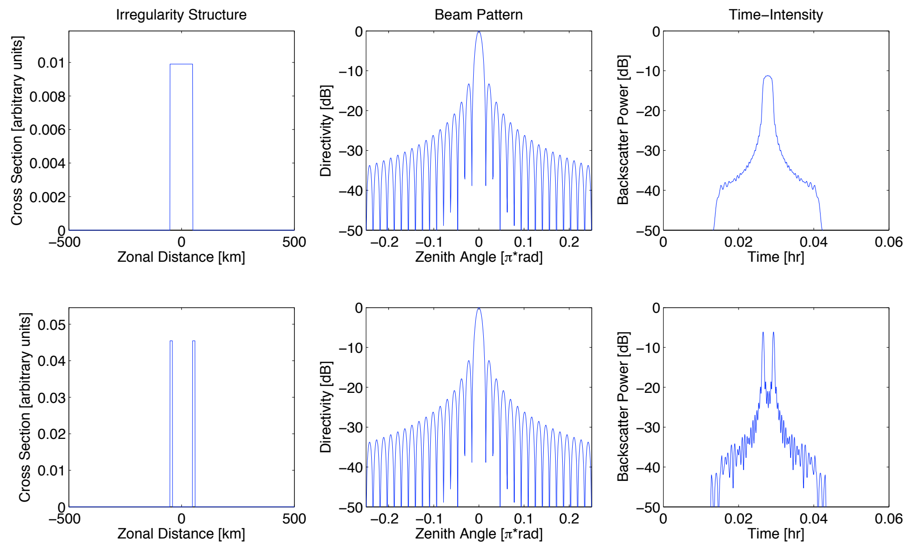

Figure 5.5: Series of cartoons that illustrate two example irregularity location scenarios. The top row illustrates a block of irregularities located in the depleted region (left), convolved with a radar beam (center), to produce a backscatter map (left). The bottom row of figures is analogous, with the exception of the differing irregularity structure. This suggests that the irregularities are either located along one wall or in the center. These plots are for one range gate, just as the plots in Figures 5.4a and 5.4b.

for 12 August 2005 using IRI 2007 [*Bilitza and Reinisch*, 2008] and NRL MSIS00-E [*Picone et al.*, 2002]. The estimated altitude exceeds that of the IRI/MSIS model. Tomographic reconstructions of plasma densities using the 135.6-nm airglow emission observed by the TIMED/GUVI instrument suggest that altitude of the peak electron density between depletions may reach as high as 425 km in the Pacific sector [*Comberiate et al.*, 2007]. Although the *Comberiate et al.* [2007] example was during the same season (22 September 2002), it was during near solar maximum conditions. *Sahai et al.* [2000] presented ionosonde data showing the F-region virtual height ($h'F$) exceeding 500 km during one night when spread-F was observed during solar minimum. Based on physical models of the emission emission profile, the 630.0-nm emission peak is typically about one neutral scale height (50–100 km) below the F-layer electron density peak. The estimated emission altitudes with this technique are therefore in line with *Comberiate et al.* [2007] and *Sahai et al.* [2000]. A more detailed correlative study with another instrument capable of estimating the airglow layer altitude would be compelling.

Furthermore, the night of 12 August 2005 is particularly active with depletions continuing throughout the entire night. The lowering (brightening in the airglow) of the ionosphere, usu-

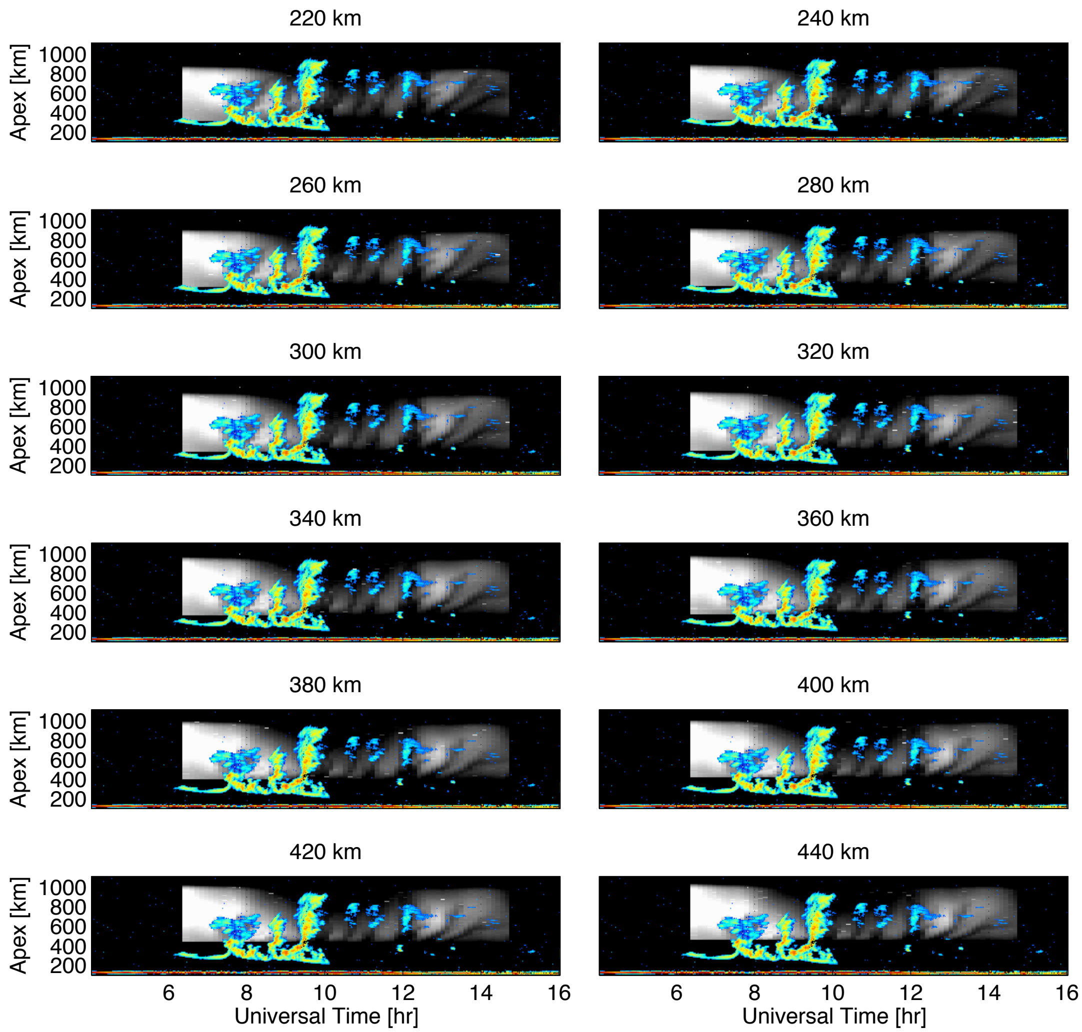

Figure 5.6: Series of RTI grams from 12 August 2005 produced with the assumed airglow emission altitude varied from 220 to 400 km. The height of the airglow layer does change as a function of time. At different times, different altitudes may match better. See text for detailed discussion.

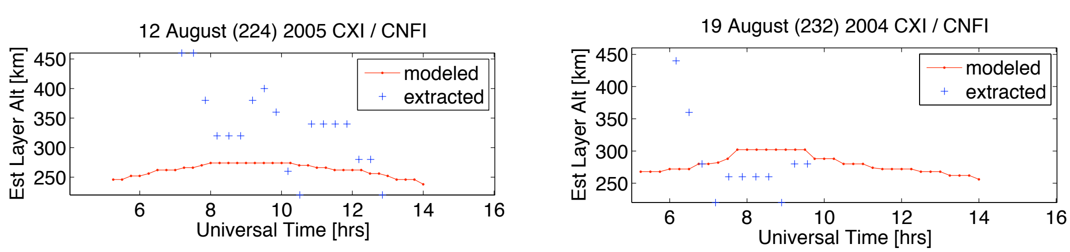

Figure 5.7: Automatically determined airglow peak emission altitude (in 20-km bins) compared with MSIS/IRI modeled emission altitude for 12 August 2005 and 19 August 2004, left to right, respectively.

ally associated with the MTM (midnight temperature maximum), occurs at 1300 UT, some three hours after local midnight. The combination of high depletion activity and late layer lowering may be related to drivers (e.g., tides, a vigorous $\mathbf{E} \times \mathbf{B}$ drift earlier in the day) that exceeded the physical or statistical basis for the models.

The remaining plots in Figure 5.7 illustrate another example, 19 August 2004 (RTI gram in Figure 5.1). The high-altitude estimate at the beginning of 19 August 2004 is probably not physical, although there is some mismatch in Figure 5.1 at that time. It appears to match quite well near 260 km the rest of the night. Apart from the IRI/MSIS model, a direct measurement of the density or emission profile would lend additional credibility to this technique.

5.4.3 Decaying backscatter

It has been theorized that the Bragg-scale irregularities responsible for coherent backscatter are due to a flute mode drift wave that is pumped by an additional irregularity [*Hysell and Farley*, 1996; *Saito et al.*, 2008]. In the absence of the pump mode, the drift wave irregularities will diffuse rapidly.

Referring to Figure 5.2, under quiet geomagnetic conditions on 26–28 August 2005, the late-night descent of the ionosphere (brightening of the airglow) appears to coincide with the cessation of 3-meter backscatter even though the depletions remain. This corroborates the argument of *Saito et al.* [2008] that the descent associated with the MTM is associated with dwindling backscatter. Based on the airglow-derived drifts, it is not entirely clear that the eastward drift approaches stationary until after the backscatter disappears, if at all. Furthermore, the example in Figure 5.1 from 19 August 2004 shows strong ($\sim$ 100 m/s) drifts even after the 3-m backscatter has ended. This example is also interesting because the backscatter disappears before any apparent descent of the ionosphere. There is, however, a descent on 20 August 2004 that appears weakly in the airglow around 1030 UT between the last two tall radar plumes.

Supposing that it is a gradient drift instability that drives the 3-meter backscatter, the variability seen here suggests that there may be a threshold in the drift velocity, almost certainly set by the eastward thermospheric neutral wind, that determines the cessation of backscatter. This may have particularly interesting implications for 12 August 2005, when high-altitude backscatter persists after low-altitude irregularities have disappeared. The small patch of backscatter at 400 km at 1200 UT on 12 August 2005 appears to be fairly well matched to the airglow, as seen in Figure 5.6. However, the backscatter above, presumably from the same depletion, is quite far from the depletion outline in the airglow, suggesting that the airglow layer might not have a uniform altitude across the image.

5.4.4 Climatology

Figure 5.3 illustrates the seasonal climatology of airglow depletions and 3-m backscatter observed from 2002 to 2009 by CNFI and CXI. This climatology extends and corroborates work by *Makela et al.* [2004], which was only performed for 2001–2003 using data from Maui. It is clear that the occurrence of airglow depletions and backscatter is seasonal and well-correlated. There is a peak in activity in the later portion of the year, particularly July–October, surrounding the autumnal equinox. There is considerably less activity at the vernal equinox, when the sunset terminator is also aligned with the geomagnetic declination in this longitude sector. This confirms that alignment may be a necessary, although insufficient, condition for irregularity growth [*Tsunoda et al.*, 1982]. The reason for this asymmetry is not yet known, although *Maruyama and Matuura* [1984] have suggested that it may be a consequence of the neutral wind. However, Fabry-Perot interferometer measurements of the neutral wind in the American sector by *Mendillo et al.* [2001] suggest that, at least during the time period considered, there is little direct correlation between the thermospheric neutral wind and the observation of GPS L_1 ($f_{L_1} = 1.57542$ GHz) radio scintillations and airglow depletions. More recently, *Su et al.* [2009] have used ROCSAT-1 satellite drift velocity measurements to infer that differences in irregularity formation morphology may be more strongly related to the onset and duration of vertical drifts (through their relationship to the local geomagnetic field intensity) during different seasons.

As discussed in the previous section, backscatter also decays before the depletions disappear. This is also quite clear from the climatological data as the depletions tend not to disappear until sunrise (top of the plots). Unlike previous studies using satellite in situ observations [*Huang et al.*, 2002] and airglow images [*Sahai et al.*, 2000], these data suggest that the equatorial ionosphere continues to produce irregularities into solar minimum at a rate comparable to that seen near solar maximum. However, there are marked differences in the morphology and behavior.

One notable effect is that the seasonal backscatter centroid appears later in the evening toward solar minimum. It is probable that these depletions go largely undetected by the sun-synchronous DMSP satellites because they occur late in the evening or early in the morning local time, and many do not reach the 840-km orbit altitude. Both 3-m backscatter and depletions appear to dwell longer at solar minimum in this data set as well. As discussed previously, the midnight temperature maximum, which often coincides with the cessation of backscatter, does not vary greatly in time or intensity as a function of solar cycle. Therefore, it is unlikely to be a source of variability with solar conditions.

As solar activity decreases, there is also an increase in early-morning backscatter activity in December–January. This effect is pronounced in 2005–2009 and only visible in the −10 dB category. These irregularities frequently coincide with activity in the airglow. Although statistics were not tracked independently for this study, many of the airglow structures observed at the end of the night in 2008 and 2009 resembled the southwestward propagating undulations often observed at Arecibo [e.g., *García*, 1999]. Although the electric fields within these structures are known to map into the conjugate hemisphere, they are not frequently associated with depletions or Bragg-scale irregularities [*Saito et al.*, 1995]. There have been some recent examples of VHF backscatter from these structures at middle latitudes by the MU radar [*Otsuka et al.*, 2009]. *Makela et al.* [2009] have argued with an example that under certain conditions, what may be a midlatitude phenomenon can induce backscatter near the geomagnetic equator. A similar event is shown in Figure 5.2 on 24 August 2005. A study of the anomalous peak in activity, as well as a proposed explanation involving forcing from mid-latitude MSTID instabilities, is presented in Chapter 6.

5.5 Conclusion

This work presents several interesting conclusions regarding the morphology of plasma depletions and VHF backscatter during the course of a solar cycle. In a long-term sense, this work confirms earlier point (space and time) observations suggesting that meter-scale coherent radar backscatter originates from within the depleted regions of equatorial plasma bubbles and presented examples showing the variety of conditions under which coherent radar echoes are observed and the capability of coincident airglow images to contextualize these events.

Over the period January 2002–January 2009, we presented a climatological reduction of the airglow images and radar data showing that depletion and backscatter activity do not decrease substantially from solar maximum to solar minimum in the central Pacific. However, as solar minimum conditions set in, backscatter begins later in the evening and continues longer. These observations confirm similar observations made from Jicamarca. One anomalous peak in backscatter and depletion activity has been noted in the November–January period of solar minimum years (November 2004–January 2009).

CHAPTER 6

EVIDENCE OF A MID-LATITUDE SEED FOR EQUATORIAL PLASMA DEPLETIONS

6.1 Introduction

As discussed in Chapters 1 and 2, irregularities in the post-sunset equatorial F-region ionosphere have been a source of immense scientific and engineering curiosity since their first reporting by *Booker and Wells* [1938]. Among the enduring unknowns regarding equatorial plasma depletions is the sequence of events linking their formation to the apparently unstructured equatorial ionosphere of the late afternoon. Although depletions tend to have a well-defined seasonal occurrence (July–October, March–May, for Hawaii [*Makela et al.*, 2004]) for a given longitude, the day-to-day variability remains elusive.

Within the depleted regions, polarization electric fields of sufficient scale map efficiently along the geomagnetic field pushing depleted wedges into low and tropical latitudes, piercing layers of airglow emission. Imaging observations of the 630.0-nm (dissociative recombination of O_2^+) airglow have been conducted from Hawaii since December 2001 [*Kelley et al.*, 2002]. These observations are supported by a 50-MHz radar on Christmas Island, Kiribati. On-going climatological study of airglow images and radar backscatter from these sites uncovered a minor peak in post-midnight depletion and backscatter activity in solar minimum years (2005–2009). Although post-midnight depletions are often associated with geomagnetic activity [*Martinis et al.*, 2005], these events almost universally occurred under quiet conditions, prompting this investigation. A similar pattern of post-midnight spread-F was also reported at Hawaii in the climatology by *Reber* [1954].

In addition to depletions, mesoscale traveling ionospheric disturbances (MSTIDs) are frequently observed in the 630.0-nm airglow emission over Hawaii, particularly during solar minimum conditions. The MSTID is a propagating perturbation in the altitude of the electron density peak thought to be related to the Perkins instability [*Perkins*, 1973]. MSTIDs appear propagating from the northeast to the southwest with wavefronts aligned in the southeast-northwest direction. Like depletions, MSTIDs contain polarization electric fields that map into the conjugate hemisphere [*Otsuka et al.*, 2004a]. However, meter-scale field-aligned irregularities (FAIs) responsible for coherent backscatter are confined to the undulations and are not generally observed at high altitudes [*Otsuka et al.*, 2009].

In this chapter, we examine observational evidence of a relationship between mid-latitude structure and the development of post-midnight equatorial spread-F during geomagnetic quiet conditions. We suggest that the polarization electric field associated with the mid-latitude structure maps to the bottom-size equatorial F region, initiating the development of plasma depletions, as proposed by *Tsunoda* [2007]. We will first give a brief overview of the instrumentation, which is amply discussed in Chapters 2, 3, and 5. Then, we will present two case study events followed by a discussion of the events and their potential implications for understanding the seeding of equatorial plasma depletions in general.

6.2 Instrumentation and Observations

The instrumentation employed in this study comprises two airglow imaging (CNFI and CASI) systems located atop Mount Haleakala and a 50-MHz radar at Christmas Island. These systems are described in Chapter 2. By tracing the ray paths from each pixel on the CCD imaging sensors in these systems to the airglow layer height, two-dimensional maps of the airglow emission extending from 5° N to 28° N latitude are produced. The radar east beam provides backscatter data slightly to the east of the CNFI field of view, while the north beam provides observations within the same geomagnetic volume as CNFI. That is, the range gate centroid locations of the north beam reside on geomagnetic field lines that intersect the airglow observed by CNFI north of the geomagnetic equator, as illustrated in Figure 2.15.

During cataloging of the images from Haleakala (reported in Chapter 5) from January 2002 to January 2009, a high incidence of MSTID structures was noted during the November–January period during the solar minimum years (from late 2005 onward). Furthermore, the radar climatology (also presented in Chapter 5) indicates a coincident increase in post-midnight backscatter. This correlation was not immediately apparent since separate statistics for MSTIDs and plasma depletions were not being kept. However, a few events provided impetus for further study. Of these, we have selected two examples to present here: 23 November (327) 2005 and 2 September (246) 2008. Both of these days are preceded by geomagnetically quiet conditions ($K_p < 3$), which is representative of all of the events in the dataset.

The first example, from 23 November 2005, is striking: it is near the end of the normal plasma bubble season for Hawaii, the airglow data are of high contrast, and the 50-MHz backscatter continues until the radar stops taking data. A composite data summary of this event is presented in Figure 6.1. The top of the figure contains header information about the date, site, and geomagnetic activity for ±5 days from the date of interest. The three panels summarize the airglow and radar data for the night, mapped to the field line apex for comparison using the International Geomagnetic Reference Field (IGRF) [*Maus et al.*, 2005]. The vertical scale is the apex altitude and the horizontal scale is Universal Time (leads Hawaiian Standard Time, HST, by 10 hours). The top panel is a keogram, except that each altitude bin at each time step corresponds to a range gate of the CXI radar's north beam. This permits direct comparison of the range-time-intensity (RTI) map from the radar with the airglow images, which are shown overlaid in the center panel. The dark bands (indicated by arrow) from upper left to lower right between 2300 and 0000 HST are the signature of an MSTID passing through the local ionosphere over Haleakala. The bottom panel provides an estimate of the eastward drift velocity of features in the airglow corresponding to different apex altitudes using the technique described in Chapter 5. The black regions indicate locations where no features were tracked. The regions marked with 'W' have westward drift components due to the MSTID.

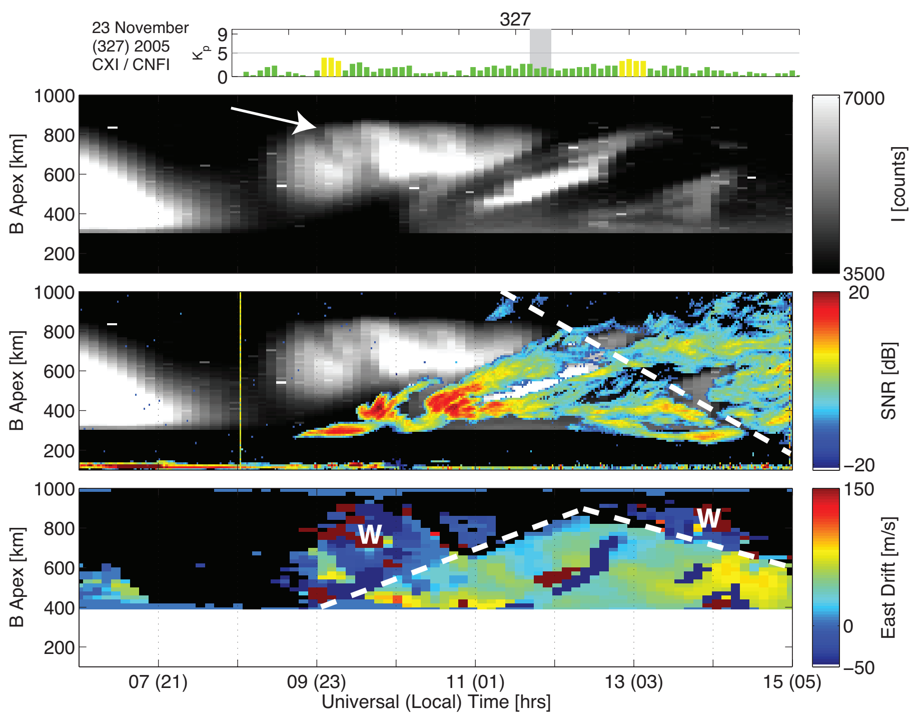

Figure 6.1: Data summary "RTI-gram" from 23 November (327) 2005. Headers show K_p index for ±5 days. The three panels contain (top) a keogram of the airglow, (middle) RTI-gram of the airglow and radar backscatter, and the plasma drift velocity estimated from features in the local airglow layer (bottom). See text for discussion.

Figure 6.2 illustrates the relationship between the light and dark bands of the MSTID structure and the Doppler velocities observed at the Christmas Island radar. Although it is not a perfect indicator of the electric field structure, the coherence of the Doppler velocity within the bands suggests that they are electrified and the polarization fields are driving the 3-meter irregularities by the $\mathbf{E} \times \mathbf{B}$ mechanism.

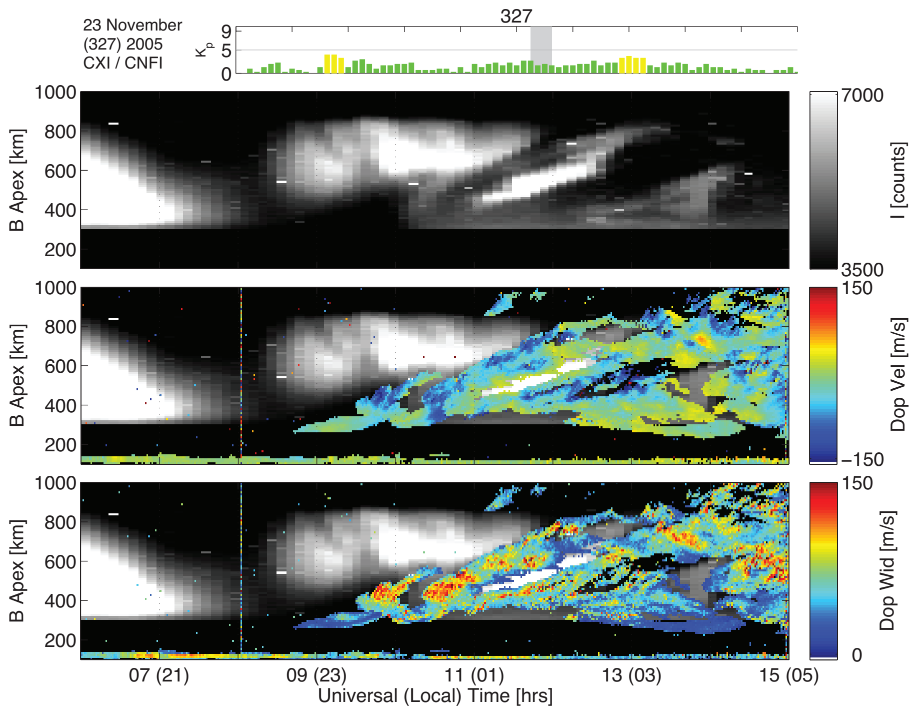

Figure 6.2: Supplemental RTI-gram plot similar to Figure 6.1 with Doppler velocities and widths from the Christmas Island radar. The light and dark bands of the MSTID structure correspond directly to downward and upward Doppler velocities, suggesting that the structure is electrified and driving $\mathbf{E} \times \mathbf{B}$ drifts. Broader widths imply more recent development of the irregularities.

Figure 6.3 contains eight selected airglow frames from CNFI and CASI on 23 November 2005. They ilustrate the appearance of a band structure propagating to the southwest as plasma bubbles appear at the equator and propagate to the east. The geomagnetic projections of the north and east beams of the Christmas Island radar along the flux tubes corresponding to each range gate are plotted as well. A large alternating band structure begins to appear in the all-sky images of the 630.0-nm emission around 2042 HST. The isointensity contours of the MSTID emerge in the airglow already elongated magnetically northwest to southeast and propagating to the southwest (about 50 degrees off magnetic north). At first, the bands appear to be a large wave. However, by 2153 HST, finer structure begins to appear in the circled region. By 2229 HST, the structure appears to reach all the way to the southern extent of CNFI's field of view. This is well-correlated with first

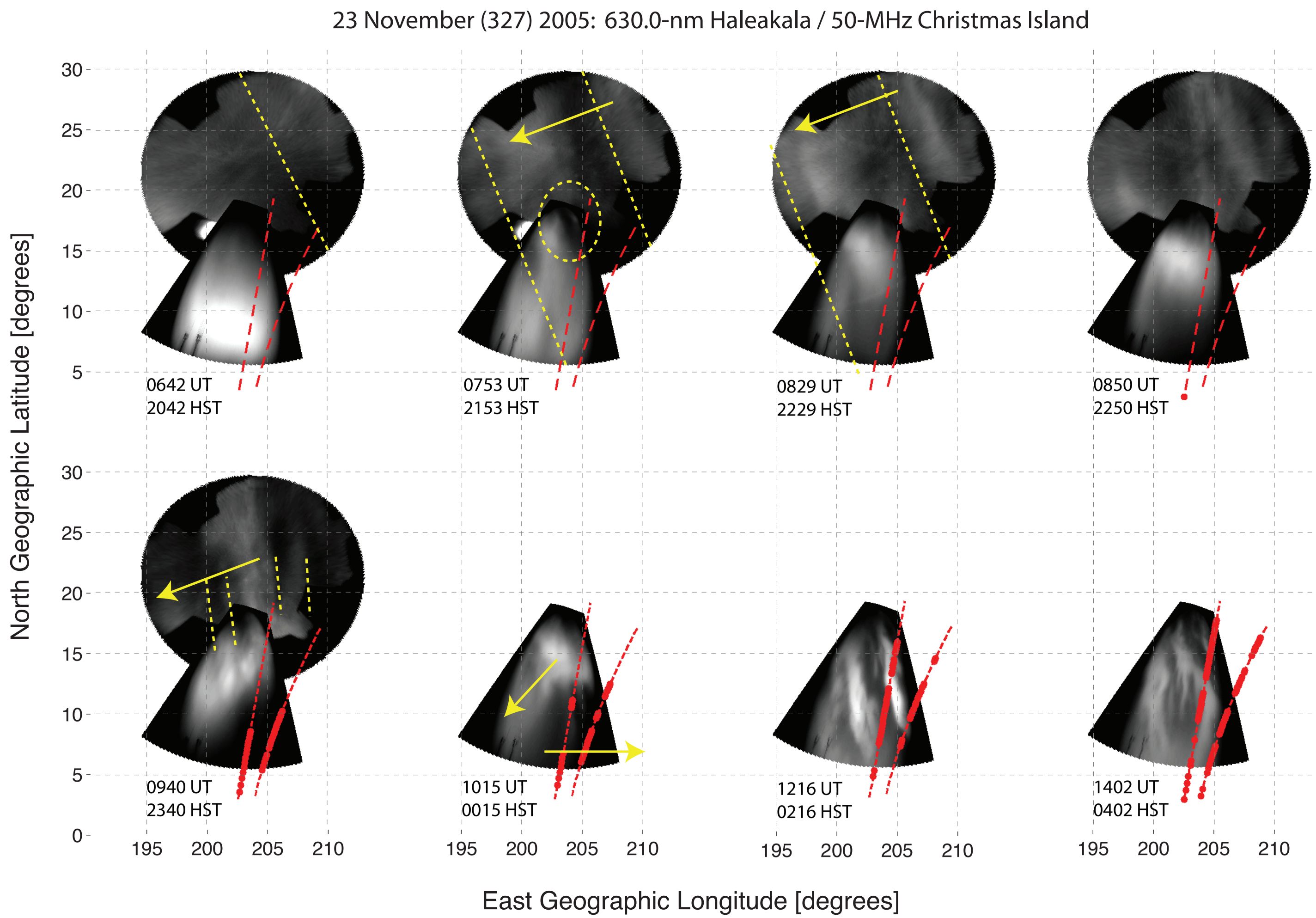

Figure 6.3: Selected airglow images from CNFI and CASI on 23 November (327) 2005. Images are projected to the airglow layer at (nominally) 250 km altitude. The north and east beams of the Christmas Island radar are also overlaid by mapping along the geomagnetic field. Dots appear on the beams when the received SNR is > -10 dB indicating FAI. Arrows coarsely indicate the motion of the structures.

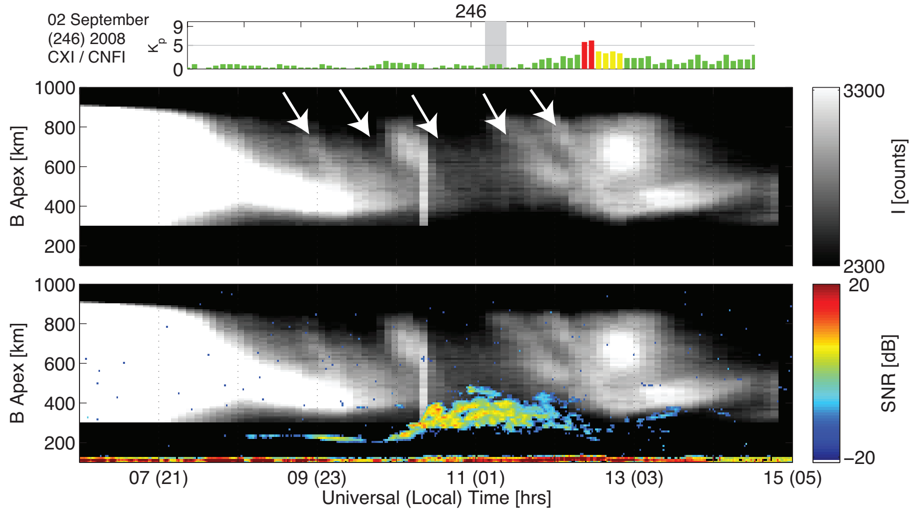

Figure 6.4: Data summary from 2 September (246) 2008. Same format as Figure 6.1 except there are no drifts.

radar echoes occurring at 2250 HST. Bubbles begin to emerge around the time of the last all-sky image at 2340 HST. The bubble-like features between 200° and 202° are actually propagating to the southwest with a wavelength of about 150 km. At 0015 HST, both the plasma bubbles drifting to the east and the MSTID drifting to the southwest are visible in the same image. The bubbles grow in altitude (and latitude) and continue to drift east throughout the remainder of the night.

In Figure 6.1, there appears to be a break in the backscatter, which is indicated by the dashed line in the center panel. This coincides with a shear in the drift velocity as the depletions grow into a region still affected by the MSTID instability. As the drift slows, secondary structures grow on the eastern walls of the depletions which are particularly evident in the 0216 HST frame from Figure 6.3.

Figure 6.4 illustrates the summary data for 2 September 2008. This night exhibits a bottom-type layer that formed at 2200 HST but did not yield any plumes before decaying around 2330 HST. In our experience, bottom-type layers never re-form after descending in altitude. This has also been confirmed by *Hysell and Burcham* [1998]. However, at 2345 HST, coincident to the passage of an MSTID in the airglow (indicated by arrows), a packet of depletions emerges along with the attendant backscatter. Although they are not evident in the keogram, these depletions are visible in the airglow frames (not shown). Most of the backscatter disappears in conjunction with the lowering (brightening of the 630.0-nm emission) of the ionosphere around 0300 HST.

6.3 Discussion

The event from 2 September 2008 is interesting because the MSTID structure continues in the airglow until the backscatter vanishes. This is in sharp contrast with the 23 November 2005 example in which the equatorial irregularities not only grow to high altitudes (latitudes), but the MSTID introduces a shear in the drift, apparently allowing the cascade to smaller-scale irregularities to continue until after the radar stopped collecting data at 0600 HST, which is 15 minutes before sunrise at the CXI site. Although it does not alter the distribution of irregularities, the descent of the ionosphere at 0300 HST on 2 September 2008 (Figure 6.4) appears to quench the cascade to smaller scales, corroborating the assertion of *Saito et al.* [2008].

Among the most compelling recent theories for the initiation of equatorial plasma depletions just after sunset is a fast-growing mode operating on perturbations with westward-tilting wavefronts (with maximum growth rate at 45°) in the equatorial plane put forth by *Kudeki et al.* [2007]. A polarization electric field $\mathbf{E_p}$ associated with an MSTID structure such as those at 2340 and 0015 HST in Figure 6.3 can drive an $\mathbf{E_p} \times \mathbf{B}$ drift with westward-tilting wavefronts when mapped to the equator. This relationship is illustrated in Figure 6.5.

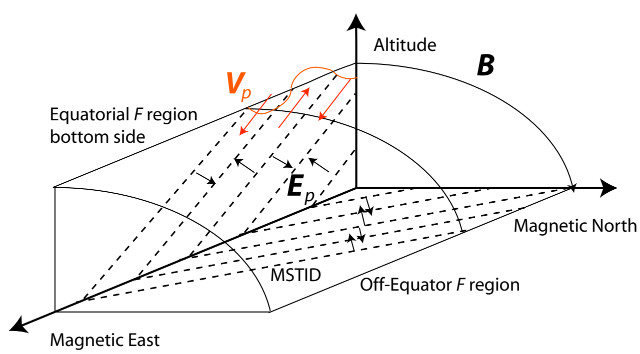

Figure 6.5: A schematic of polarization electric fields ($\mathbf{E}_p$) within a mid-latitude structure driving a perturbation (via $\mathbf{V}_p$) at the equator.

The (projected) length-scale presented here for 23 November 2005 differs from those suggested by *Kudeki et al.* [2007] as providing maximal growth in the post-sunset period (240 km versus 40 km). And, as *Kudeki et al.* [2007] point out, the collisional-shear instability presented by *Hysell and Kudeki* [2004] has a similar growth rate to the 240-km wind-driven instability. Although this particular instability may no longer operate due to the fact that the F-region dynamo constrains the neutrals and plasma to move at the same rate, the MSTID can generate vertical velocity perturbations on the order of 80 m/s, which are sufficient to destabilize the equatorial ionosphere. On 23 November

2005, the spacing of the depletions is identical to the projected wavelength (240 km $\times \cos 50° \approx$ 150 km, where 50° is the angle of MSTID propagation with respect to the magnetic equator) of the fine-scale MSTID bands indicated at 2340 HST in Figure 6.3, lending credence to this theory.

The principle contribution of this work is to illustrate that seeding of Rayleigh-Taylor instability responsible for the ultimate growth stage of equatorial plasma depletions need not be the sole providence of a particular process; rather, the title goes to the highest bidder. That is, the bottom-side F-region gradient is susceptible to the Rayleigh-Taylor instability for much of the night. In the hours just after sunset and during periods of peak depletion activity, irregularities growing out of the evening vortex region are the fastest-growing, and therefore most likely seeds. Later in the evening, when the ionospheric current system has approached steady state with the F-region dynamo firmly in control, perturbations may be created by electric fields mapped in from off-equatorial sources. There are at least a half-dozen more examples of coincident mid-latitude and equatorial events in the data from November and December 2008 alone. This suggests that these events may be quite common at solar minimum.

That depletions may be triggered by off-equator processes also underscores the practical importance of understanding the ionosphere at middle latitudes from a space weather perspective. Scintillations associated with equatorial plasma depletions have negative effects on the availability and accuracy of satellite-based communication and navigations systems. Users of these systems would benefit from enhanced prediction and mitigation schemes.

6.4 Conclusion

In this chapter, we have examined two examples of post-midnight equatorial plasma depletions initiated by polarization electric fields from a mid-latitude process mapped into the equatorial ionosphere, as suggested by *Tsunoda* [2007]. Airglow images in conjunction with VHF coherent backscatter provide a four-dimensional (three spatial, one temporal) picture of the initiation of many post-midnight equatorial plasma depletions observed during quiet periods.

CHAPTER 7

CONCLUSION AND FUTURE DIRECTIONS

7.1 Contribution

7.1.1 Data presentation and analysis

The primary aim of this work is to develop synergy between data sets from radio and optical instruments, leveraging their strengths and mitigating their weaknesses to understand the physical implications of the data. Radio instruments excel at providing high-resolution range data through phase-coherent detection. However, their coverage is generally limited to a narrow beam/ray region.[1] Airglow imaging provides considerable information on the two-dimensional (horizontal) spatial structure at ionospheric altitudes. However, it lacks information on the detailed irregularity structure and the range. Combination of data from imagers and radars permits the small-scale irregularities to be contextualized within the larger-scale structures. Combination of data from imagers and GPS occultation receivers can approximate the location of scintillation-causing irregularities in three dimensions.

7.1.2 Physics

Three physics contributions have been made in this work. The first is to establish the location of scintillation-causing regions in three dimensions using radio occultation and airglow imaging. The second contribution is the long-term climatology of equatorial plasma depletions and the associated backscatter in the central Pacific using airglow observations from Maui and coherent-scatter radar observations from Christmas Island. The third and perhaps most significant contribution is evidence of a mid-latitude seed for equatorial plasma depletions that occur post-midnight during quiet geomagnetic conditions at solar minimum.

During the course of the climatology created using airglow observations from Hawaii and backscatter from Christmas Island, an anomalous post-midnight peak in depletion/backscatter activity was

[1] Although this restriction has been relaxed considerably by the AMISR systems and radio tomography techniques, there is no significant AMISR installation at middle or equatorial latitudes and tomography requires sufficient instrument density, which is only recently coming to fruition for long-term observations.

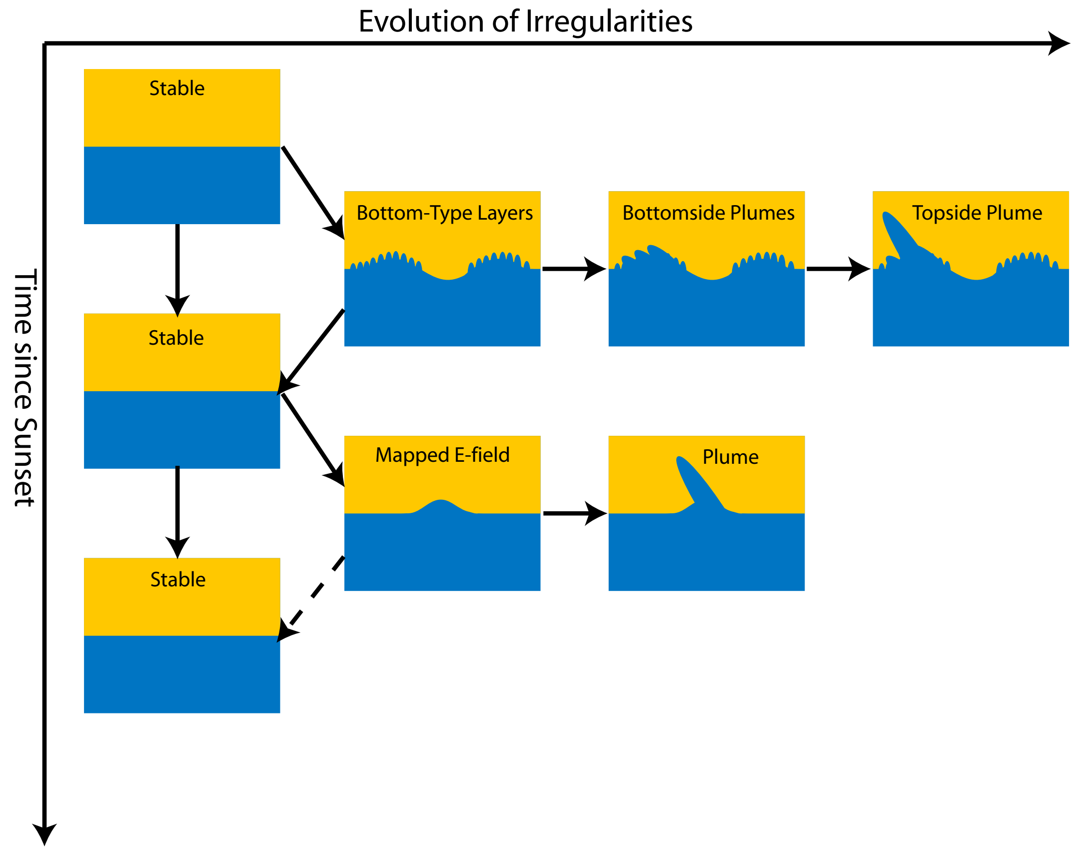

Figure 7.1: Flow-chart showing the interaction between potential seeding mechanisms for equatorial plasma depletions.

discovered during November–January during solar minimum. Further investigation yielded an interesting coincidence between mesoscale traveling ionospheric disturbances (MSTIDs) and the formation of depletions and backscatter post-midnight during geomagnetic quiet conditions. Polarization electric fields within the MSTIDs drive an $\mathbf{E} \times \mathbf{B}$ drift as the the fields are mapped to the geomagnetic equator. This suggests an alternate seeding method for equatorial plasma depletions by MSTID structures propagating to low-latitudes. Figure 7.1 illustrates the present post-sunset seeding theory along with the middle latitude seeding theory put forth in Chapter 6.

7.2 Future Directions

There are two primary areas where this work could be expanded, one in the physics, and the other in data processing. Although evidence of mid-latitude seeding of equatorial plasma depletions has been presented, it is mostly a by-product of the analysis techniques at this stage. A more-detailed description of the physics would be compelling, although it could perhaps form another dissertation in and of itself. The 2-D inverse-scattering solution for GPS radio occultation presented by *Sokolovskiy et al.* [2002] and discussed in Chapter 2 was not reproducible on coincident airglow observations discussed in Chapter 4 using standard quadrature integration techniques. This continues to be an area of potentially fruitful study because it would provide a complete picture of scintillation-causing irregularities.

7.2.1 Seeding of depletions

There are several more examples of coincidence between MSTID events and the appearance of equatorial plasma depletions in November and December of 2008. At least one of these examples, 29 November (334) 2008, coincides with the passage of the C/NOFS satellite in the vicinity of Maui and Christmas Island. CORISS radio occultation profiles for this event, depicted in Figures 7.2a–c, suggest considerable structure in the equatorial ionosphere at this time, including what may be E_s layers.

Each of Figures 7.2a–c exhibit negative n_e over a range of altitudes, particularly up to 200 km. This suggests a gross violation of spherical symmetry. Figure 7.2b not only shows structure apparently in the E region, it also has jagged structure along the topside portion of the profile. Although there is coherent backscatter, there is very little L_1 scintillation (not depicted here). This suggests that the structure may be the result of an MSTID structure possibly associated with an E-F coupled instability as suggested by *Cosgrove et al.* [2004]; *Otsuka et al.* [2009]. Further work on the geometry of the occultation, as well as complementary data sets from the ground and in situ, may aid complete identification of MSTID structures in radio occultation profiles.

Another important consideration is the growth rate of perturbations caused by electric fields mapped to the equator from MSTID structures. The differential velocity between the plasma drift and the neutral wind is an important contributor to the instability suggested by *Kudeki et al.* [2007]. Since the F-region dynamo should be in control of the equatorial ionospheric current system by local midnight, this differential velocity would be approximately zero. This suggests that there may be more to the mid-latitude seeding of depletions than simple $\mathbf{E}$ perturbations.

7.2.2 Inverse scattering and radio occultation

As mentioned previously, the work of *Sokolovskiy et al.* [2002] was not reproducible for comparison with the irregularity location technique presented in Chapter 4. In brief, this inverse scattering

(a) CORISS Radio Occultation Profile - prn 26 - 29 November 2008 - 1136 UT

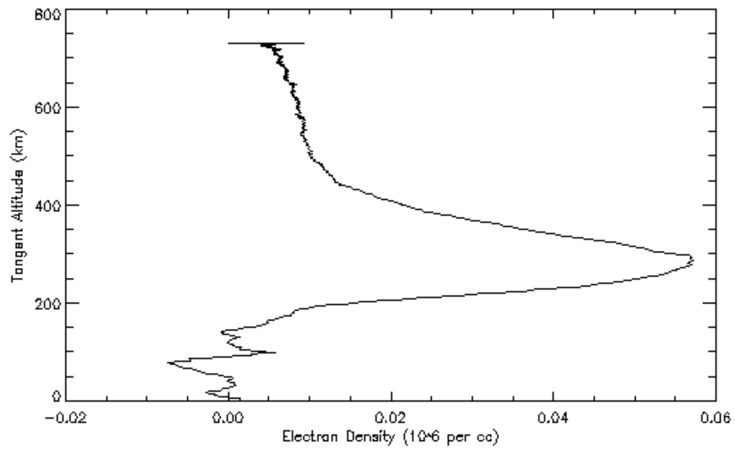

(b) CORISS Radio Occultation Profile - prn 12 - 29 November 2008 - 1317 UT

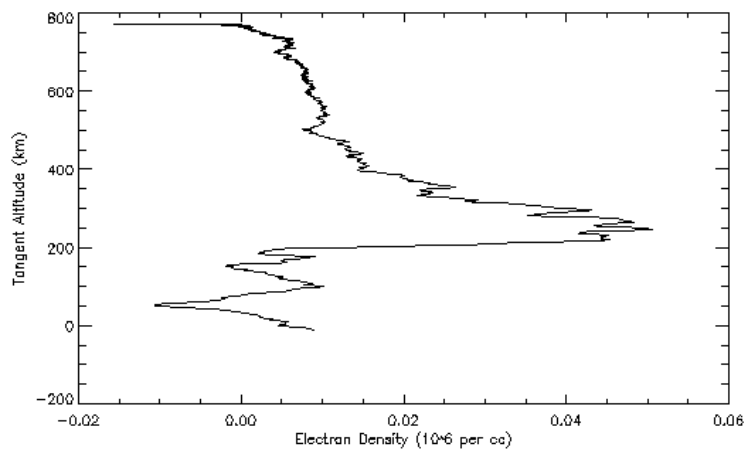

(c) CORISS Radio Occultation Profile - prn 9 - 29 November 2008 - 1321 UT

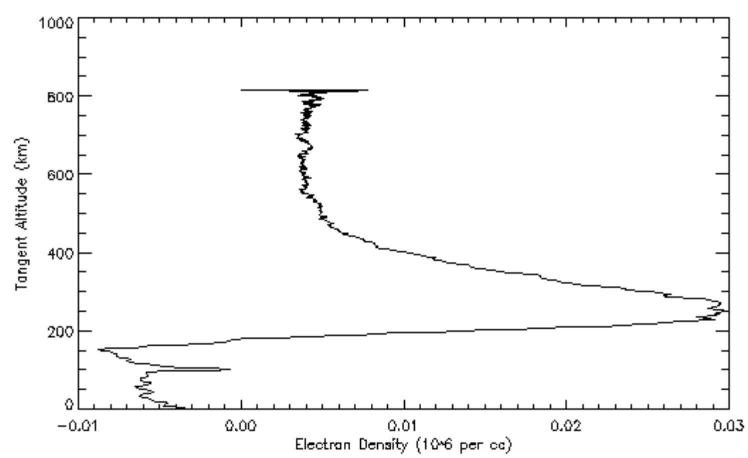

Figure 7.2: Three electron density profiles retrieved from C/NOFS Occultation Receiver for Ionospheric Sensing and Specification (CORISS) from the central Pacific on 29 November (334) 2008. These profiles were produced from the sub-orbital TEC assuming spherical symmetry. See text for discussion. Figures were provided by Rebecca Bishop and Paul Straus.

technique utilizes the SNR and excess phase data from radio occultation measurements to deduce samples of the complex field scattered by a thin phase screen. One of the principal errors was that any variation in the received signal amplitude or phase would result in the same solution for the phase screen location. That is, for a given orbit geometry and the projection into two-dimensions, any varying complex input signal produced the same phase-screen solution. However, employing the same technique with the two-dimensional modeled data in Chapter 2 was invertible for the phase screen locations. This suggests that the projection to two dimensions (from four—three spatial and one temporal) may have deleterious effects, particularly when the occultation is not particularly planar.

The scattering problem is quite computationally intensive, especially if a three-dimensional forward model was created to study the effects of projecting to fewer dimension to reduce computational complexity. One approximation that may be attractive has been presented by *Chaubell et al.* [2009].

Furthermore, few high-rate 50-Hz occultation examples exhibiting significant scintillation and significant common volume with the airglow imagers were available for comparison. This should be rectified with the continued success of the COSMIC/FORMOSAT-3 mission and the possibility for 50-Hz burst mode data on CORISS.

APPENDIX A

DATA MANAGEMENT WORKFLOW

A.1 Introduction

This work utilizes data from ground- and space-based airglow imaging systems, ground- and space-based GPS receivers, and radar systems, as well as models written in FORTRAN. In this chapter, I outline the workflow used to manage all of these data in a sensible manner.

A.2 Overview

Figure A.1 illustrates the flow of data. Incoming data transit our file server (`airglow`) as a point of entry. From there, they are archived and pushed off to other locations for analysis since the file server does not have sufficient resources to support many analysis sessions. I assembled an 8-node MOSIX cluster (`esf`) using surplus workstations from the dormitories for my analysis [*Barak et al.*, 1993]. The MOSIX environment simulates a symmetric multiprocessing system (SMP) similar to those supported by modern multi-core processors. This type of cluster is ideal because most of my analyses are codes that run relatively quickly on a small portion of the data set, but take a long time when analyzing the entire data set. The codes need not be specifically parallelized in the same sense that a large weather model might be for a supercomputer. Rather, multiple processes can be launched and the MOSIX scheduler simply migrates them from node to node for optimum performance.

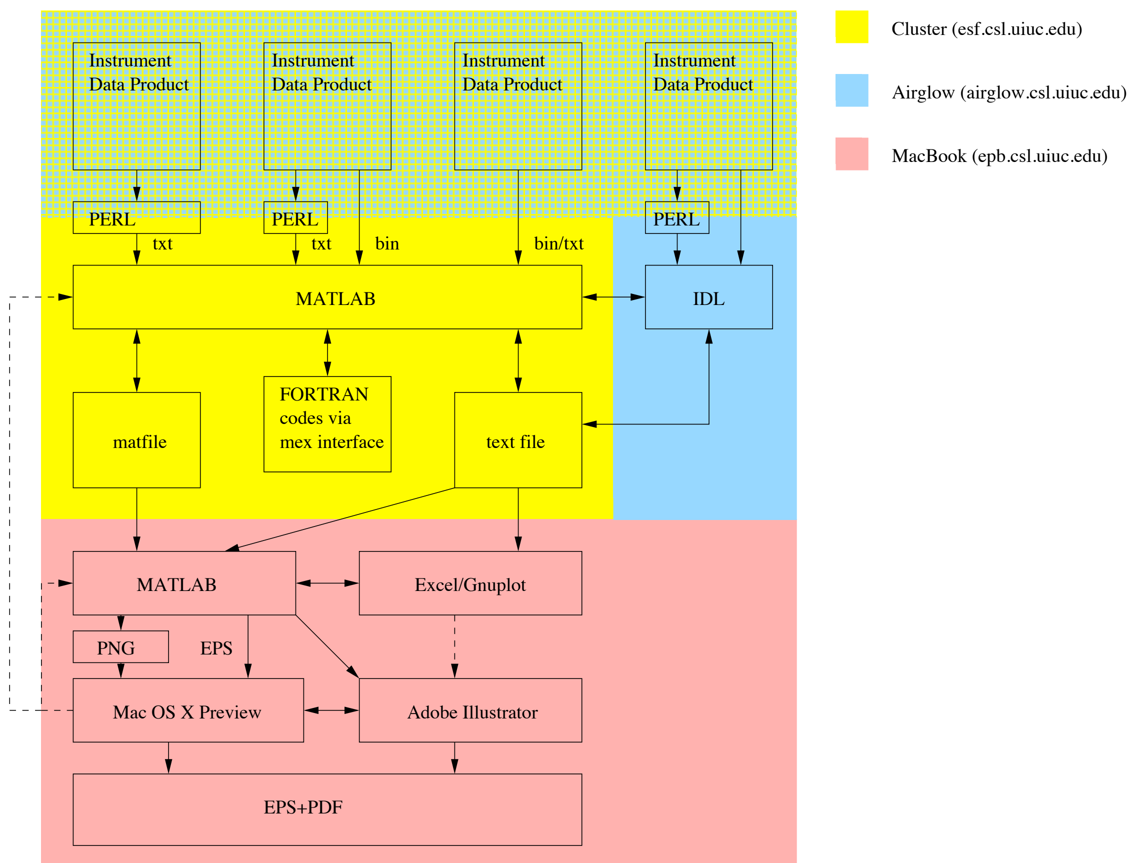

Figure A.1: Workflow developed to manage the data presented in this dissertation.

APPENDIX B

A CASE STUDY IN FIELDING INSTRUMENTATION

B.1 Introduction

The purpose of this appendix is to outline the process required to field instrumentation in a remote location. The instrumentation suite has already been selected: a dual-frequency GPS receiver and an all-sky airglow imaging system. Although the goal of the research at the Bonaire site is not directly related to this dissertation, it is an interesting case study because it was not conducted in conjunction with a university or another research organization. This introduced both challenges and opportunities. One aspect that will come up again and again is the power of knowing people. It is also instructive because, as of this writing, the system represents the state of the art in portable ionospheric observation. The following topics will be discussed: selecting the site, preparing the equipment and related hardware, transporting the instrumentation, and installation and data collection.

B.2 Site Selection

In the case at hand, the instruments needed to be located somewhere in the southwestern Caribbean since there was already a planned group of instruments in the southeastern Caribbean (Trinidad and Tobago). This left basically four choices: any of the three ABC (Aruba, Bonaire, Curaçao) islands of the Netherlands Antilles, or one of the coastal islands of Venezuela. Due to the stormy political situation between the U.S. and Venezuela, it was deemed unsuitable out-of-hand. West to east, Aruba, Curaçao, and Bonaire, each have very different character. Aruba is well known in the U.S. as a tourist destination and Curaçao is becoming more well known for tourism and as a center of commerce in the region. Bonaire is relatively lesser-known in the U.S. outside diving circles and has substantially lower population than the other two islands. Correspondingly, Bonaire is the most rural and has the least light pollution. The Bonaire community is also very eco-concious. In fact, the entire coastline of the island is a protected marine habitat. This suggested that it would be a good location.

There is one primary difficulty with Bonaire, as well: getting power. An initial visit to Bonaire made that clear. The best locations on the island do not have power available. I had some contacts among amateur radio operators who own homes on Bonaire, as well as several who visit there regularly (Hans van Hese, Noah Gottfried, Jeff Clarke, and Scott Robbins, personal communcation). These conversations suggested that most of the places with electricity would also have many lights. None of their properties were suitable for the installation. There was one option on a hill called Seru Largu in the northeast part of the island. Seru Largu hosts some of the communication (Telbo) and navigation (Antillean Coast Guard) equipment for the island and so would provide a nearby power drop. The Seru Largu location was accessible by road, as well, although it would require us to provide our own secure enclosure for the equipment. I pursued the idea of installing the equipment in a 20-foot sea container, which is readily available from Amcar Freight in Bonaire (Scott Robbins and Sue Felix, personal communication). The next step was to obtain a lease for the land.

In Bonaire, there are three types of land rights: outright ownership, short-least land, and long-lease land (Hans van Hese, personal communication). Most of the privately held land is in housing developments that are unsuitable for our instruments due to the surrounding light sources and other view obstructions. Short-lease land is difficult and expensive to obtain and tends to be used for business purposes. Long-lease land, however, was an attractive option: a few dollars per m^2 per year. Most of the hilltop at Seru Largu is long-lease land, so this would work. However, in preparation for a change in the administration of the Netherlands Antilles, the land office was being audited. There were so many poorly documented or undocumented land transfers that the process was held up at least two years for new applicants (Scott Robbins and Hans van Hese, personal communication). This suggested that an alternative would be attractive.

We started working another angle: find the most suitable site capable of alternative power. Two sites that I had driven past but not contacted were a butterfly farm and the Bonaire Washington-Slagbaai National Park (part of the Antillean national park system STINAPA). The butterfly farm was not responsive. The Washington-Slagbaai staff were not keen on the idea of installing the instruments and related power generation equipment on Park land. However, Fernando Simal (personal communication), the manager of the Park, put us in contact with several individuals who own property in the rural parts of the island. The most receptive of these were Alan Gross and Jane Townsend, who own about 30 acres in the Bolivia region of eastern Bonaire. Figure B.1 illustrates the location of the prospective sites.

Figure B.1: Composite satellite photograph of Bonaire showing the proposed instrument locations. The site marked “Alan and Jane” was the final location for installation.

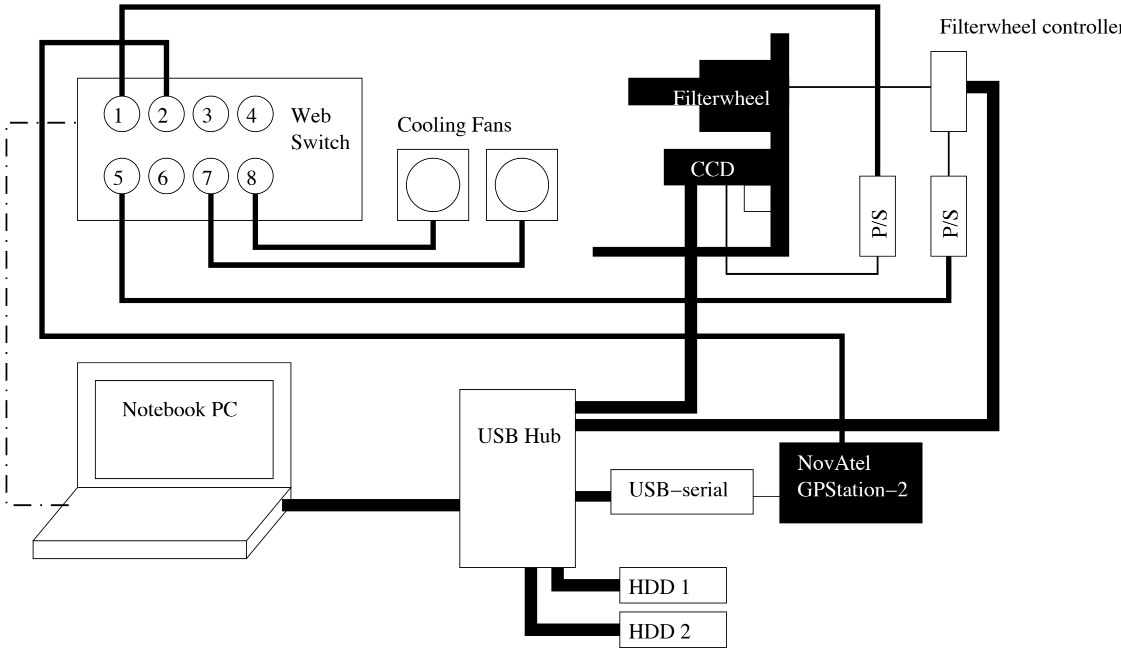

Figure B.2: Schematic of the complete instrument package installed in Bonaire.

Alan and Jane's entire homestead is powered by solar electricity. Initial measurements of the PICASSO (S/N A2) imager system with an SBIG CCD, the IBM ThinkPad R60 notebook computer, and the modified NovAtel GPStation-2 receiver, yielded a power requirement of about 80 watts during the night and around 40 watts during the day when the CCD was switched off. This exceeded the projected capacity of the present system. In order to support the additional load, a Whisper 200 wind generator was installed[1] prior to the installation of the equipment.

B.3 Equipment Preparation

The center of the instrument package is a notebook computer running a GNU/Linux operating system. This system controls the instruments and collects the data. The imager CCD and filterwheel are controlled via USB interface by CDAS (camera data acquisition software) written by Jonathan Makela. The GPS receiver is controlled by GPS-SCINDA software from Atmospheric and Environmental Research (AER). Scheduling is handled by the `cron` daemon and CDAS. Figure B.2 shows a schematic of the complete system with all components. A hard plastic toolbox serves as a convenient and readily available housing when a 12-inch acrylic optical dome is installed in the lid, as shown in Figure B.3.

[1]The logistical saga surrounding the purchase, installation, and ownership of the wind generator is not discussed here.

Figure B.3: Photograph of the inside of the equipment housing.

When this set of instruments was originally installed in Socorro, NM, Fedora Core 1 GNU/Linux (2.4 kernel, released in 2003) was installed for compatibility with the Finger Lakes Instruments filterwheel. Since both the Santa Barbara Instrument Group (SBIG) and Finger Lakes Instruments (FLI) had released new software for their products, and for compatibility with the USB to RS-232 convertor used by the GPS, it was decided to move to a more modern 2.6-series Linux kernel. The Xubuntu 8.04.1 LTS GNU/Linux distribution was selected for this installation because it offers long-term binary support, low graphical overhead, and an easy-to-use interface. The specific details of the software installation are chronicled electronically with the CDAS software.

The USB interface in the SBIG CCD requires firmware to be downloaded into it every time the power is cycled. This is accomplished through the Linux `udev` system, which allows system commands to be executed on hot-plug events. Both the CCD and the filterwheel are configured to be accessible to unprivileged users by `udev`, as well. All of the USB devices are connected by way of a powered USB hub. The powered hub also allows two external hard drives which are powered via USB to be attached to the bus without exceeding the power capacity. These drives are configured to automount and are synchronized daily by `rsync`.

As illustrated in Figure B.2, power is distributed using a Digital Loggers web power switch. This device has eight power outlets that are switchable through an embedded world-wide web server. For the purpose of automation, a Perl script on the computer automatically connects to the web server to switch outlets ON and OFF. This allows the CCD and filterwheel to be turned OFF during the

Table B.1: List of Tools and General Consumables Required for PICASSO/GPS Installation

Tool	Application
Leatherman Tool	General
Digital multimeter	Electronic and electrical troubleshooting
Solder iron and solder	Electronic repairs and modifications
Hacksaw blades	Cutting holes for dome, cables, and ventillation
Cordless drill and bits*	Drilling holes and driving screws
Interchangeable screwdriver*	Driving screws, prying, bits fit in drill
Wrench* (4- or 6-inch adjustable)	Tightening machine nuts
Hex wrenches	Imager adjustments
Flashlight	Finding your way in the dark
8-32 stainless machine screws	Mounting dome and electrical box
#6 drywall screws	Securing wooden shelf
1/4-inch Tapcon® screws	Mounting instruments to concrete
1/4-20 hex bolts	Mounting housing to pylons
Unistrut pylons	Mounting housing above concrete surface
1/4- x 1-inch fender washers	Tapcon screws and Unistrut mounting
Cauk dispenser† and silicone cauk†	Sealing the dome and other joints
11-inch Ty-wraps	Anchoring cables, fans, etc
Electrical tape	UV-/weather-proofing, masking, general
Heavy-duty hook and loop fastener	sticking small peripherals to the walls of the enclosure
Duct tape	General
Permanent marker	General

*Items were provided by host in Bonaire.
†Items were purchased on-site in Bonaire.

day to conserve electricity. Two fans are installed to move air through the enclosure for 5 minutes every 15 minutes.

Table B.1 lists basic tools and consumables used in the installation of the imager and GPS. The local availability and quality of these items varies dramatically from place to place. It is, therefore, wise to ship these items ahead of time. It is also beneficial to mark the circular hole for the dome with a compass before the box is transported into the field. White paint or correction fluid usually suffices in this application.

The final important step before shipping an imaging system is to determine and set the focus point in the laboratory. This is accomplished by coupling a tungsten light source into a single-mode fiber optic cable and focusing the camera on the spot of light at the unterminated end of the fiber. Introducing the dome into the optical path slightly perturbs the focus point on a PICASSO imaging system. Therefore, it is important to perform the focusing with the dome in-line as well as without. The focal point with the dome in-line is recorded and the focusing stage locked with a hex wrench for transport.

B.4 Transportation

The PICASSO system moves in two packages. One is the primary container, a Pelican 0350 flight case, which contains the instrumentation and computer. The second package serves as the housing and contains the GPS antenna and mast, the optical dome, and miscellaneous hardware that may or may not be available at the destination. Ordinarily, when working with a host institution, it is a simple matter to ship all of the equipment and the host will either provide a customs broker (as was the case with the instruments installed at Cerro Tololo, Chile) or negotiate directly with Customs (as was the case with the Trinidad and Tobago installation that complimented the Bonaire instruments). We did not wish to be in the position of paying a high duty or "fast money" as has been done in Brazil [*Ledvina*, 2004]. The Bonaire Customs procedures are not uniform, although they tend to protect locally produced goods (Alan Gross, Hans van Hese, Geoff Howard, personal communication). At the suggestion of Alan Gross (personal communication), we decided to secure a *carnet* (essentially, a merchandise passport) for the equipment. This was confirmed by Mr. Ludwig Balentien of the Customs office in Bonaire (personal communication). Most standard international courier services such as FedEx and UPS do not allow the use of carnets. So, the main container of instruments would be transported as checked baggage. Only the container of hardware was shipped by courier. At this writing, FedEx has the most reliable international logistics model of any courier, using local subcontractors to navigate the delivery-end environment (Dan Jordan, personal communication). This was confirmed by Alan Gross. The package arrived in Curaçao less than 24 hours after it was picked up; however, it took a week to get to Bonaire.

The carnet was straightforward to obtain from the U. S. Council for International Business. It cost about 500 USD and took two business days to arrive with standard processing. The carnet must be validated by U. S. Customs at the port of exit. This is important. I tried to do this before my port of exit and was refused. The validation process only takes about 20 minutes once the equipment is in the Customs area. When checking in for the departure flight, tell the airline representative that you would like to claim the containers covered by the carnet at the port of exit because it needs to clear Customs leaving the U.S. If baggage porters are available, they are worth whatever you pay them to get you to the Customs area, which may or may not be readily accessible from the insecure zone of the airport. You should not have to pay the excess baggage fee again if you are continuing on the same airline under the original itinerary. The Customs officer in Bonaire immediately spotted the flight case and demanded an explanation. When I produced the carnet document with a U. S. Customs seal on it, he was instantly satisfied and waved me through. This may or may not be representative of other countries.

B.5 Installation

B.5.1 Overview

No installation is typical. However, a typical plan of attack follows:

- Survey the site visually for light sources and view obstructions.
- Select the best position for the instruments.
- Assess needed supplies and (optionally) obtain them from a hardware store.
- Prepare the instrument housing by cutting holes for:
  - Dome
  - Cable inlet (mount an outdoor electrical box on the surface of the enclosure)
  - Ventillation (cover holes with fine fiberglas/plastic mesh)
- Install shelves for imager and computer, studs for web power switch.
- Install dome, fans, and electrical box.
- Seal dome and electrical box with silicone caulk.
- Mount instrument housing (see discussion following this plan).
- Connect and install instruments within the housing.
- Assess image quality:
  - Focus
  - Light pollution
  - Dark noise
- Operate the system for a period of nights.
- Train local host on maintenance and data transport.

B.5.2 Specific details

Although much of the installation of airglow imagers and GPS receivers is fairly obvious, there are some local idiosyncrasies that may complicate things. This section details how to work with concrete construction, UV radiation, and salt air.

In most of the tropical and equatorial regions, concrete construction is common. In Bonaire, the site was on top of a concrete above-ground septic tank. The GPS antenna and equipment enclosure were installed using Tapcon® concrete screws. These screws are very easy to install: drill a pilot hole with the provided concrete bit, then insert the screw. In order to make the instrument enclosure easy to install and keep it above the surface of the concrete for airflow and moisture ingress considerations, it was mounted on four pylons made of Unistrut channel that were anchored to the concrete, as shown in Figure B.4. These pylons also allow the enclosure to be removed from the concrete without drilling additional holes.

Protection from UV radiation is necessary, particularly for power cables. Our host, Alan Gross, provided some scraps of plastic irrigation tubing to use as conduits. Most varieties of Ty-wraps will disintegrate, as well. This can be prevented by wrapping them with good quality (3M Scotch® Super 33+) electrical tape (Geoff Howard, personal communication). Amateur radio operators who own and maintain stations in the Caribbean are a valuable source of information about UV protection and salt-air corrosion mitigation (e.g., `http://www.pj2t.org/`).

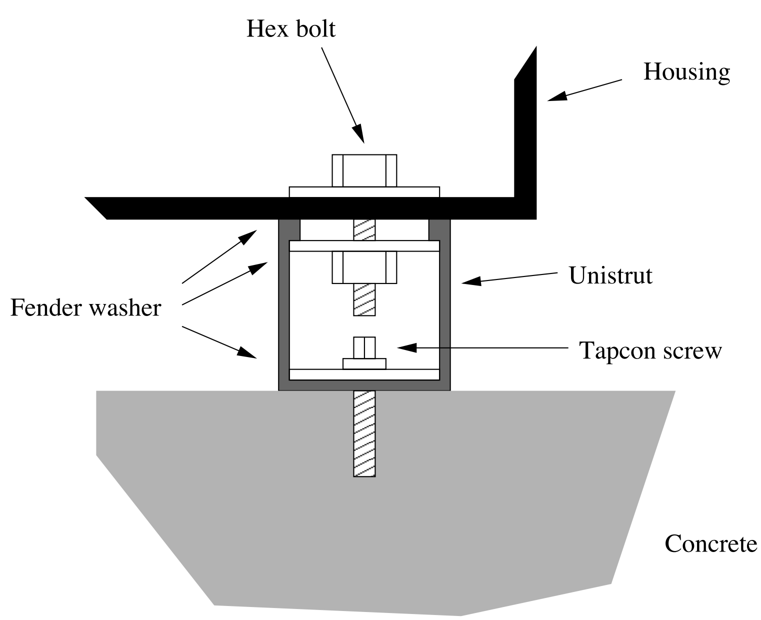

Figure B.4: Cross-sectional view of the Unistrut pylon arrangement.

B.6 After the Installation

There are two main tasks once the instruments have been installed and determined working: getting the data and ensuring that the instruments are maintained. In the case of the imager/GPS instruments in both Bonaire (miniature hard drives) and Trinidad (DVD+R), the data are sent back at regular intervals by courier service. The instruments on Mount Haleakala, Hawaii, and Cerro Tololo, Chile, are connected to high-speed Internet links. Maintenance can be a considerable headache, particularly when the computers are not connected to the Internet. Mobile telephone and video conferencing over a mobile Internet connection has worked relatively well in Trinidad. We have no experience with Bonaire, as of this writing.

APPENDIX C

GEOMAGNETIC FIELD MODELS

C.1 Introduction

As discussed in Chapter 3, electric fields of a certain scale map efficiently along the geomagnetic field. In order to effectively extrude electrified structures from airglow images, it is necessary to utilize a geomagnetic field model. There are two models in use for this type of work: the Altitude Adjusted, Corrected, Geomagnetic (AACGM) coordinate system [*Baker and Wing*, 1989] and the International Geomagnetic Reference Field (IGRF) [*Maus et al.*, 2005].

AACGM was primarily designed for high-latitude work as a part of the SuperDARN radar project. It gives each geomagnetic field line a unique latitude-longitude pair. Although questions have been raised in the past about the efficacy of AACGM at equatorial latitudes, the field coefficients of AACGM are no longer actively maintained. IGRF aims to be an accurate specification of the geomagnetic field and its variation with time. This goal is subtly different from AACGM: IGRF requires the field line to be traced in order to find points on the same field line. In this appendix, we briefly explore the relative errors involved in using AACGM versus IGRF as well as changing step sizes for tracing along the field line.

C.2 Step Size Study

In order to trace a field line, an initial point (δ, λ, z), a step size, step direction (via the sign of the step size), and the stopping altitude are provided. IGRF provides the magnetic field direction. The next point is determined by creating a segment of the length of the step size in the direction of the field. This process is iterated until the stopping altitude is reached.

Figure C.1 compares the absolute error with respect to a standard 100-m step size for the case of mapping the CXI north beam range gate centroids to the airglow layer at 250 km. The choice of 100 m was largely arbitrary and dictated by computation time. At the equator, one degree of longitude is approximately equal to 111 km. One degree in latitude is approximately the same at the equator and drops to about 100 km at 25° latitude. Clearly, the largest errors are in latitude. However, they only reach 25 km in the worst presented case (50 km steps) and 5 km in the second-worst case. For the purpose of this dissertation, a step size of 1 km has been used with the CXI beams.

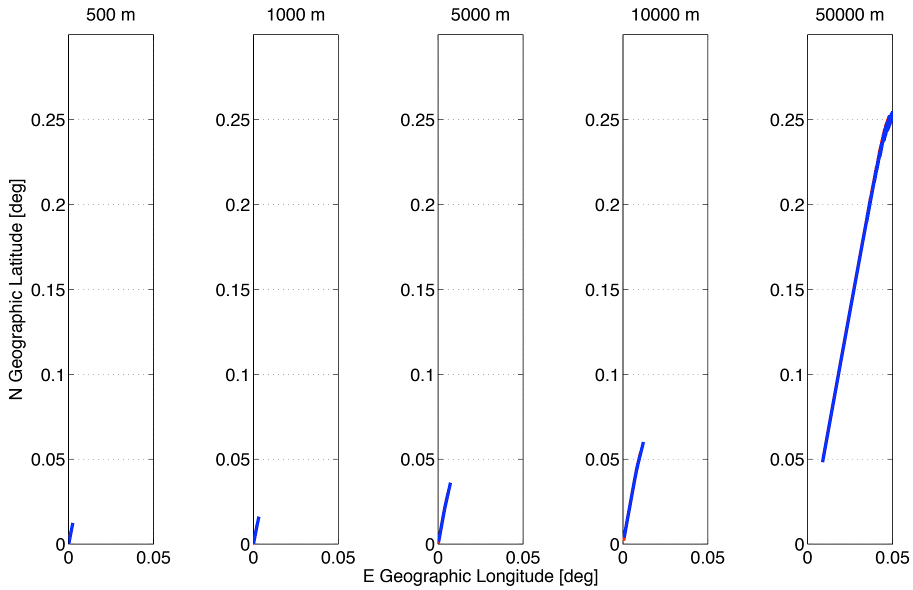

Figure C.1: Comparison of the error with respect to 100-m step size for steps of 500 m, 1 km, 5 km, 10 km, and 50 km, when mapping CXI north beam range gates to 250 km.

C.3 IGRF vs AACGM

This section highlights the absolute error between AACGM and the 100-m step IGRF trace used in the previous section. For comparison, the range gate centroids of the CXI north beam were converted from geographic coordinates to AACGM. The resulting magnetic coordinates were converted back to geographic coordinates using a fixed altitude of 250 km, again the nominal location of the airglow layer. The latest AACGM epoch 2000 coordinates are compared to IGRF in 2005, which is representative of the application in this dissertation.

Figure C.2 illustrates that the AACGM error is quite large, on the order of 25 km at some points. However, AACGM is much faster than IGRF, so this error has been tolerated with some of the airglow image maps, which have on the order of $10^3\times$ more points, in the interest of reduced computational complexity. An adaptive IGRF tracing function might be beneficial to expedite this.

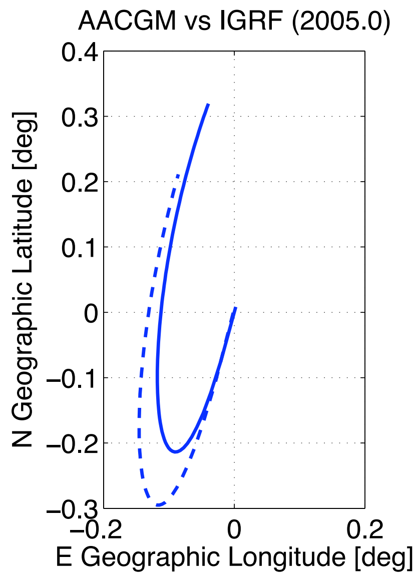

Figure C.2: Comparison of the error with respect to IGRF tracing with 100-m step size to AACGM, when mapping CXI east (solid curve) and north (dashed curve) beam range gates to 250 km.

REFERENCES

Aarons, J., J. P. Mullen, H. E. Whitney, and E. M. MacKenzie, The Dynamics of Equatorial Irregularity Patch Formation, Motion, and Decay, *J. Geophys. Res.*, *85*(A1), 139–149, 1980.

Anderson, P. C., and P. R. Straus, Magnetic field orientation control of GPS occultation observations of equatorial scintillation, *Geophys. Res. Lett.*, *32*, L21107, doi:10.1029/2005GL023781, 2005.

Atkinson, I., F. Kamalabadi, S. Mohan, and D. L. Jones, Asymptotically optimal blind estimation of multichannel images, *IEEE Trans. Imag. Proc.*, *15*(4), 992–1007, 2006.

Austen, J. R., S. J. Franke, and C. H. Liu, Ionospheric imaging using computerized tomography, *Radio Sci.*, *23*, 299–307, 1988.

Baker, K. B., and S. Wing, A new magnetic coordinate system for conjugate studies at high latitudes., *J. Geophys. Res.*, *94*(A7), 9139–9143, 1989.

Barak, A., S. Guday, and R. Wheeler, *The MOSIX Distributed Operating System: Load Balancing for UNIX*, *Lecture Notes in Computer Science*, vol. 672 pp., Springer-Verlag, Berlin, 1993.

Basu, S., S. Basu, J. Aarons, J. P. McClure, and M. D. Cousins, On the coexistence of kilometer- and meter-scale irregularities in the night-time equatorial F region, *J. Geophys. Res.*, *83*, 4219–4226, 1978.

Basu, S., S. Basu, J. D. Huba, J. Krall, S. E. McDonald, J. J. Makela, E. S. Miller, S. Ray, and K. M. Groves, Day-to-day variability of the equatorial ionization anomaly and scintillations at dusk observed by GUVI and modeling by SAMI3, *J. Geophys. Res.*, *114*, A04302, doi: 10.1029/2008JA013899, 2009.

Basu, S., et al., Scintillations, plasma drifts, and neutral winds in the equatorial ionosphere after sunset, *J. Geophys. Res.*, *101*(A12), 26,795–26,809, 1996.

Batista, I. S., and M. A. Abdu, Ionospheric variability at Brazilian low and quatorial latitudes: comparison between observations and IRI model, *Adv. Space Res.*, *34*, 1894–1900, doi: 10.1016/j.asr.2004.04.012, 2004.

Beach, T. L., and P. M. Kintner, Development and use of GPS ionospheric scintillation monitor, *IEEE Trans. Geoscience and Rem. Sens.*, *39*(5), 918–928, 2001.

Berkner, L. V., and H. W. Wells, Abnormal ionization of the E region of the ionosphere, *Terr. Magn. Atmos. Elec.*, *43*, 73, 1937.

Bernhardt, P. A., and C. A. Siefring, New satellite-based systems for ionospheric tomography and scintillation region imaging, *Radio Sci.*, *41*, RS5S23, doi:10.1029/2005RS003360, 2006.

Bhattacharyya, A., S. Basu, K. M. Groves, C. E. Valladares, and R. Sheehan, Dynamics of equatorial F region irregularities from spaced receiver scintillation observations, *Geophys. Res. Lett.*, *28*(1), 119–122, 2001.

Bilitza, D., International reference ionosphere 2000, *Radio Sci.*, *36*(2), 261–275, 2001.

Bilitza, D., and B. Reinisch, International reference ionosphere 2007: Improvements and new parameters, *J. Adv. Space Res.*, *42*(4), 599–609, doi:10.1016/j.asr.2007.07.048, 2008.

Bojarski, N. N., A survey of the near-field far-field inverse scattering inverse source integral equation, *IEEE Trans. Antennas and Prop.*, *AP-30*(5), 975–979, 1982.

Booker, H. G., and H. W. Wells, Scattering of radio waves by the F-region of the ionosphere, *J. Geophys. Res.*, *43*, 249–256, 1938.

Bowles, K. L., Observation of vertical-incidence scatter from the ionosphere at 41 Mc/sec, *Phys. Rev. Lett.*, *1*(12), 454–455, 1958.

Bowles, K. L., R. Cohen, G. R. Ochs, and B. B. Balsley, Radio echoes from field-aligned ionization above the magnetic equator and their resemblence to auroral echoes, *J. Geophys. Res.*, *65*(6), 1853–1855, 1960.

Breit, G., and M. A. Tuve, A radio method of estimating the height of the conducting layer, *Nature*, *116*, 357, 1925.

Cerruti, A. P., B. M. Ledvina, and P. M. Kintner, Scattering height estimation using scintillating Wide Area Augmentation System/Satellite Based Augmentation System and GPS satellite signals, *Radio Sci.*, *41*, RS6S26, doi:10.1029/2005RS003360, 2006.

Chaubell, J., O. P. Bruno, and C. O. Ao, Evaluation of EM-wave propagation in fully three-dimensional atmospheric refractive index distributions, *Radio Sci.*, *44*, RS1012, doi:10.1029/2008RS003882, 2009.

Cheng, C.-Z. F., Y.-H. Kuo, R. A. Anthes, and L. Wu, Satellite constellation monitors global and space weather, *Eos Trans. AGU*, *87*(17), 166, 2006.

Christensen, A. B., et al., Initial observations with the Global Ultraviolet Imager (GUVI) in the NASA TIMED satellite mission, *J. Geophys. Res.*, *108*(A12), 1451, doi:10.1029/2003JA009918, 2003.

Comberiate, J. M., F. Kamalabadi, and L. J. Paxton, A tomographic model for ionospheric imaging with the Global Ultraviolet Imager, *Radio Sci.*, *42*, RS2011, doi:10.1029/2005RS003348, 2007.

Cosgrove, R. B., R. T. Tsunoda, S. Fukao, and M. Yamamoto, Coupling of the Perkins instability and the sporadic E layer instability derived from physical arguments, *J. Geophys. Res.*, *109*, A06301, doi:10.1029/2003JA010295, 2004.

Daubechies, I., *Ten Lectures on Wavelets* pp., SIAM, Philadelphia, PA, 1992.

DeMajistre, R., L. J. Paxton, D. Morrison, J.-H. Yee, L. P. Goncharenko, and A. B. Christensen, Retrievals of nighttime electron density from Thermosphere Ionosphere Mesosphere Energetics and Dynamics (TIMED) mission Global Ultraviolet Imager (GUVI) measurements, *J. Geophys. Res.*, *109*, A05305, doi:10.1029/2003JA010296, 2004.

Drob, D. P., et al., An empirical model of the Earth's horizontal wind fields: HWM07, *J. Geophys. Res.*, *113*, A12304, doi:10.1029/2008JA013668, 2008.

Dungey, J. W., Convective diffusion in the equatorial F-region, *J. Atmos. Terr. Phys.*, *9*(5-6), 304–310, 1956.

Eccles, J. V., Modeling investigation of the evening prereversal enhancement of the zonal electric field in the equatorial ionosphere, *J. Geophys. Res.*, *103*(A11), 26,709–26,719, 1998.

Elsmore, B., Radio observations of the lunar atmosphere, *Phil. Mag.*, pp. 1040–1046, 1957.

Elsmore, B., and G. R. Whitfield, Lunar occultation of a radio star and the derivation of an upper limit for the density of the lunar atmosphere, *Nature*, *176*, 457–458, 1955.

England, S. L., T. J. Immel, E. Sagawa, S. B. Henderson, M. E. Hagan, S. B. Mende, H. U. Frey, C. M. Swenson, and L. J. Paxton, Effect of atmospheric tides on the morphology of the quiet time, postsunset equatorial ionospheric anomaly, *J. Geophys. Res.*, *111*, A10S19, doi: 10.1029/2006JA011795, 2006.

Farley, D. T., A theory of electrostatic fields in a horizontally stratified ionosphere subject to a vertical magnetic field, *J. Geophys. Res.*, *64*(9), 1225–1233, 1959.

Farley, D. T., A theory of electrostatic fields in the ionosphere at non-polar geomagnetic latitudes, *J. Geophys. Res.*, *65*(3), 869–877, 1960.

Farley, D. T., B. B. Balsley, R. F. Woodman, and J. P. McClure, Equatorial spread F: Implications of VHF radar observations, *J. Geophys. Res.*, *75*(34), 7199–7216, 1970.

Farley, D. T., E. Bonelli, B. G. Fejer, and M. F. Larsen, The prereversal enhancement of the zonal electric field in the equatorial zone, *J. Geophys. Res.*, *91*(A12), 13,723–13,728, 1986.

Fejer, B. G., D. T. Farley, R. F. Woodman, and C. Calderón, Dependence of equatorial F-region vertical drifts on season and solar cycle, *J. Geophys. Res.*, *84*(A10), 5792–5796, 1979.

Fjeldbo, G., A. J. Kliore, and V. R. Eshleman, The neutral atmosphere of Venus as studied with the Mariner V radio occultation experiments, *Astron. J.*, *76*(2), 123–140, 1971.

García, F. J., Atmospheric studies using all-sky imaging of airglow layers, Ph.D. dissertation, Cornell University, 1999.

Gentile, L. C., W. J. Burke, and F. J. Rich, A climatology of equatorial plasma bubbles from DMSP 1989–2004, *Radio Sci.*, *41*, RS5S21, doi:10.1029/2005RS003340, 2006.

Gorbunov, M. E., and A. S. Gurvich, Algorithms of inversion of Microlab-1 satellite data including effects of multipath propagation, *Int. J. Remote Sensing*, *19*(12), 2283–2300, 1998.

Gorbunov, M. E., A. S. Gurvich, and A. V. Shmakov, Back-propagation and radio-holographic methods for investigation of sporadic ionospheric E-layers from Microlab-1 data, *Int. J. Remote Sensing*, *23*(4), 675–685, 2002.

Gordon, W. E., Incoherent scattering of radio waves by free electrons with applications to space exploration by radar, *Proc. IRE*, *46*(11), 1824–1858, 1958.

Groves, K. M., et al., Equatorial scintillation and systems support, *Radio Sci.*, *32*(5), 2047–2064, 1997.

Haerendel, G., and J. V. Eccles, The role of the equatorial electrojet in the evening ionosphere, *J. Geophys. Res.*, *97*(A2), 1181–1192, 1992.

Harrington, J. V., R. W. Goff, M. D. Grossi, and B. M. Langworthy, Orbiter-to-orbiter radio occultation measurement of planetary atmospheres and ionospheres, *AIAA Journal*, *8*(7), 1335–1341, 1970.

Heelis, R. A., Electrodynamics in the low and middle latitude ionosphere: A tutorial, *J. Atmos. Solar-Terr. Phys.*, *66*, 825–838, 2004.

Hernández-Pajares, M., J. M. Juan, and J. Sanz, Improving the Abel inversion by adding ground GPS data to LEO radio occultations in ionospheric sounding, *Geophys. Res. Lett.*, *27*(16), 2473–2476, 2000.

Hoffleit, E. D., and C. Jaschek, *The Bright Star Catalogue*, 5th ed. pp., Yale University Observatory, New Haven, CT, 1991.

Huang, C. Y., W. J. Burke, J. S. Machuzak, L. C. Gentile, and P. J. Sultan, Equatorial plasma bubbles observed by DMSP satellites during a full solar cycle: Toward a global climatology, *J. Geophys. Res.*, *107*(A12), 1434, doi:10.1029/2002JA009452, 2002.

Huba, J. D., G. Joyce, S. Sazykin, R. Wolf, and R. Spiro, Simulation study of penetration electric field effects on the low- to mid-latitude ionosphere, *Geophys. Res. Lett.*, *32*, L23101, doi: 10.1029/2005GL024162, 2005.

Hysell, D. L., Radar imaging of equatorial F region irregularities with maximum entropy interferometry, *Radio Sci.*, *31*(6), 1567–1578, 1996.

Hysell, D. L., An overview and synthesis of plasma irregularities in equatorial spread F, *J. Atmos. Solar-Terr. Phys.*, *62*, 1037–1056, 2000.

Hysell, D. L., Inverting ionospheric radio occultation measurements using maximum entropy, *Radio Sci.*, *42*, RS4022, doi:10.1029/2007RS003635, 2007.

Hysell, D. L., and J. D. Burcham, JULIA radar studies of equatorial spread F, *J. Geophys. Res.*, *103*, 29,155–29,167, 1998.

Hysell, D. L., and D. T. Farley, Implications of the small aspect angles of equatorial spread F, *J. Geophys. Res.*, *101*(A3), 5165–5176, 1996.

Hysell, D. L., and E. Kudeki, Collisional shear instability in the equatorial F region ionosphere, *J. Geophys. Res.*, *109*, A11301, doi:10.1029/2004JA010636, 2004.

Hysell, D. L., J. Chun, and J. L. Chau, Bottom-type scattering layers and equatorial spread F, *Ann. Geophys.*, *22*, 4061–4069, 2004.

Hysell, D. L., J. L. Chau, and S. Lakshmanan, Improved spectral estimation of equatorial spread F through aperiodic pulsing and Bayesian inversion, *Radio Sci.*, *43*, RS2010, doi: 10.1029/2007RS003790, 2008a.

Hysell, D. L., F. S. Rodrigues, J. L. Chau, and J. D. Huba, Full profile incoherent scatter analysis at Jicamarca, *Ann. Geophys.*, *26*, 59–75, 2008b.

Immel, T. J., E. Sagawa, S. L. England, S. B. Henderson, M. E. Hagan, S. B. Mende, H. U. Frey, C. M. Swenson, and L. J. Paxton, The control of equatorial ionospheric morphology by atmospheric tides, *Geophys. Res. Lett.*, *33*, L15108, doi:10.1029/2006GL026161, 2006.

Jahn, J.-M., and J. LaBelle, Rocket measurements of high-altitude spread F irregularities at the magnetic dip equator, *J. Geophys. Res.*, *103*(A10), 23,427–23,441, 1998.

Kelley, M. C., *The Earth's Ionosphere* pp., Academic Press, San Diego, CA, 1989.

Kelley, M. C., M. F. Larsen, and C. L. Hoz, Gravity wave initiation of equatorial spread F: A case study, *J. Geophys. Res.*, *86*, 9087–9100, 1981.

Kelley, M. C., R. C. Livingston, C. L. Rino, and R. T. Tsunoda, The vertical wave number spectrum of topside equatorial spread F: Estimates of backscatter levels and implications for a unified theory, *J. Geophys. Res.*, *87*(A7), 5217–5221, 1982.

Kelley, M. C., J. J. Makela, B. M. Ledvina, and P. M. Kintner, Observations of equatorial spread-F from Haleakala, Hawaii, *Geophys. Res. Lett.*, *29*(20), 2003, doi:10.1029/2002GL015509, 2002.

Kintner, P., B. Ledvina, E. de Paula, and I. Kantor, Size, shape, orientation, speed, and duration of GPS equatorial anomaly scintillations, *Radio Sci.*, *39*(2), RS2012, doi:10.1029/2003RS002878, 2004.

Kliore, A., D. L. Cain, G. S. Levy, V. R. Eshleman, G. Fjeldbo, and F. D. Drake, Occultation experiment: Results of the first direct measurement of Mars's atmosphere and ionosphere, *Science*, *149*, 1243–1248, 1965.

Kudeki, E., and S. Bhattacharyya, Postsunset vortex in equatorial F-region plasma drifts and implications for bottomside spread-F, *J. Geophys. Res.*, *104*(A12), 28,163–28,170, 1999.

Kudeki, E., and F. Sürücü, Radar interfrometric imaging of field-aligned plasma irregularities in the equatorial electrojet, *Geophys. Res. Lett.*, *18*(1), 41–44, 1991.

Kudeki, E., A. Akgiray, M. Milla, J. L. Chau, and D. L. Hysell, Equatorial spread-F initiation: Post-sunset vortex, thermospheric winds, gravity waves, *J. Atmos. Solar-Terr. Phys.*, *69*(17–18), 2416–2427, doi:10.1016/j.jastp.2007.04.012, 2007.

Kunitsyn, V. E., and E. D. Tereshchenko, *Ionospheric Tomography*, Physics of Earth and Space Environments Series pp., Springer-Verlag, Berlin, 2003.

Ledvina, B., P. Kintner, and E. de Paula, Understanding spaced-receiver zonal velocity estimation, *J. Geophys. Res.*, *109*(A10), A10306, doi:10.1029/2004JA010489, 2004.

Ledvina, B. M., A scintillation-based spaced-receiver analysis of scattering medium dynamics in the equatorial ionosphere, Ph.D. dissertation, Cornell University, 2004.

Ledvina, B. M., and J. J. Makela, First observations of SBAS/WAAS scintillations: Using colocated scintillation measurements and all-sky images to study equatorial plasma bubbles, *Geophys. Res. Lett.*, *32*(14), L14101, doi:10.1029/2004GL021954, 2005.

Lee, J. K., F. Kamalabadi, and J. J. Makela, Three-dimensional tomography of ionospheric variability using a dense GPS receiver array, *Radio Sci.*, *43*, RS3001, doi:10.1029/2007RS003716, 2008.

Lei, J., et al., Comparison of COSMIC ionospheric measurements with ground- based observations and model predictions: Preliminary results, *J. Geophys. Res.*, *112*, A07308, doi: 10.1029/2006JA012240, 2007.

Lim, J. S., *Two-Dimensional Signal and Image Processing*, pp. 469–476, Prentice Hall, Englewood Cliffs, NJ, 1990.

Link, R., and L. L. Cogger, A reexamination of the O I 6300 Å nightglow, *J. Geophys. Res.*, *93*(A9), 9883–9892, 1988.

MacDougall, J. W., Distributions of the irregularities which produce ionospheric scintillations, *J. Atmos. Terr. Phys.*, *43*(4), 317–325, 1981.

Makela, J. J., A review of imaging low-latitude ionospheric irregularity processes, *J. Atmos. Solar-Terr. Phys.*, *68*(13), 1441–1458, doi:10.1016/j.jastp.2005.04.014, 2006.

Makela, J. J., and M. C. Kelley, Field-aligned 777.4-nm composite airglow images of equatorial plasma depletions, *Geophys. Res. Lett.*, *30*(8), 1442, doi:10.1029/2003GL017106, 2003a.

Makela, J. J., and M. C. Kelley, Using the 630.0-nm nightglow emission as a surrogate for the ionospheric Pedersen conductivity, *J. Geophys. Res.*, *108*(A6), 1253, doi:10.1029/2003JA009894, 2003b.

Makela, J. J., and E. S. Miller, Optical observations of the growth and day-to-day variability of equatorial plasma bubbles, *J. Geophys. Res.*, *113*, A03307, doi:10.1029/2007JA012661, 2008.

Makela, J. J., B. M. Ledvina, M. C. Kelley, and P. M. Kintner, Analysis of the seasonal variations of equatorial plasma bubble occurrence observed from Haleakala, Hawaii, *Ann. Geophys.*, *22*, 3109–3121, 2004.

Makela, J. J., M. C. Kelley, and M. J. Nicolls, Optical observations of the development of secondary instabilities on the eastern wall of an equatorial plasma bubble, *J. Geophys. Res.*, *111*, A09311, doi:10.1029/2006JA011646, 2006.

Makela, J. J., M. C. Kelley, and R. T. Tsunoda, Observations of midlatitude ionospheric instabilities generating meter-scale waves at the magnetic equator, *J. Geophys. Res.*, *114*, A01,307, doi:10.1029/2007JA012946, 2009.

Marouf, E. A., G. L. Tyler, and P. A. Rosen, Profiling Saturn's rings by radio occultation, *Icarus*, *68*, 120–166, 1986.

Martinis, C. R., M. J. Mendillo, and J. Aarons, Toward a synthesis of equatorial spread F onset and suppression during geomagnetic storms, *J. Geophys. Res.*, *110*, A07306, doi:10.1029/2003JA010362, 2005.

Maruyama, T., and N. Matuura, Longitudinal variability of annual changes in activity of equatorial spread F and plasma bubbles, *J. Geophys. Res.*, *89*(A12), 10,903–10,912, 1984.

Maus, S., et al., The 10th generation international geomagnetic reference field, *Phys. Earth Planet. Int.*, *151*, 320–322, doi:10.1016/j.pepi.2005.03.006, 2005.

McClure, J. P., S. Singh, D. K. Bambgboye, F. S. Johnson, and H. Kil, Occurrence of equatorial F region irregularities: Evidence for tropospheric seeding, *J. Geophys. Res.*, *103*(A12), 29,119–29,135, 1998.

Mendillo, M., and J. Baumgardner, Airglow characteristics of equatorial plasma depletions, *J. Geophys. Res.*, *87*(A9), 7641–7652, 1982.

Mendillo, M., and A. Tyler, Geometry of depleted plasma regions in the equatorial ionosphere, *J. Geophys. Res.*, *88*(A7), 5778–5782, 1983.

Mendillo, M., J. Baumgardner, X. Pi, P. J. Sultan, and R. T. Tsunoda, Onset conditions for equatorial spread F, *J. Geophys. Res.*, *97*(A9), 13,865–13,876, 1992.

Mendillo, M., J. W. Meriwether, and M. A. Biondi, Testing the thermospheric neutral wind suppression mechanism for day-to-day variability of equatorial spread F, *J. Geophys. Res.*, *106*(A3), 3655–3663, 2001.

Miller, E. S., and J. J. Makela, A multi-instrument technique for localization of scintillation-causing regions in the equatorial ionosphere, *J. Geophys. Res.*, *113*, A12303, doi:10.1029/2008JA013144, 2008.

Ossakow, S. L., Spread-F theories—a review, *J. Atmos. Terr. Phys.*, *43*, 437–452, 1981.

Otsuka, Y., K. Shiokawa, T. Ogawa, and P. Wilkinson, Geomagnetic conjugate observations of equatorial airglow depletions, *Geophys. Res. Lett.*, *29*(15), 1753, doi:10.1029/2002GL015347, 2002.

Otsuka, Y., K. Shiokawa, T. Ogawa, and P. Wilkinson, Geomagnetic conjugate observations of medium-scale traveling ionospheric disturbances at midlatitude using all-sky airglow imagers, *Geophys. Res. Lett.*, *31*, L15803, doi:10.1029/2004GL020262, 2004a.

Otsuka, Y., K. Shiokawa, T. Ogawa, T. Yokoyama, M. Yamamoto, and S. Fukao, Spatial relationship of equatorial plasma bubbles and field-aligned irregularities observed with an all-sky airglow imager and the Equatorial Atmosphere Radar, *Geophys. Res. Lett.*, *31*, L20802, doi:10.1029/2004GL020869, 2004b.

Otsuka, Y., K. Shiokawa, T. Ogawa, T. Yokoyama, and M. Yamamoto, Spatial relationship of nighttime medium-scale traveling ionospheric disturbances and F region field-aligned irregularities observed with two spaced all-sky airglow imagers and the middle and upper atmosphere radar, *J. Geophys. Res.*, *114*(A05302), doi:10.1029/2008JA013902, 2009.

Pannekoek, A., Über die Erscheinungen, welche bei einer Sternbedeckung durch einen Planeten auftreten, *Astron. Nachr.*, *164*, 5–10, 1903.

Perkins, F., Spread F and ionospheric currents, *J. Geophys. Res.*, *78*(1), 218–226, 1973.

Picone, J. M., A. E. Hedin, D. P. Drob, and A. C. Aikin, NRLMSISE-00 empirical model of the atmosphere: Statistical comparisons and scientific issues, *J. Geophys. Res.*, *107*(A12), 1468, doi: 10.1029/2002JA009430, 2002.

Ratcliffe, J. A., Some aspects of diffraction theory and their application to the ionosphere, *Rep. Progr. Phys.*, *19*, 188–267, 1956.

Reber, G., Spread F over Hawaii, *J. Geophys. Res.*, *59*(2), 257–265, 1954.

Rishbeth, H., Polarization fields produced by winds in the equatorial F-region, *Planet. Space Sci.*, *19*(3), 357–369, 1971.

Rishbeth, H., The ionospheric E-layer and F-layer dynamos — a tutorial review, *J. Atmos. Solar-Terr. Phys.*, *59*(15), 1873–1880, 1997.

Rohrbaugh, R. P., W. B. Hanson, B. A. Tinsley, B. L. Cragin, J. P. McClure, and A. L. Broadfoot, Images of transequatorial bubbles based on field-aligned airglow observations from Haleakala in 1984–1986, *J. Geophys. Res.*, *94*(A6), 6763–6770, 1989.

Sahai, Y., P. R. Fagundes, and J. A. Bittencourt, Transequatorial F-region ionospheric plasma bubbles: solar cycle effects, *J. Atmos. Solar-Terr. Phys.*, *62*, 1377–1383, 2000.

Saito, A., T. Iyemori, M. Sugiura, N. C. Maynard, T. L. Aggson, L. H. Brace, M. Takeda, and M. Yamamoto, Conjugate occurrence of the electric field fluctuations in the nighttime midlatitude ionosphere, *J. Geophys. Res.*, *100*(A11), 21,439–21,451, 1995.

Saito, S., S. Fukao, M. Yamamoto, Y. Otsuka, and T. Maruyama, Decay of 3-m-scale ionospheric irregularities associated with a plasma bubble observed with the Equatorial Atmosphere Radar, *J. Geophys. Res.*, *113*, A11318, doi:10.1029/2008JA013118, 2008.

Sekar, R., D. Chakrabarty, S. Sarkhel, A. K. Patra, C. V. Devasia, and M. C. Kelley, Identification of active fossil bubbles based on coordinated VHF radar and airglow measurements, *Ann. Geophys.*, *25*, 2099–2102, 2007.

Sheehan, R. E., and C. E. Valladares, Equatorial ionospheric zonal drift model and vertical drift statistics from UHF scintillation measurements in South America, *Ann. Geophys.*, *22*, 3177–3193, 2004.

Sokolovskiy, S., W. Schreiner, C. Rocken, and D. Hunt, Detection of high-altitude ionospheric irregularities with GPS/MET, *Geophys. Res. Lett.*, *29*(3), 1033, doi:10.1029/2001GL013398, 2002.

Straus, P. R., P. C. Anderson, and J. E. Danaher, GPS occultation sensor observations of ionospheric scintillation, *Geophys. Res. Lett.*, *30*(8), 1436, doi:10.1029/2002GL016503, 2003.

Su, S.-Y., C. K. Chao, and C. H. Liu, Cause of different local time distribution in the postsunset equatorial ionospheric irregularity occurrences between June and December solstices, *J. Geophys. Res.*, *114*, A04321, doi:10.1029/2008JA013858, 2009.

Sultan, P. J., Linear theory and modeling of the Rayleigh-Taylor instability leading to the occurrence of equatorial spread F, *J. Geophys. Res.*, *101*(A12), 26,875–26,891, 1996.

Tinsley, B. A., Field aligned airglow observations of transequatorial bubbles in the tropical F-region, *J. Atmos. Terr. Phys.*, *44*(6), 547–557, 1982.

Tinsley, B. A., A. B. Christensen, J. Bittencourt, H. Gouveia, P. D. Angreji, and H. Takahashi, Excitation of oxygen permitted line emissions in the tropical nightglow, *J. Geophys. Res.*, *78*(7), 1174–1186, 1973.

Tsunoda, R. T., On the spatial relationship of 1-m equatorial spread-F irregularities and plasma bubbles, *J. Geophys. Res.*, *85*, 185–190, 1980.

Tsunoda, R. T., On the generation and growth of equatorial backscatter plumes: Structuring of the west walls of upwellings, *J. Geophys. Res.*, *88*(A6), 4869–4874, 1983.

Tsunoda, R. T., Control of the seasonal and longitudinal occurrence of equatorial scintillations by the longitudinal gradient in integrated E region Pedersen conductivity, *J. Geophys. Res.*, *90*(A1), 447–456, 1985.

Tsunoda, R. T., Day-to-day variability in equatorial spread F: Is there some physics missing? *Geophys. Res. Lett.*, *33*, L16,106, doi:10.1029/2006GL025956, 2006.

Tsunoda, R. T., Seeding of equatorial plasma bubbles with electric fields from an E_s-layer instability, *J. Geophys. Res.*, *112*, A06304, doi:10.1029/2006JA012103, 2007.

Tsunoda, R. T., R. C. Livingston, J. P. McClure, and W. B. Hanson, Equatorial plasma bubbles: Vertically elongated wedges from the bottomside F layer, *J. Geophys. Res.*, *87*, 9171–9180, 1982.

Valladares, C. E., R. E. Sheehan, S. Basu, H. Kuenzler, and J. Espinoza, The multi-instrumented studies of equatorial thermosphere aeronomy scintillation system: Climatology of zonal drifts, *J. Geophys. Res.*, *101*(A12), 26,839–26,850, 1996.

Woodman, R. F., Vertical drift velocities and east-west electric fields at the magnetic equator, *J. Geophys. Res.*, *75*(31), 6249–6259, 1970.

Woodman, R. F., Coherent radar imaging: Signal processing and statistical properties, *Radio Sci.*, *32*(6), 2373–2391, 1997.

Woodman, R. F., and S. Basu, Comparison between in-situ spectral measurements of F-region irregularities and backscatter observations at 3-m wavelength, *Geophys. Res. Lett.*, *5*(10), 869–872, 1978.

Woodman, R. F., and C. L. Hoz, Radar observations of F region equatorial irregularities, *J. Geophys. Res.*, *81*(31), 5447–5466, 1976.

Yao, D., and J. J. Makela, Analysis of equatorial plasma bubble zonal drift velocities in the Pacific sector by imaging techniques, *Ann. Geophys.*, *25*, 701–709, 2007.

Yeh, K. C., and C. H. Liu, Radio wave scintillations in the ionosphere, *Proc. IEEE*, *70*(4), 324–360, 1982.

AUTHOR'S BIOGRAPHY

Ethan Schofield Miller was born and raised in Millersburg, Ohio. He was first exposed to electrical engineering while sitting on his father's lap as he wrote BASIC code on a HeathKit H-8 microcomputer. Although he was later fascinated by construction work, automobiles, and airplanes, he eventually came back to electronics. His work has varied from building mobile robot cleaning devices to fabricating and evaluating 110-GHz interconnects to tracking insect pests with harmonic radar. Ethan married Sarah in 2005, and they both began pursuing graduate degrees at the University of Illinois. His most recent work on remote sensing of the ionosphere has been motivated by a long-standing interest in amateur radio, as well as a keen interest in configuring instrumentation and making sense of data. After graduation, he will be employed by the Johns Hopkins University Applied Physics Laboratory in the Atmospheric and Ionospheric Remote Sensing group.